The University Of Sheffield.

Modelling, Simulation and Performance Evaluation of Post-Combustion Carbon Capture based on Chemical Absorption

Olajide Stephen Otitoju

Supervisor: Prof Meihong Wang

A thesis submitted in partial fulfilment of the requirement for the degree of Doctor of Philosophy

Department of Chemical and Biological Engineering

Faculty of Engineering

The University of Sheffield

January 2022

Acknowledgement

I am most grateful to God almighty the giver of life for the grace bestowed upon me to embark on this PhD journey. May his name alone be praised. My most profound and heartfelt gratitude goes to Professor Meihong Wang for his motivations, patience, invaluable advice on how to improve the quality of my research and consistent push for me to be better. Your efforts toward the successful completion of this PhD programme are deeply appreciated, Sir. I would also like to appreciate the efforts of Dr Eni Oko for his help and most importantly his valuable and insightful comments throughout this PhD programme. Eni picks the phone at the first ring and is ever willing to answer my questions. To every member of the Process and Energy Systems Engineering research group, I am thankful for the friendship we have shared over this PhD period. Every moment of this PhD journey with you guys has been a very pleasurable one.

This PhD programme would not have been possible without the financial support from the Petroleum Technology Development Fund (PTDF), who provided full scholarship for me throughout the PhD programme. I am very grateful for the privilege. To the members of the Redeemed Christian Church of God (RCCG) Joy Assembly, Sheffield. I am grateful for the love and brotherhood that we share.

To my lovely, beautiful wife Mrs Titilayo Otitoju, I am most grateful for the gift of your love and companionship. Thank you very much for taking good care of our home and kids during those endless times I was away from home. Your selfless sacrifices are deeply appreciated. I love you. To my lovely daughter Bowofola Otitoju you have been a source of blessings to me since you came into our life. I am very proud of the intelligent young woman you are becoming. To my darling son Diekolola Otitoju you are the precious gift that God blessed us with on this PhD journey. Every time you whisper “I love you dad” in your little tiny voice my joy knows no bound. To my sisters, friends and in-laws, I am grateful for your continued support.

Abstract

Carbon dioxide is a greenhouse gas and its emissions contribute to climate change. Fossil-fuel-fired power plants are the largest emitter of CO_2. The solvent-based post-combustion carbon capture (PCC) is the most developed technology to cut down CO_2 emissions from power plants. The downsides of the PCC process is the high costs (capital and operating costs) and the high energy needed for solvent regeneration. These have prevented the large-scale deployments of the PCC process. Through accurate scale-up, modified process configurations, use of solvent such as piperazine (PZ) in place of monoethanolamine (MEA) and the use of rotating packed bed (RPB) in place of packed (PB), the energy consumption and the cost of the solvent-based PCC process can be reduced significantly.

A steady-state rate-based model of the PCC process in PB using MEA solvent was developed and validated with pilot-scale experimental data in Aspen Plus®. The model predictions agreed with experimental data. A new scale-up method based on the flooding gas velocity was proposed and validated by using it to scale up between two existing pilot plants of different sizes. The scale-up method accurately predicted the diameter of the absorber and stripper with a deviation of 2.6% and 1.54% respectively. This method was also used to develop a PCC plant for a 250 MW_e CCGT power plant. It was found that the proposed scale-up method gives a lower column size compared to the generalized pressure drop correlation (GPDC) method.

The use of new solvents and modified process configurations are some of the options being pursued to reduce the cost and energy consumption of the solvent-based PCC process. A steady-state rate-based model of the PCC process in PB using PZ as a solvent was developed in Aspen Plus®. The accuracy of the model was verified by validating with pilot-scale experimental data. The model predictions were within ±10% of experimental data. The model was used to assess the technical and economic performances of a large-scale PCC process using PZ solvent for a 250 MW_e CCGT power plant. The technical and economic assessments were performed in Aspen Plus® and Aspen Process Economic Analyzer® (APEA) respectively. Three configurations of the process including the standard, absorber intercooling (IC) and absorber intercooling with advanced flash stripper (AIAFS) were evaluated. Results obtained from the process evaluations of the three configurations of the PCC process using PZ were compared to those of the benchmark process using 30

wt% MEA solvent. The technical assessment results revealed that the total energy needed to capture and compress a tonne of CO_2 by the PCC process was 3.56 GJ/t_{CO_2} with the standard process configuration using 30 wt% PZ as against 4.57 GJ/t_{CO_2} with the standard process configuration using 30 wt% MEA. The lowest total energy attained was 2.41 GJ/t_{CO_2} with the AIAFS process configurations using 40 wt% PZ. Economic assessments results indicated that the least total annual cost (TAC) and the least cost of CO2 capture were M$26.58/year and $34.65/$t_{CO_2}$ respectively. These were attained with the AIAFS process configuration using 40 wt% PZ solvent. Thus, the PCC process using 40 wt% PZ offers both technical and economic benefits over the current 30 wt% MEA PCC process.

RPB has the potential to significantly reduce the size of the absorber and stripper when used in place of PB for CO2 capture. A steady-state rate-based model of the RPB absorber was developed and validated at a pilot scale using Aspen Custom Modeller® (ACM). A new methodology for RPB scale-up was proposed. The RPB model was scaled up using an iterative procedure for a 250 MW_e CCGT power plant. Technical and economic assessment of the large-scale PCC process using RPB shows that a 5-13 times volume reduction factor was achieved with the RPB absorber (using 75 wt% MEA) compared to the PB absorbers (using 30 wt% MEA and 40 wt% PZ). The CAPEX also reduced by 39-69% with RPB absorbers compared to PB absorbers. This shows that the size, cost and footprint of the entire PCC process can be reduced with RPB as an absorber.

Keywords: Post-combustion carbon capture; Chemical absorption; Packed Bed; Rotating packed Bed; Process modelling and simulation; Scale-up; Technical and economic assessment; Combined cycle gas turbine power plant

List of peer-reviewed Publications and Presentations

Peer-reviewed journal

Parts of the work presented in Chapter 3 of this PhD thesis has been published in a peer-reviewed journal as follows:

- **Otitoju, O.,** Oko, E., Wang, M., (2020). A new method for scale-up of solvent-based post-combustion carbon capture process with packed column. *International Greenhouse Gas Control,* 93, 102900.

Parts of the work presented in Chapter 4 of this PhD thesis has been published in a peer-reviewed journal as follows:

- **Otitoju, O.,** Oko, E., Wang, M., (2021). Technical and economic performance assessment of post-combustion carbon capture using piperazine for large-scale natural gas combined cycle power plants through process simulation. *Applied Energy,* 292, 116893.

Parts of the work presented in Chapters 5 and 6 of this PhD thesis appears in a peer-reviewed journal as follows:

- **Otitoju, O.,** Wang, M., (2022). Modelling, Scale-up and techno-economic performance analysis of RPB absorber for 250 MW_e CCGT power plant. *Applied Energy* (under review).

The author contributed to the following journal paper:

- Hua, G., Lia, X., Liua, X., Hub, J., **Otitoju, O.,** Wang, M,. Du, W, Ye, Z., Long, Z., Qian, F., (2022) Techno-economic evaluation of post-combustion carbon capture based on chemical absorption for the thermal cracking furnace in ethylene manufacturing. *Applied Energy* (under review).

Conference presentations and proceedings:

(a) Conference proceedings: Parts of the work presented in Chapter 4 of this thesis has been published in conference proceedings as follows:

- **Otitoju, O.,** Oko, E., Wang, M, (2021). Energy Performance Analysis of Post-combustion Carbon Capture using Piperazine for Large-scale Natural Gas Combined

Cycle Power Plants. *Proceedings of the 15th Greenhouse Gas Control Technologies Conference 15-18 March 2021,* Available at SSRN: https://ssrn.com/abstract=3814904

(b) Oral Presentations

- **Otitoju, O.,** Oko, E., Wang, M. (2018). Solvent-based post-combustion capture: Process simulation, validation and scale-up. *12th European Conference on Coal Research and its Applications, Cardiff UK. 5th -7th September 2018*.
- **Otitoju, O**., Oko, E., Wang, M. (2021). Energy Performance Analysis of Post-combustion Carbon Capture using Piperazine for Large-scale Natural Gas Combined Cycle Power Plants. *15th International virtual conference on Greenhouse Gas Control Technologies (GHGT-15), Abu Dhabi, 15-18 March 2021.*

Table of contents

List of Figures

List of Tables

Nomenclatures

A Area (m^2)

a_{gl} Gas-liquid interfacial area (m^2/m^3)

a_t Specific surface area of packing (m^2/m^3)

ATU Area of transfer units (m^2)

a'_p Surface area of the 2 mm diameter bead per unit volume of the bead (1/m)

$C_{l,i}$ Concentration of component *i*. ($kmol/m^3$)

CP Capacity parameter

$C_{p,g}$ Gas specific heat capacity (kJ/kg K)

$C_{p,l}$ Liquid specific heat capacity (kJ/kg K)

D Diameter (m)

$D_{g,i}$ Gas diffusivity of component *i* (m^2/s)

d_h Hydraulic diamter (m)

$D_{l,i}$ Liquid diffusivity of component *i* (m^2/s)

d_p Effective diameter of packing (m)

E_i Enhancement factor of component i

E_a Activation energy (kJ/kmol)

f_d Fraction of the packing in the inner radius occupied by the liquid distributor

F_g Gas molar flow rate (kmol/s)

F_{g_a} Gas molar flow rate per cross-sectional area ($kmol/m^2$ s)

F_l Liquid molar flow rate (kmol/s)

F_{LV} Flow parameter

F_p Packing factor (m^{-1})

G Gas mass flow rate (kg/s)

g Acceleration due to gravity (m/s)

g_0 Characteristic acceleration with a value of 100 m/s^2

He_{excess} Excess Henry's coefficient for the MEA+H_2O binary system

$H_{el,i}$ Henry constant of component i in the liquid ($bar.m^3/kmol$)

h_{gl} Interfacial heat transfer coefficient (kW/m² K)

H_{OG} Height of the transfer unit (m)

ΔH_{rxn} Heat of absorption of CO2 (kJ/kmol)

$\Delta H_{vap,H2O}$ Heat of vaporization of water (kJ/kmol)

$\Delta H_{vap,H2O,bp}$ Heat of vaporization at boiling point (kJ/kmol)

k_{app} The apparent reaction rate constant (1/s)

K_{eq} Equilibrium constant

$K_{eq,CO2}$ Combined Henry's law and chemical equilibrium constants

$k_{g,i}$ Mass transfer coefficient of component i in the gas phase (m/s)

k_i Third order reaction rate constant for component i (MEA and H2O) (m6/(kmol2.s))

k_j^o Pre-exponential factor (m³/kmol.s)

$k_{l,ave}$ Average liquid film mass transfer coefficient (m/s)

$k_{l,i}$ Mass transfer coefficient of component i in the liquid phase (m/s)

$K_{tot,i}$ Overall gas-phase mass transfer coefficient (kmol/m³ s bar)

L Solvent mass flow rate (kg/s)

M_{MEA} Molar mass of MEA (kg/kmol)

N Temperature factor

N_i Molar fluxes of components (kmol/m²s)

NTU Number of transfer units

P Pressure (bar)

$P_{g,i}$ Partial pressure of component *i* in the gas phase (bar)

P_m Rotor power consumption (kW)

P_i^* Equilibrium partial pressure of component *i* (bar)

P_i^{vap} Vapour pressures of component *i* (bar)

$P^{l/g}$ Ratio of the kinetic energy of the liquid to the kinetic energy of the gas

ΔP_{fl} Flooding pressure drop (in.H_2O/ft)

ΔP_{RPB} Pressure drop across the RPB

Q_g Gas volumetric flow rate (m³/s)

Q_L Liquid volumetric flow rate (m^3/s)

R Universal gas constant (kJ/kmol.K)

r variable radius (m)

r_i Inner radius (m)

r_o outer radius (m)

r_s Radius of the stationary housing (m)

$R_{rxn,j}$ Reaction rate for reaction *j*, (m^3/kmol.s)

T Temperature (°C)

T_{bp} Temperature of water at boiling point (°C),

T_c Critical temperature (°C)

$u_{g,fl}$ Superficial flooding velocity (m/s)

u_g Superficial gas velocity (m/s)

u_{jet} Liquid jet velocity (m/s)

u_l Liquid superficial velocity (m/s)

U_0 Characteristics superficial liquid velocity with a value of 0.01 m/s,

V_o Volume between the outer radius of the bed and the stationary housing (m^3)

V_t Total volume of the RPB (m^3)

W_{comp} Compression work (GJ/t_{CO_2})

W_{eq} Total equivalent work (GJ/t_{CO_2})

W_{pump} Pump work (GJ/t_{CO_2})

W_{reg} Regeneration work (GJ/t_{CO_2})

x_i Liquid phase component molar fraction

y Mole fraction of CO_2 in the gas phase at any point in the column

y_1 Mole fraction of CO_2 in the inlet gas

y_2 Mole fraction of CO_2 in the outlet gas

y_e Gas-phase mole fraction of CO_2 in equilibrium with CO_2 concentration in the liquid

y_i Gas-phase component molar fraction

ž Number of equivalents/moles of amine (1 for MEA)

Z Packing height (m)

Greek letters

α_{Lean} Lean loading (mol_{CO_2}/mol_{MEA})

α_{Rich} Rich loading (mol_{CO_2}/mol_{MEA})

$\Delta\alpha$ Absorption capacity (mol_{CO_2}/mol_{MEA})

α_{ij} Specie *i* reaction order in reaction *j*

γ_i Activity coefficient of component *i*

ρ_G Gas density (kg/m^3)

ρ_l Liquid density (kg/m^3)

σc Critical surface tension (N/m)

σ Surface tension (N/m)

μ_g Gas viscosity (Ns/m^2)

μ_l Liquid viscosity (Ns/m^2)

ε Porosity

ε_g Gas holdup

ε_L liquid holdup

$\tau_{1,2}$ Parameter to describe the two-body interaction between MEA and H_2O

φ_{CO_2} percentage of CO_2 captured

ω Rotating speed (rad/s)

v Kinematic viscosity (m^2/s)

λ_l Liquid thermal conductivity (kW/mK)

Abbreviations

ACC Annual capital cost

ACM Aspen custom modeller

AI Absorber intercooling

AIAFS Absorber intercooling with advanced flash stripper

AMP 2-amino-2-methyl-1-propanol

APEA Aspen Process Economic Analyser®

ATU Area of transfer unit

BD Boundary Dam

BP British petroleum

CAPEX Capital expenditure

CCC Cost of CO_2 capture

CCGT Combined cycle gas turbine

CCUS CO_2 capture, utilization and storage (CCUS)

CRB Cold rich bypass

DAC Direct air capture

DCC Direct contact cooler

DEA Diethylamine

DETA Diethylenetriamine

FGD Flue Gas Desulphurization

FOMC Fixed operating and maintenance cost

GHG Greenhouse gas

HTU Height of the transfer unit

GPDC Generalized pressure drop correlation

MDEA Methyldiethanolamine

MEA Monoethanolamine

MOF Metal-organic framework

NTU Number of transfer units

OPEX Operating expenditure

PCC Post-combustion carbon capture

PN Petra Nova

PRE Percentage relative error

PZ Piperazine

TAC Total annual cost

TDC Total direct cost

TRL Technology readiness level

VLE Vapour liquid equilibrium

VOMC Variable operating and maintenance cost

WRB Warm rich bypass

Chapter 1: Introduction

This chapter sets the context of the thesis. Section 1.1 presents the background of the study. The motivation of the study is presented in Section 1.2 while the aim and objectives are presented in Section 1.3. Section 1.4 outlines the novel contributions of this PhD thesis. The scope of the study is detailed in Section 1.5. Research methodology is given in section 1.6. Tools utilized in the study are described in Section 1.7. In Section 1.8, the outline of the thesis is presented.

1.1 Background

1.1.1 Energy demand, CO_2 emissions and climate change

The global energy demand has continued to rise due to population increase and advancement in technology. The Global energy demand grew by 2.3% in 2018 and by 0.5% in 2019 (IEA, 2019). British Petroleum (BP) estimated a 30% increase in global energy demand from 2015 to 2035 (BP,2017). The global electricity production by source for 2019 is shown in Figure 1.1. In 2019, fossil fuels were responsible for 65.3% of global electricity production (IEA, 2021).

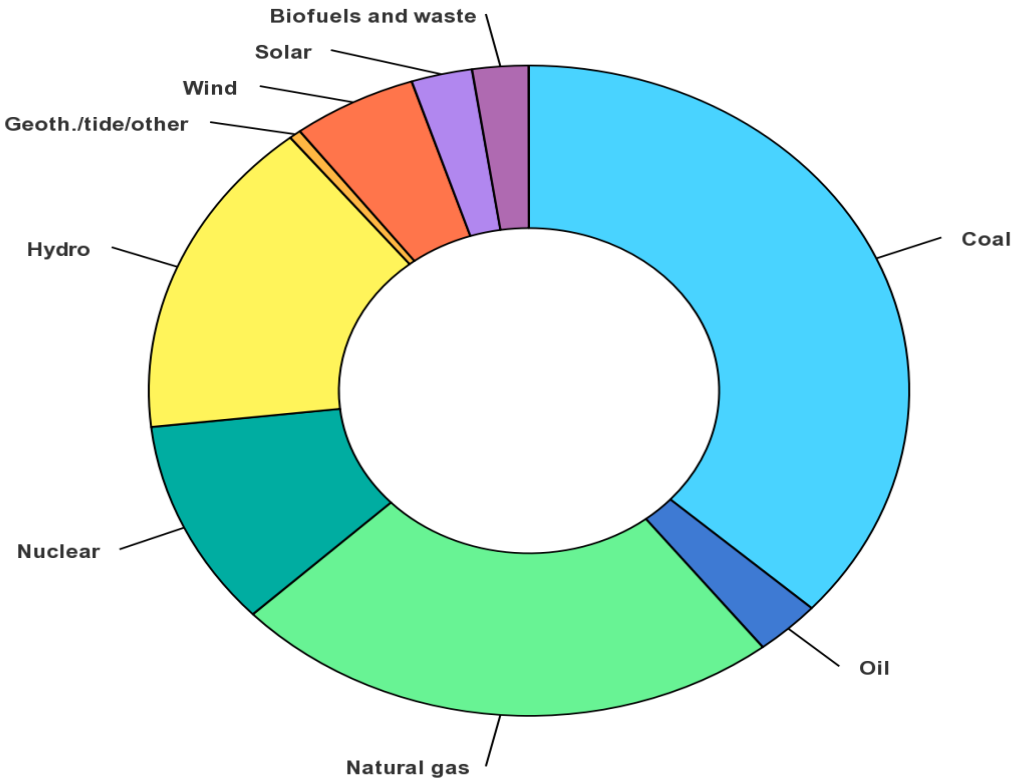

Figure 1.1 Global electricity production by fuel source 2019 (IEA, 2021)

The combustion of these fossil fuels in power plants and industries leads to CO_2 emissions. Power plants emit millions of tons of CO_2 per year (IPCC, 2005). The global CO_2 emissions from fossil fuel use were 36 gigatons (Gt) CO_2 in 2015 (CO2earth). This value is projected to reach 41.3Gt in 2040 if nothing is done (IEA, 2019). Fossil fuel-fired power plants are the largest source of CO_2 emissions (Wang et al., 2011). CO_2 is the main greenhouse gas (GHG) and its emissions have been directly linked to global climate change. The contribution of each GHG to the total global GHG emission is shown in Figure 1.2. CO_2 is responsible for 90% of the total GHG emissions.

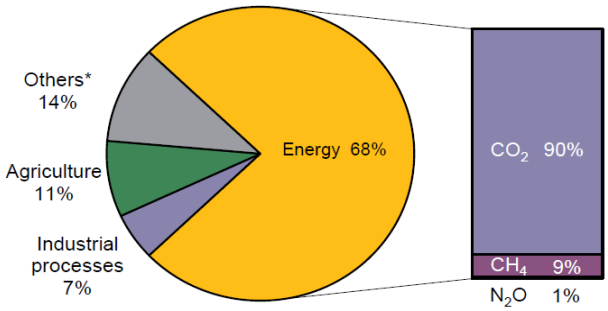

Figure 1.2 Global GHG emissions share by sector and gases

CO_2 emissions have led to an increase in the global atmospheric concentrations of CO_2 from 316 ppm in 1958 (IPCC, 2014) to 412 ppm in 2019 (CO2earth). At current fossil fuel consumption and CO_2 emissions rate, the global CO_2 concentration is projected to surpass 800 ppm by 2100 if no action is taken to address the situation. Under this scenario, the global surface temperature rise could reach 4.0 °C thereby exacerbating the climate change problem (CO_2earth). To combat this trend, effective CO_2 emissions mitigation technologies such as carbon capture, utilization and storage (CCUS) must be deployed in the decarbonization of high CO_2 emission sectors like power generation (power plants) and industries (iron and steel, cement production and petroleum refining). Among the various technology routes identified in Figure 1.3, CCUS is expected to be responsible for a 19 % reduction in the total global CO_2 emissions by 2050 (IEA, 2010).

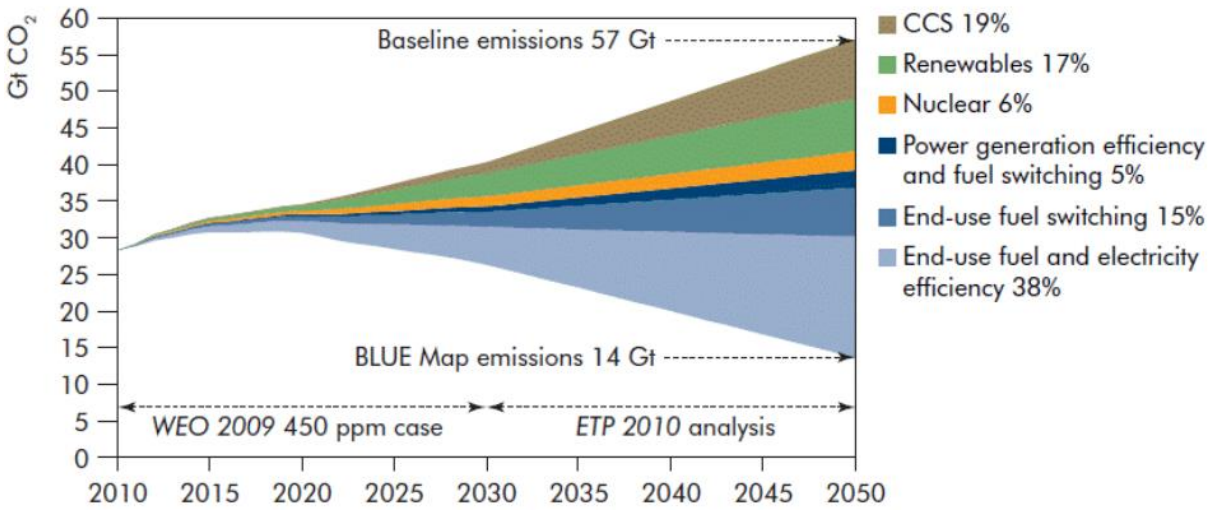

Figure 1.3 CO2 reduction projections for key technologies from 2010-2050 (IEA, 2010)

1.1.2 CO_2 capture, utilization and storage (CCUS)

CCUS refers to a process that captures CO_2 from industrial and energy-related sources, followed by transportation to a storage location where it is permanently sequestrated. The captured CO_2 can also be used as a valuable feedstock for the production of industrial chemicals and fuels. CCUS consists of three basic stages namely (a) CO_2 capture (b) CO_2 transportation (c) CO_2 storage/CO_2 utilization.

There are different technological routes for CO_2 capture. This includes post-combustion capture, pre-combustion capture, oxyfuel process and industrial processes (Kenarsari et al., 2013; Liang et al., 2015). These technological routes are illustrated in Figure 1.4.

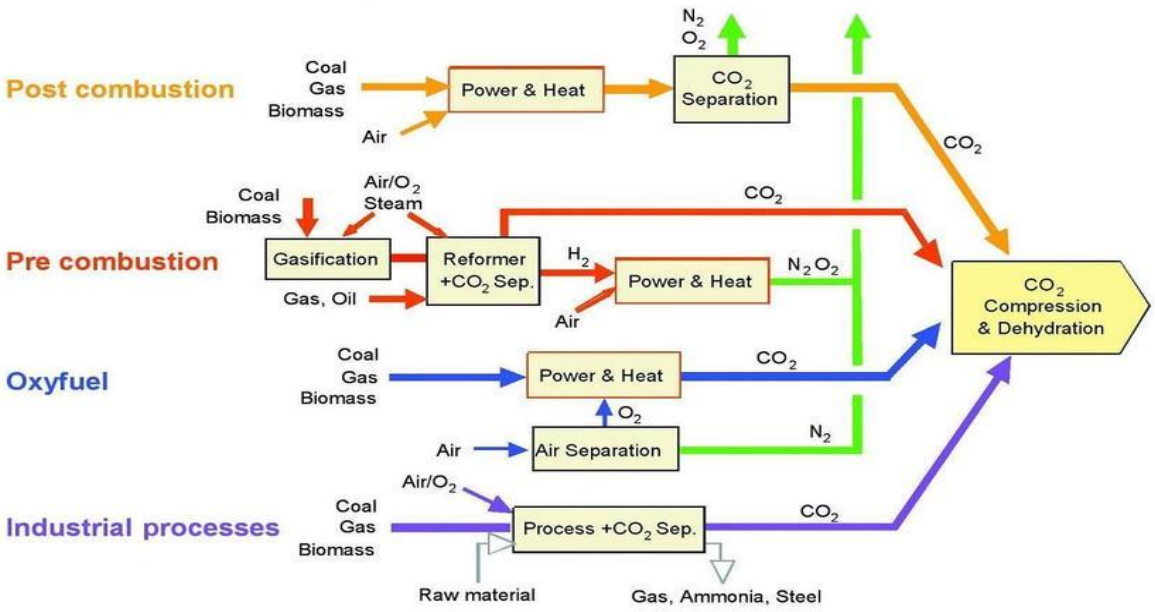

Figure 1. 4 Technological route for CO_2 capture approaches (IPCC, 2005)

Post-combustion capture (PCC) which involves the separation of CO_2 from the flue gases after combustion is considered the most viable option among these technologies. This is because it can be easily retrofitted to existing combustion technologies and can treat flue gases with low CO_2 partial pressure. However, when used as a retrofit option in existing power plants, it imposes a huge energy penalty on the power plant. Specifically, about 50% of the steam exiting the intermediate pressure steam turbine would be required for solvent regeneration. This corresponds to about 4 GJ/t of thermal energy consumption (Liguori and Wilcox, 2018).

1.1.3 Post-combustion capture (PCC)

The different technical options that could be used with post-combustion capture are illustrated in Figure 1.5. These include adsorption, membrane separation, cryogenics carbon capture, microbial/algal systems and absorption. Among these options, absorption, adsorption and membranes are the most studied. A brief discussion of these technical options is presented in the following sub-sections.

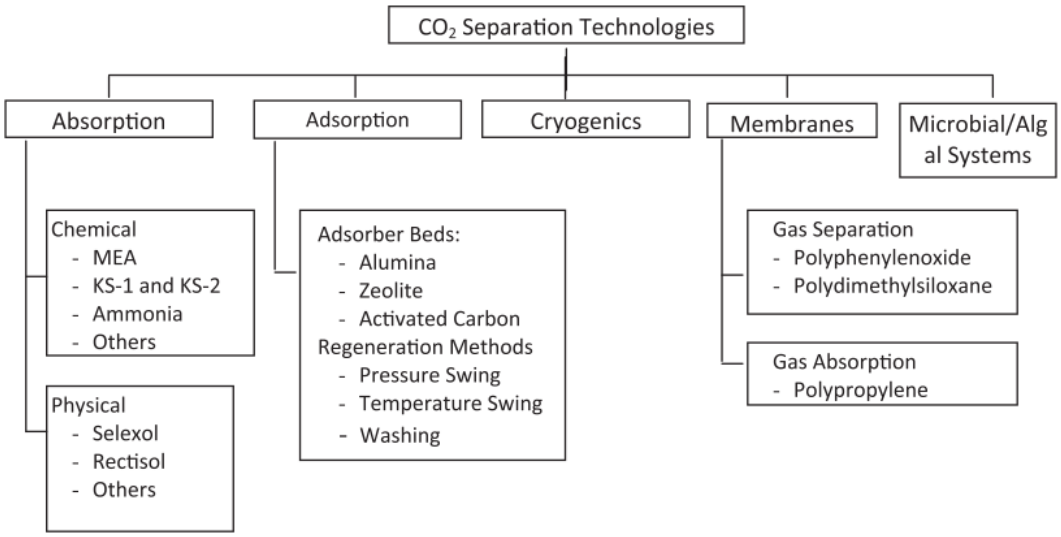

Figure 1.5 Various process technologies for post-combustion carbon capture (Wang et al., 2011)

1.1.3.1 Adsorption

Adsorption is a process that involves the attachment of a gas or liquid to a solid surface (Wang et al., 2011). This attachment could be with (chemical adsorption) or without (physical adsorption) the formation of chemical bonds. Under physical adsorption, the interaction of CO_2 with the solid surface is dominated by the quadrupole moment and electric field gradient (Hedin et al., 2013).

The adsorbent is regenerated using different methods including temperature swing adsorption (TSA) (Hedin et al., 2013; Ishibashi et al., 1996; Mulgundmath and Tezel, 2010), pressure swing adsorption (PSA) (García et al., 2013; Grande, 2012; Mulgundmath and Tezel, 2010), electrical swing adsorption (ESA) (Grande et al., 2009) and moisture swing adsorption (MSA) (Wang et al., 2011). A combination of these methods can also be used for adsorbent regeneration (Ishibashi et al., 1996; Mulgundmath and Tezel, 2010) Adsorption can be employed with both post-combustion and pre-combustion capture (Bui et al., 2018). Among the popular adsorbents are activated carbon, alumina, metallic oxide, zeolites, hydrotalcite microporous polymers and metal-organic framework (MOFs). Activated carbon is cheap, widely available and has a lower affinity for water vapour compared to zeolite (Wang and Song, 2020). However, its CO_2 capacity is lower than those of Zeolites, particularly at low pressures. Zeolites are crystalline microporous

aluminosilicates with large internal specific surface area and volumes (Hedin et al., 2013). Zeolite has adsorption capacity in the range of 0.7-4.0 mmol/g at 0- 40 °C and 0.15 bar (Bae et al., 2013; Hedin et al., 2013; Wang and Song, 2020). The main weakness of Zeolite as an adsorbent is its strong affinity for water vapour which results in low CO_2 uptakes (Bui et al., 2018). MOFs are crystalline porous materials formed by metal ions coordinated with rigid organic linkers. Apart from the application in capturing CO2 from flue gas, MOFs are also used for CO2 separation from biogas, landfill gas and natural gas. MOFs have adsorption capacity in the range of 1.1- 5.8 mmol/g at 25 °C and 0.15 bar (Bae et al., 2013; Wang and Song, 2020).

In addition to these adsorbents, amine-based sorbents are also being investigated. This group of adsorbents is formed by combining amine compounds such as polyethyleneimines (PEI), monoethanolamine (MEA), Pentaethylenehexamine (PEHA), and diethylamine (DEA) with solid adsorbents through either surface immobilization, surface polymerization or surface grafting. They have the potential to reduce the energy consumption of the CO_2 capture process because they combined the lower regeneration heat of the solid absorbents with the fast reaction kinetics, high selectivity for CO_2, high CO_2 capacity, multicycles stability and tolerance to the water of the amine compounds (Ma et al., 2009; Wang and Song, 2020). The current adsorption system may not be suitable for the treatment of power plants and industrial flue gases because of the low adsorption capacity, low selectivity and low impurity tolerance of available adsorbents. Also, at that scale, the volume of the flue gas to be treated pose a challenge as it limits the possibilities of regular swing adsorption. Therefore, recent and most current research efforts in adsorption are directed at improving these characteristics of the adsorbents

1.1.3.2 Cryogenics carbon capture

Cryogenic carbon capture separates CO_2 from the flue gas stream by condensation (Wang et al., 2011). It is a promising and transformational CO_2 capture technology that is suitable for treating flue gas with high CO_2 concentration (>16 mol %) The CO_2 capture level of this process depends on the coldest temperature achieved by the flue gas. At 1 bar and -117 °C, the process is capable of 90% CO_2 capture from typical coal flue gases (Baxter et al., 2019). Although this process produces a liquid CO_2 stream that requires fewer resources to compress, the high costs of refrigeration could potentially increase the cost of the capture

process. Among the advantages of cryogenic capture are, it can recover water from the flue gas, handles impurities in the gas stream and enables energy storage.

1.1.3.3 Membrane absorption

Membrane absorption can be applied in post-combustion capture to capture CO_2 or co-permeation of CO_2 and oxygen. It can also be used in oxyfuel and pre-combustion for air and hydrogen separation respectively. The membrane can be classified as either organic membrane (not suitable for high-temperature application) or inorganic membrane (suitable for high-temperature application). In gas absorption, the membranes act as contacting devices between the gas stream and the liquid solvent. Compared to the other contacting devices such as packed column, membranes are more compact and are not prone to operational problems (such as flooding at high flowrates, entrainment, channelling and foaming) which can lead to difficulties in the mass transfer of CO_2 between gas and liquid phase (Ahmad et al., 2010; Wang et al., 2011). For CO_2 transport across the membrane to occur, the pressure on the liquid and gas sides must be equal. The separation efficiency depends on the partial pressure of the CO_2. Therefore, it is mostly suited for application to flue gas from an oxyfuel or IGCC processes where CO_2 concentration could be well above 20 vol%. Due to the observed challenges with membrane separation of CO_2 and H_2, a tradeoff would have to be made between CO_2 recovery and product purity.

1.1.3.4 Absorption

Absorption involves the separation of CO_2 from the flue gas using solvents. The absorption process can either be by physical absorption which is based on Henry's law or chemical absorption which involves a reaction between CO_2 and solvent.

1.1.3.4.1 Physical absorption

Physical absorption involves CO_2 absorption based on Henry's law. In this technology, the absorption operations take place at high CO_2 partial pressures and low temperature, therefore, it is not economical for flue gas with CO_2 concentration below 15 vol% (Wang et al., 2011; Yu et al., 2012). The CO_2 is desorbed at low pressure and high temperature. The main energy consumption of this technology comes from the pressurization of flue gas. Physical absorption is widely used in industrial processes such as natural gas and hydrogen production. There are commercial processes based on this technology. Among them is the

Selexol process which uses dimethyl ether or propylene glycol as the solvent, Rectisol process which uses methanol as solvent, Morphysorb process which uses morphiline as the solvent, Purisol process which uses N-methyl pyrrolidone as solvent and Flour process which uses propylene carbonate as solvent (Yu et al., 2012). In addition to CO_2, some of these processes like Selexol and Rectisol are also capable of removing H_2S from the flue gas stream.

1.1.3.4.2 Chemical absorption

This involves the removal of CO_2 from flue gases with amine solvents after the combustion of fossil fuel in power plants and industries. The CO_2 rich solvent is regenerated at elevated temperatures to break the Amine-CO_2 bond to produce a CO_2 rich vapour stream and the original solvent (IPCC, 2005). MEA is the most commonly used solvent and the 30 wt% MEA is widely referred to as the benchmark solvent for this process. Other solvents used in CO_2 chemical absorption include piperazine (PZ), diethylamine (DEA), methyldiethylamine (MDEA) etc. Also, blends of these solvents such as MEA/MDEA, PZ/MEA and PZ/MDEA are also used. It is the most matured CO_2 capture technology with a technology readiness level (TRL) of 9 (Bui et al., 2018), therefore, it has been deployed at a commercial scale for CO_2 capture at two coal-fired power plants (Jenkins, 2015; Stéphenne, 2014). The PCC process based on chemical absorption is the focus of this PhD thesis.

Before entering the CO_2 capture system, the flue gas must be processed by removing contaminants such as SO_2, NOx O_2 and particulates and by cooling the temperature to within the range that improves the absorption process. Acid gases such as SO_2 and NOx compromise the absorption performance by reacting with MEA to form unregenerated heat stable salts. Heat stable salts tend to reduce the solvent absorption capacity, increase viscosity and promote foaming. Therefore, the concentrations of the acid gases in the flue gas must be kept within the recommended values. SO2 concentrations below 10 ppm are recommended (Davison, 2007; Li et al., 2016). SO_2 removal is usually achieved by scrubbing the flue gas with limestone ($CaCO_3$) in a Flue Gas Desulphurization (FGD) unit. A valuable product such as gypsum ($CaSO4.2H_2O$) can be derived from this process. The FGD can achieve SO_2 removal efficiency of 95-99%. NOx concentrations should be kept below 5 ppm (Davison, 2007). This can be achieved with Selective Catalytic Reduction, Selective Non-Catalytic Reduction or low NOx burners. Particulate matter such as fly ash is removed by

either electrostatic precipitators or baghouse filters. Particulates promote foaming in the system. Foaming causes operational issues, reduces absorption capacity, lowers mass transfer coefficients and increases the pressure drop in the absorber and stripper. Its formation can be suppressed by the addition of silicon anti-foaming agent (Rabensteiner et al., 2015a).

The oxygen concentration in the flue gas must be reduced to avoid equipment corrosion and losses in solvent capacity. Oxygen concentrations of 1 ppm are recommended for use with MEA in the absence of corrosion inhibitors. Oxygen causes oxidative degradation of alkanolamines like MEA particularly in the absorber (packing and sump), cross heat exchanger and piping leading to the cross heat exchanger (Pinto et al., 2014; Więckol-Ryk et al., 2018). This degradation can be inhibited by the addition of oxygen scavengers such as sodium sulphite (Na_2SO_3), hydroxylamine (NH_2OH) and ethylenediaminetetraacetic acid (EDTA) to the amine solution (Supap et al., 2011). These oxidation inhibitors can be added either directly to the amine or indirectly by contacting through a membrane barrier (Buvik et al., 2021). Also, "salting out" (which is the addition of salts to a solution to increase the ionic strength to decrease the oxygen solubility) can be used to control the oxygen-induced amine degradation (Buvik et al., 2021).

The flue gas entering the absorber must be cooled down to between 40–50 °C to improve the CO_2 absorption process and minimize solvent loss due to evaporation (Wang et al., 2011). The cooling is achieved in a direct contact cooler (DCC) where the flue gas is cooled by a spray of water, this, in addition, saturates the flue gas to the absorber and thereby helps the water balance.

1.1.4 Process description for PCC

The conventional CO_2 absorption process is shown in Figure 1.6. The cooled flue gas enters the CO_2 capture system from the bottom of the absorber where it is contacted counter-currently with a lean solvent of CO_2 loading of 0.1-0.2 mol_{CO2}/mol_{MEA}. As CO_2 is being absorbed, the lean solvent gradually heats up and the temperature in the absorber could reach up to 60 °C. Upon absorption, the scrubbed gas is water washed to remove solvents and then vented to the atmosphere. The rich solvent exits the bottom of the absorber at CO_2 loading of 0.4-0.5 mol_{CO2}/mol_{MEA}. It is heated in a cross-heat exchanger by the hot regenerated lean solvent before being pumped to the top of the stripper where it is

regenerated at temperatures of 100-120 °C and pressures of 1.5-2 atm (IPCC,2005). The regeneration heat is supplied through the reboiler. The regenerated solvent is pumped through the cross-heat exchanger and then it is cooled before it is returned to the absorber. Part of the bottom products from the stripper is sent to the reclaimer unit. Here, the solvent is evaporated and returned to the system. The non-volatile wastes left behind are purged from the system.

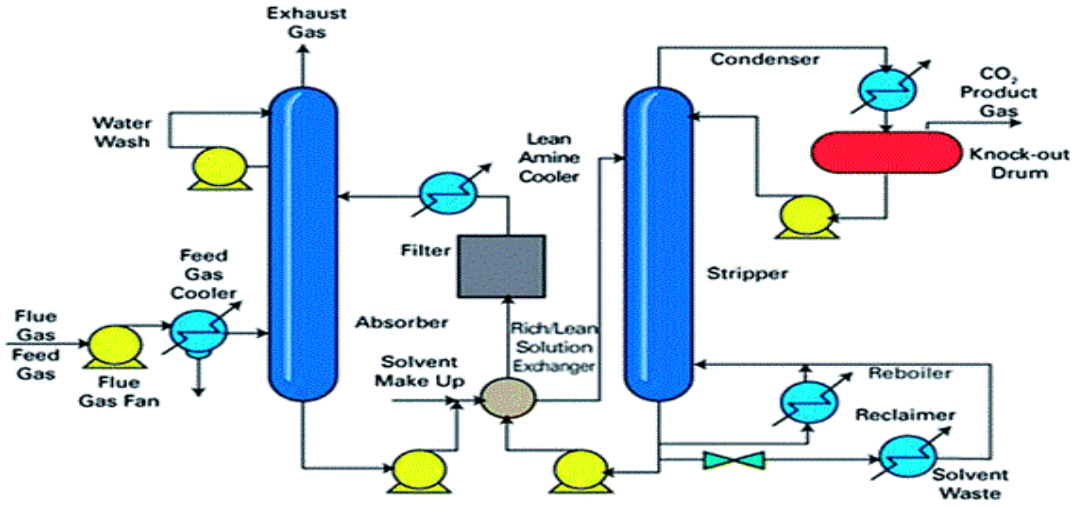

Figure 1. 6 Process flow diagram for solvent-based PCC (Saeed *et al*., 2013)

1.2 Motivation for this study

As earlier mentioned, the PCC process can be added to an existing power plant without the plant undergoing any radical change. It is also the most mature technology to capture CO_2 from fossil fuel-fired power plants (Sreedhar *et al*., 2017; Wang *et al*., 2011). Despite these advantages, the cost and the energy consumption of the process are still very high. The high costs (capital and operating) of the process are due mainly to the huge size of the packed bed (PB) (i.e absorber and stripper). For instance, a 250 MW_e combined cycle gas turbine (CCGT) power plant emitting 2340 tonnes of CO_2 per day will require a PCC plant with two absorbers (each 9.5 m x 30 m in dimension) and one stripper (8.2 m x 30 m) (Canepa et al., 2013). The generalized pressure drop correlation (GPDC) method is mostly used for estimating the diameter of the PBs used in large-scale PCC plants (Agbonghae et al., 2014; Dutta et al., 2017; Lawal et al., 2012; Montañés et al., 2017; Nittaya et al., 2014).

However, the GPDC method may not give the correct estimates of the diameter due to the limited correlation curves available in the range used to design the absorbers and the strippers. Thus, an alternative scale-up method is required to explore the possible size reduction for the absorber and the stripper.

The size of the absorbers and the strippers can also be reduced by using a rotating packed bed (RPB). RPB enhances mass and heat transfer in the PCC process due to the presence of centrifugal acceleration. This leads to a significant size reduction when used for PCC. So far, modelling, simulation and process analysis of CO_2 capture in RPB have been at a pilot-scale (Borhani et al., 2018; Im et al., 2020; Joel et al., 2014; Kang et al., 2014; Oko et al., 2018; Thiels et al., 2016). There is a need to have a comprehensive study to quantify the requirements for CO2 capture in an MEA-based large-scale RPB absorber.

The high energy consumption of the PCC process results from a large amount of steam used for solvent regeneration. For the conventional PCC process (with 30 wt% MEA), the energy consumptions are in the range of 3.2-5 GJ/t_{CO_2} (Canepa et al., 2013; Oh et al., 2018; Knudsen et al., 2009; Luo and Wang, 2017; Mimura et al., 1995; Otitoju et al., 2020). Despite various process modifications (heat integration, vapour re-compression, split flow, absorber intercooling, selective exhaust gas recirculation, the addition of heat pumps (Diego et al., 2018; Frimpong et al., 2019; Rezazadeh et al., 2017; Song et al., 2017; Steeneveldt et al., 2006) the energy consumption of the MEA-based PCC process still high. In addition to this, it is highly corrosive and volatile. It also has high susceptibility to thermal degradation (above 120 °C) and oxidative degradation (Otitoju et al., 2021).

The use of PZ as a solvent for the PCC process is a possible route to an energy-efficient process. PZ has been proposed as a possible replacement for the 30 wt% MEA (Freeman et al., 2010). Compared to 30 wt% MEA, it has a higher CO2 loading capacity, lower volatility, and lower regeneration energy. It also reacts faster with CO2 and has been used as a rate promoter in blends with other solvents such as MEA, DEA, and MDEA, AMP (Cullinane and Rochelle, 2006; Ghalib et al., 2017; Hemmati et al., 2019; Li et al., 2013). Its cyclic nature means that it can be regenerated at elevated temperatures (>120 °C) and pressures (up to 14 bar) without significant degradation. A recent pilot plant study has demonstrated that the energy consumption of the solvent-based PCC process can be reduced by 10-20 % using

PZ as solvent (Gao et al., 2019). This has motivated the use of PZ as a solvent in the PCC process to explore the energy-saving benefits arising from its superior properties to MEA. The 40 wt% PZ is generally referred to as the standard concentration for the solvent-based PCC process.

1.3 Aim and objectives of this PhD study

This PhD research aims to reduce the energy consumption and cost of the solvent-based PCC process through modelling, simulation and performance evaluation of the process using different solvents (monoethanolamine and piperazine), different process configurations (standard, absorber intercooling and absorber intercooling with advanced flash stripper) and technologies (packed bed (PB) and rotating packed bed (RPB)). The research objectives include the following;

- A comprehensive literature review of the solvent-based PCC using PB and RPB.
- Model development, model validation, model scale-up using a newly proposed scale-up method and process analysis of the MEA-based PCC process in PB using Aspen plus®.
- Model development, model validation, model scale-up and process analysis of PCC process using PZ in PB using Aspen Plus®.
- Technical and economic performance assessment of PCC process using PZ in PB with Aspen Plus® and Aspen Process Economic Analyzer®.
- Model development, model validation, model scale-up using a newly proposed iterative scale-up method and process analysis of MEA based RPB absorber with Aspen Custom Modeller®.
- Technical and economic performance comparison of MEA based PCC process using RPB absorber to PCC process using MEA and PZ in PB absorber.

1.4 Novel contributions of this study

Based on the literature review presented in chapter 2 and the summary in section 2.4, the novel contributions of the studies in this thesis are as follows:

I. A new method to calculate the diameter of the absorber and the stripper used in CO_2 absorption was developed and validated between two existing pilot-plant sizes. The method is based on the gas flooding velocity in the columns. This is in contrast to the

traditional GPDC method where the diameter of the absorber and stripper is calculated by assuming a pressure drop. According to Sinnott (2005), the recommended pressure drop range for packed column design is 15-50 mm-water/m of packing. However, within this range, experimental data are only available for pressure drop curves at 21 and 42 mm-water/m of packing on the GPDC chart. This limits the choice of pressure drops that can be assumed within this range to only the two mentioned above. In addition to this, interpolation of pressure drop data on the GPDC chart is cumbersome and often lead to inaccurate results. The new method proposed in this study addresses the limitations of the GPDC method as it does not require pressure drop assumption or data interpolation to be used. It is an algebraic equation derived for the flooding velocity from the flooding point experimental data reported in the literature. This attempt is the first as far as open literature is concerned. This method was applied to scale up a pilot-scale PCC model developed in Aspen Plus® to a large-scale PCC plant for a 250 MWe CCGT power plant. It was found that smaller equipment sizes and process parameters can be achieved using the new method compared to the GDPC method.

II. Extensive studies have been carried out on the technical and economic assessment of the PCC process using MEA in PBs (Abu-Zahra et al., 2007a; Agbonghae et al., 2014; Alhajaj et al., 2016; Li et al., 2016). These studies are based on a reliable closed-loop model. However, modelling and simulation studies of the PCC process using PZ in PB have focused either on the standalone absorber (Moioli and Pellegrini, 2015; Sachde et al., 2013; Zhang et al., 2017) or the standalone stripper (Lin et al., 2016; Madan et al., 2013). Although standalone models are useful in identifying key performance trends and process parameters, they do not give realistic predictions of the process as communications between process units is unidirectional. Considering that the PCC plant exists in closed-loop in real life, thus a closed-loop model is required to accurately predict its behaviour. In this thesis, a closed-loop model of the PCC process using PZ as solvent is developed and validated at the pilot scale. This is followed by the scale-up of the validated pilot-scale model to a large-scale PCC process capture model for flue gas from a 250MW_e CCGT power plant.

III. The technical and economic assessment of the large-scale PCC process using different process configurations and PZ concentrations is demonstrated in this PhD thesis for the first time for a 250 MW_e CCGT power plant.

IV. Previous studies on CO_2 capture with RPB absorber (Borhani et al., 2018; Im et al., 2020; Jassim et al., 2007; Joel et al., 2014; Kang et al., 2014; Thiels et al., 2016) have reported that the size of the column could be significantly reduced by using RPB absorber. Joel et al. (2014) reported a 12 times volume reduction factor when an RPB absorber was used in place of a PB absorber for CO_2 capture. In a recent study, Im et al., (2020) reported that RPB could achieve the same absorption operations as PB with 3 times less packing volume in the absorber. For these studies, significant size reduction benefits were reported for small RPB rigs handling flue gas flowrate of 0.66 kg/s or less. The significant reduction in packing volume could potentially result in lower capital and operating cost for the large-scale CO_2 capture process. Detailed scale-up procedure and technical and economic analysis of CO2 capture in an MEA-based large-scale RPB absorber has not been reported in the literature. MEA concentrations of 55-75 wt% are used in this thesis. Thus, the technical and economic implications of CO_2 capture in large-scale RPB absorber at higher MEA Concentrations (55-75 wt%) need to be assessed. In this thesis, a customized model of the RPB absorber was developed in ACM®. The absorber model was validated at pilot scale before being scaled up (using an iterative scale-up method proposed in this thesis) to process flue gas from a 250 MW_e CCGT power plant. In addition, technical and economic assessment was carried out to quantify the size and costs requirements of CO_2 capture in an MEA-based large-scale RPB absorber.

1.5 Scope of this study

The main focus of the work presented in this thesis is the modelling, simulation and analysis of the solvent-based PCC process.

- This study is limited to CO_2 capture using MEA and PZ.
- Modelling for the other aspects of the CCUS train such as power plants, CO_2 transports, flue gas desulphurisation and storage are not covered in this study. The studies in Chapters 3 and 4 utilize the integrated model of the PCC process developed in Aspen Plus® for CO_2 capture in PBs.

- The studies in Chapters 5 and 6 looks at model development, model validation, model scale-up and technical and economic analysis of CO_2 capture in large-scale RPB absorber using MEA solvent. These studies involving RPB is limited to only the absorber component and MEA solvent.
- All studies performed in this thesis are based on steady-state models.
- The life-cycle-analysis (LCA) of the PCC process is not covered in this study.

1.6 Research Methodology

The methodology used in this thesis is presented in Figure 1.7. It highlights the stages involved in each route used in the thesis.

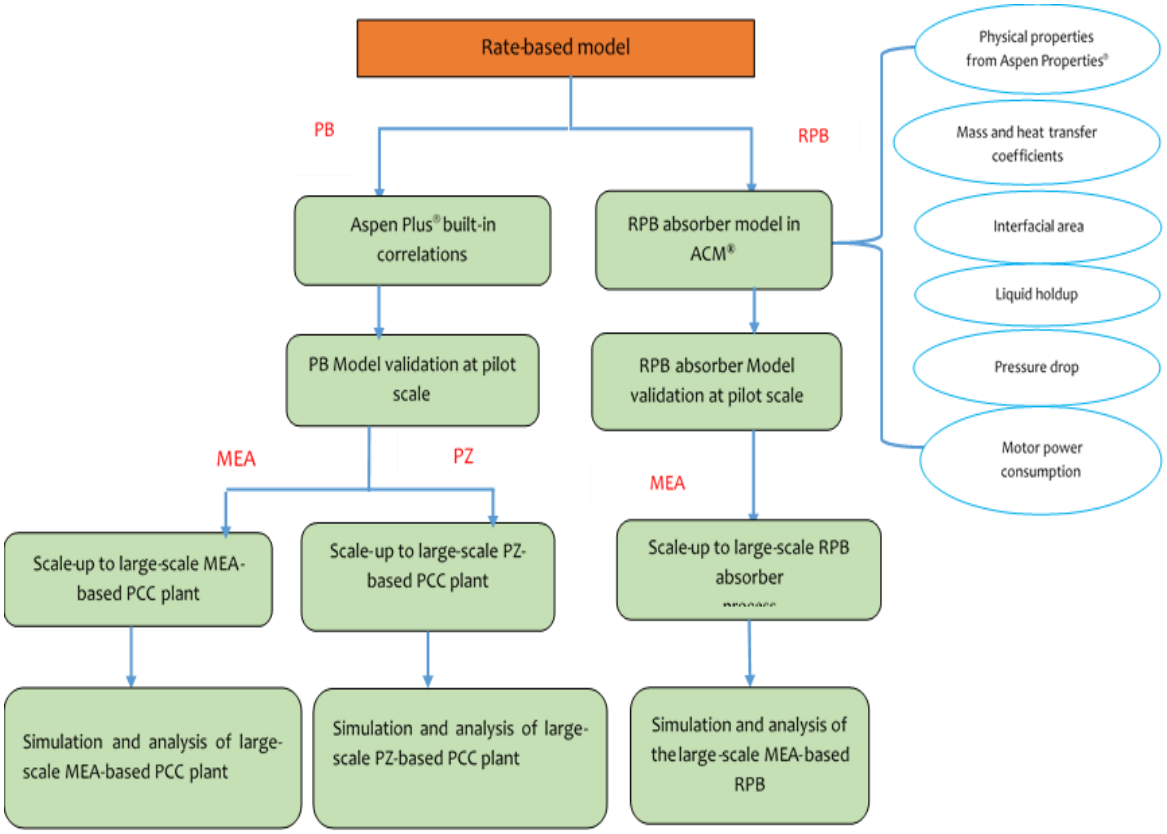

Figure 1.7 Overview of the methodology used in this thesis

1.7 Research tools to be used for this study

1.7.1 Aspen Plus®

Aspen Plus® is a very useful tool for the simulation and analysis of chemical processes. It contains model libraries of various unit operations. It is a powerful and innovative software with a large database of pure components and phase equilibrium data, conventional

chemicals, electrolytes, solids, and polymers. It is useful for the modelling of batch and customs processing units, online performance monitoring, faster troubleshooting, and real-time optimization. It provides a convenient platform to develop and simulate the CO2 capture process as it requires only the selection and input of key design and operating parameters. The Aspen Plus® V8.4 was used for the work presented in Chapters 3 and 4 of this thesis.

1.7.2 Aspen Custom Modeller®

ACM is a modelling platform that is used for quick custom model development and simulation. It allows users to develop and customise a process model that can run in four different modes: (1) steady-state (2) dynamic state, (3) optimization and (4) parameter estimation. In addition, it can be linked to Aspen plus®. This gives ACM unfettered access to the Aspen Properties databank to collect useful data for the calculation of physical and chemical properties. Furthermore, it allows for custom procedures to be developed and used to calculate model variables. This help in reducing the size and number of model equations thereby making the ACM model more compact. However, the use of the procedure functionality depends on the needs of the user. One more other feature of ACM is that the model developed on this platform can be easily packaged and exported into Aspen Plus® where the ACM model can be used interactively with other model blocks to build and test new processes. The ACM® V11 was used for the work presented in Chapters 5 and 6 of this thesis.

1.8 Outline of the Thesis

This thesis consists of seven chapters. The rest of the chapters in the thesis are as follows: **Chapter 2** focuses on the reviews of existing experimental and modelling and simulation studies of solvent-based PCC in PBs and RPBs. Summary based on the review is also included.

Simulation and scale-up of MEA-based PCC process using a PB are presented in **Chapter 3**. This includes model development and model validation at the pilot scale. A new method scale-up method for the solvent-based PCC is proposed and used to develop a large-scale PCC process. Results of the steady-state analysis performed using this model are also presented.

In chapter 4, simulation and technical and economic assessment of the solvent-based PCC process using PZ in PB is presented. This includes model development, model validation at pilot scale, model scale-up and technical and economic performance analysis. Results of the technical and economic analysis performed using this model are also presented.

The steady-state model development for the RPB absorber is presented in **Chapter 5**. This includes a description of the operating principles of the RPB absorber and the various equations and correlations used to develop the model.

In Chapter 6, the results of the model validation, model scale-up and technical and economic performance analysis of a large-scale MEA-based RPB absorber is presented. Results and discussions from the different analyses performed using the RPB absorber model are also presented.

Finally, conclusions drawn from this thesis and the recommendations for future works are presented in **Chapter 7.**

Chapter 2: Literature Review

2.1 Overview

This chapter aimed at reviewing previous research activities on experimental, modelling and simulation of the solvent-based PCC process in PB and RPB. The review of existing pilot plants and commercial deployment of the PCC process is discussed in Section 2.2. Section 2.3 presents the principles of modelling, a review of model-based studies of the PCC process using MEA as a solvent and a review of model-based studies using PZ as a solvent. modelling and simulation as well as the scale-up of the solvent-based PCC plants in PB. Section 2.4 presents a review of existing RPB absorber rigs used for CO2 capture, commercial deployment of RPB and modelling and simulation studies of the RPB absorber for solvent-based PCC process using MEA as a solvent. The summary of the literature review is presented in Section 2.5

2.2 Solvent-based PCC process using packed bed (PB) technology

2.2.1 Review of PCC Pilot-plant worldwide

Several research activities on solvent-based PCC have been conducted at pilot plants around the world. A brief description of different pilot plants and a summary of the past research activities conducted at the plants were presented by Wang et al. (2011). Operational issues that can be encountered in pilot plants and methods to resolve them before full-scale design and operations were presented by Gelowitz et al. (2013). In a later publication, Oko et al. (2017) gave a summary of the successful demonstration trials of the solvent-based PCC plant integrated into real power plants. Recently, a comprehensive review of research facilities and pilot plants in thirty-seven locations across the world was carried out by Nessi et al. (2021) with a focus on the evolution of different solvents as well as the structural and operating features that influenced these pilot plants performance. A few of the PCC pilot plants and key information about their operation are shown in Table 2.1. These pilot plants have been arranged according to their CO2 capture capacity and column sizes from the smallest to the biggest.

Table 2.1 Summary of PCC pilot plants worldwide

Pilot plant	Location	Absorber Dimension	Stripper Dimension	Flue gas flow rate	Solvents	CO_2 capacity	Initial data collection	Reference
Laboratory of Engineering Thermodynamic	University of Kaiserslautern, Germany	0.125 m x 4.20 m; WS: 0.125 m x 0.42 m	0.125 m x 2.52 m; WS: 0.125 m x 0.42 m	30-110 kg/h	30 wt% MEA, BASF 1 &2 solvents	N/A	2009	(Mangalapally et al., 2009; Notz et al., 2012)
CO2 Separation Plant (CO_2SEPPL)	Durnrohr, Austria	0.15 m x 12 m; WS: 0.15 m X 2 m	0.1 m x 8 m WS: 0.1 m X 2 m	50-120 m^3/h	30 wt% MEA, 37.6 wt% PZ, 28 wt% AMP+ 17 wt% PZ	0.6 t/day	2010	(Rabensteiner et al., 2015b, 2015a)
Pilot-scale Advanced CO2 Capture Technology	University of Sheffield, UK	0.30 m x 8 m; WS: 0.30 m X 1.2 m	0.30 m/ 8 m No WS	160-250 Nm^3/h	30-40 wt% MEA	1 t/day	2012	(Akram et al., 2016)
Technology development pilot plant	University of Regina, Canada	0.3 m x 10 m	0.324 m x 10 m	200 Nm^3/h	30 wt% MEA, RS1, MEA+MDEA	1 t/day	2000	(Gelowitz et al., 2013; Nessi et al., 2021)
CSIRO Tarong	Queensland, Australia	0.35 m x 7 m WS: 0.35 m x 1.561 m	0.25 m x 7 m WS: 0.25 m x 1.12 m	500-900 kg/h	30 wt% MEA and 40.8 wt% PZ	2.7 t/day	2010	(Cousins et al., 2014, 2011)
Separation[a] Research Programme (SRP)	University of Texas at Austin, USA	0.427 m x 6.1 m No WS	0.427 m x 6.1 m No WS	600-1500 m^3/h	30 wt% MEA, 40 wt% PZ and K_2CO_3+PZ	3-6 t/day	2006	(Chen et al., 2013; Dugas, 2006; Seibert et al., 2011)

Pilot plant	Location	Absorber Dimension	Stripper Dimension	Flue gas flow rate	Solvent	CO_2 capacity	Initial data collection	Reference
National carbon capture centre	Alabama, USA	0.66 m x 12 m	0.59 m x 4 m	1656-2376 kg/h	30 wt% PZ	10 t/day	2011	(Gao and Rochelle, 2020; Rochelle et al., 2019)
The Esbjerg CESAR EU project	Esbjerg power station, Denmark	1.1 m/17 m WS: 1.1 X 3 m	1.1 m/10 m WS: 1.1m X 3m	5,000 Nm^3/h	30 wt% MEA, CASTOR 1 & 2, CESAR 1&2	24 t/day	2006	(Knudsen et al., 2009; Razi et al., 2013)
Enel pilot plant	Brindisi, Italy	1.5 m x 45 m; WS: 1.5 m X 4 m	1.3 m x 31 m WS: 1.3 m x 3m	3,000-12,000 Nm^3/h	20-30 wt% MEA, KS-1^{TM}, HiCapt^{TM}	48-60 t/day	2011	(Enaasen et al., 2016; Lemaire et al., 2014)
The CO2 technology centre Mongstad	Bergen, Norway	Rectangular: 3.5 x 2 m; height: 62 m	2.2 m x 30 m	40,000-60,000 Nm^3/h	30-40 wt% MEA and other solvent mixtures	80 t/day	2012	(De Koeije et al., 2011; Montañés et al., 2017)

WS: Washing section, [a]The experimental data from this pilot-plant was used for model validation in this thesis.

These pilot plants have been used to investigate various process improvements of the CO_2 capture plant including solvents performance evaluations (Frimpong et al., 2019; Idem et al., 2015; Liu et al., 2022; Nwaoha et al., 2017; Zhang et al., 2017), modification of process configurations and heat integration (Khalifa et al., 2022; Krótki et al., 2020; Moore et al., 2021; Rochelle et al., 2019; Stec et al., 2015), different packings, mass transfer and separation performance (Mangalapally and Hasse, 2011; Tsai et al., 2011). Experimental data collected at these pilot plants are valuable sources of data for model validation. The successes recorded in the pilot plants tests and demonstration trials have led to the commercial implementation of the solvent-based PCC process.

2.2.2 Commercial deployment of solvent-based PCC process

The solvent-based PCC process has been deployed at large-scale to capture CO_2 from the flue gas of coal-fired plants at Boundary Dam (BD) in Canada and Petra Nova (PN) project in the USA (Montañés et al., 2017a). These commercial PCC plants are described in the following sections.

2.2.2.1 Boundary Dam (BD) CCS plant

The BD CCS plant is the first commercial CCS plant to be built in the world. It became operational in 2014. It is located in Saskatchewan, Canada and retrofitted to a lignite (coal) fired power plant with a gross and a net capacity of 160 MW_e and 110 MW_e respectively (Mantripragada et al., 2019). The BD CCS was built at the cost of about US $1.3 billion and was financed by a partnership including SaskPower, Canadian and Saskatchewan governments and private sectors (SaskPower, 2012). It has a CO2 capture capacity of 1 million t/yr and operates at 90 % CO2 capture level. The BD CCS uses the Cansolve solvent which is an advanced amine solvent developed by Shell. This solvent in the BD is regenerated using a low-pressure steam from the steam cycle. This results in derating the power output of the steam turbine and is therefore the main parasitic load in the BD CCS. It also increases the cost of electricity in the BD CCS plant. The captured CO2 is compressed and transported Cenovus energy for enhanced oil recovery (EOR) (Stéphenne, 2014).

2.2.2.2 The Petra Nova (PN) CCS plant

The PN CCS plant is the world largest commercial CCS project. It is owned by the Petra Nova Parish Holdings PCC and sequestration project and became operational in 2017

(Kenneth, 2017). It is located in Texas, USA and retrofitted to a slipstream of flue gas from a bituminous coal-fired power plant with a gross and a net capacity of 240 MW_e. It is based on the Mitsubishi Heavy Industries (MHI) KM CDR® process and can capture 1.6 million t/yr of CO2 at 90% capture level using the Mitsubishi KS-1™ solvent (Energy, 2014; Jenkins, 2015; Mantripragada et al., 2019). The solvent in the PN CSS is regenerated using the steam supplied by a dedicated natural gas co-generation power plant. This, therefore, does not lead to the derating of the coal-fired plant to which the PN CCS is integrated. It also does not increase the cost of electricity. The downside of this is that additional capital and operating expenses are needed for the natural gas co-generation plant. The captured CO2 in the PN CCS is used for enhanced oil recovery.

2.3 Model-based studies of solvent-based CO_2 capture in PB

2.3.1 Principles of modelling

The solvent-based PCC process via chemical absorption involves simultaneous chemical reactions and gas-liquid mass transfers that are best described using either the equilibrium stage model approach or the rate-based model approach. The differences between these two approaches are shown in Figure 2.1. The equilibrium stage approach assumes a well-mixed theoretical stage where the vapour and liquid are at equilibrium (Lawal *et al*., 2009). This assumption is unrealistic as gas-liquid equilibrium is hardly ever attained in the PCC process where reactive absorption takes place. This makes the equilibrium stage model less accurate for modelling solvent-based PCC processes (Kenig *et al*., 2001; Schneider *et al*., 1999). The rate-based approach accounts for multicomponent mass transfer, heat transfer and chemical reactions within the columns. This makes it more appropriate for describing the solvent-based PCC process as it gives an accurate representation of the process (Kucka *et al*. 2003; Lawal *et al*., 2009).

The gas-liquid mass transfer in the rate-based model approach is described using different theories such as the penetration theory (Danckwerts, 1970; Rahimpour and Kashkooli, 2004) the surface renewal theory (Danckwerts, 1951), and the two-film theory (Biliyok et al., 2012; Lawal et al., 2009; Nittaya et al., 2014; Whitman, 1924). The two-film theory is the most widely used among these theories. In the two-film theory, the mass transfer within the film arises from steady-state molecular diffusion and mass transfer resistance is assumed in the vapour film and liquid film (Kenig *et al*., 2003). The Maxwell-Stefans

equations are used to describe the diffusion in the film and the compositions of the bulk liquid phase and the bulk gas phase are assumed to be uniform.

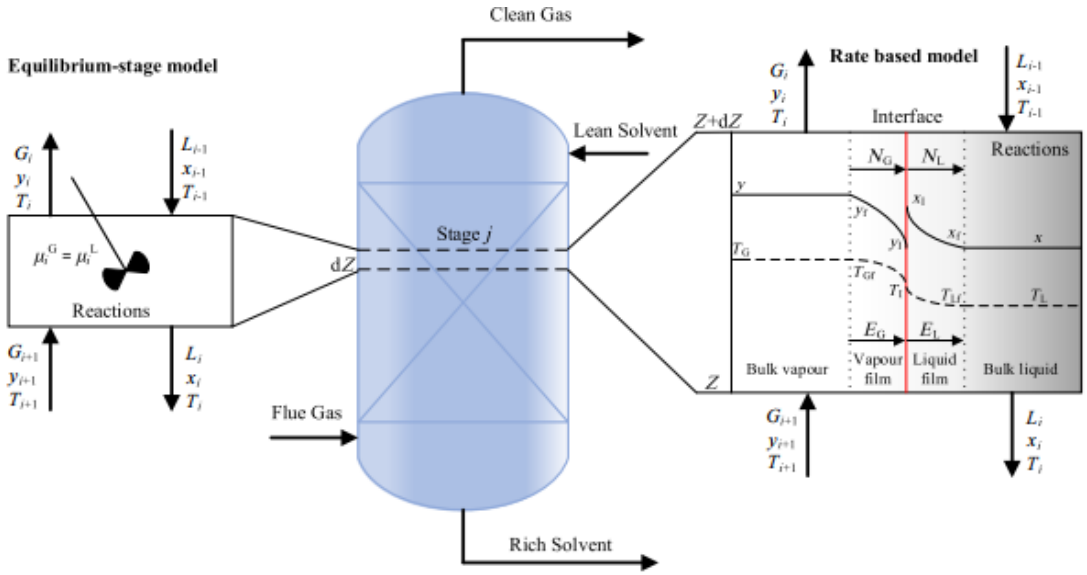

Figure 2.1 The equilibrium-stage model and rate-based model approaches for the solvent-based PCC process

The reaction of CO_2 with an amine in the solvent-based PCC process is described using three reaction mechanisms which are the Zwitterion mechanism, termolecular mechanism and the base-catalysed hydration mechanism. The details of these reaction mechanisms have been extensively discussed in the literature (Aboudheir et al., 2003; Derks et al., 2006; Littel et al., 1992). The reaction kinetics of fast-reacting solvents such as MEA and PZ can be approximated assuming these reactions reach equilibrium. For solvents such as DEA and MDEA that react slowly, this assumption is not enough, an accurate reaction kinetic is therefore needed to describe the reactions (Zhang et al., 2009). In first principle modelling, this reaction kinetic is accounted for using the enhancement factor based on pseudo-first-order reaction.

Thus based on the level of details required in the mass transfer and reaction kinetics, the model of the solvent-based PCC can be developed according to the level of complexities shown in Figure 2.2. The level of accuracy increases with complexity thus level 5 is the most accurate as it accounts for mass transfer and reaction kinetics via the rate-based approach. Level 1 is regarded as the least accurate of all the levels.

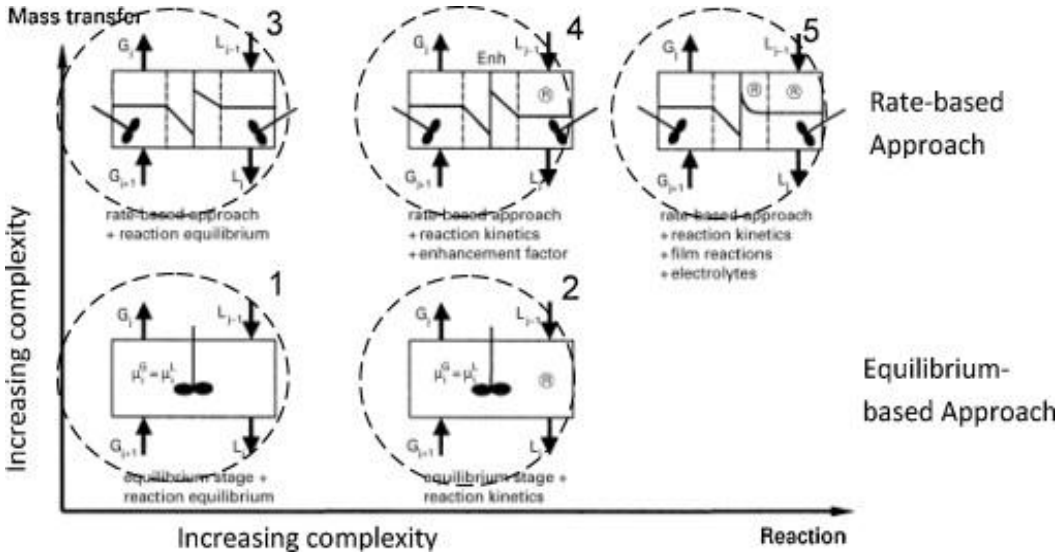

Figure 2.2 Complexity in model level for solvent-based PCC process (Kenig et al., 2001; Wang et al., 2011)

2.3.2 Modelling and simulation studies of the PCC process using MEA solvent in PB

MEA is the most widely used solvent to capture CO_2 in the PCC process, and the 30 wt% MEA is considered as the benchmark solvent. There are many studies on the modelling and simulation of the PCC process using MEA in PB. These studies include modelling and simulation of single components such as absorber and stripper (Kvamsdal., 2009; Lawal *et al*., 2009; Zhang *et al*., 2009), the whole solvent-based PCC plant (Gaspar and Cormos, 2012; Harun et al., 2012; Lawal et al., 2010; Mostafavi et al., 2021), integration of the PCC plant to CO_2 emitters such as power plants (Ayyad et al., 2021; Biliyok and Yeung, 2013; Lawal et al., 2012; Mac Dowell and Shah, 2014). Among the popular software employed to carry out the modelling and simulation studies of the solvent-based PCC process is Aspen plus®, gPROMS®, Aspen HYSYS®, K-Spice®, MATLAB®, Modelica® and Unisim®.

Zhang *et al.* (2009) developed a rate-based absorber model in Aspen Plus® for the PCC process using MEA solvent. This model was validated with pilot plant experimental data and accurately predicted the pilot plant measurements for lean and rich CO_2 loadings, capture level and temperature profile. The effect of different mass transfer correlations on the predictions ability of the rate-based model was explored by Khan *et al*. (2011). It was found that the model gave better predictions with the Onda et al. (1968) correlation compared to Rocha *et al*. (1996) and Higbie, (1935) correlations. The suitability of these

mass transfer and hydraulic correlations is based on the type of amine, packing and flow conditions. It is therefore necessary to benchmark the correlations against experiments carried out based on a range of operating conditions and different packing types (Gaspar and Cormos, 2012).

Razi *et al*. (2013) investigated the influence of mass transfer coefficient correlation, kinetic models and effective interfacial area correlation on the model predictions of pressure drop, CO_2 capture level and temperature profiles in the columns. It was found that the accuracy of the model predictions relied greatly on the kinetic model and mass transfer correlations. A comprehensive sensitivity analysis of model parameters and optimization of the specific total annual cost of the solvent-based PCC process using MEA was carried out by Arias *et al*. (2016). Results showed that the temperatures of the rich solvent, lean solvent and flue gas are highly sensitive to the specific total annual cost. Garcia *et al*. (2017) developed and validated a stripper model of the PCC process in Aspen Plus®. The model predictions of the desorbed CO_2 flow rate, lean loading and lean temperature agree with experimental data. Model analysis showed that heat loss depends on the insulation in the PCC plant rather than on the solvent flow rates and reboiler duty.

Additionally, studies also focussed on the evaluation of process configuration modifications (Karimi et al., 2011; Li et al., 2016; Mostafavi et al., 2021), evaluation of solvent performance (Abu-Zahra et al., 2007b, 2007a), and scale-up based on the GPDC method to study the requirements of large-scale PCC process (Canepa et al., 2013; Luo and Wang, 2017; Otitoju et al., 2020). These studies showed that the reboiler duty and L/G ratio are key parameters that influence the cost and capture efficiency of the solvent-based PCC process.

Mostafavi et al., (2021) proposed combinations of process modifications such as absorber intercooling, lean vapour recompression and parallel exchanger arrangement to reduce the reboiler duty and cost of the PCC process. They found that the combination of the absorber intercooling and the lean vapour recompression resulted in an 8% reduction in steam consumption for regeneration and consequently a significant reduction in operating and total expenses. These complex process configurations however resulted in higher capital expenditure. Studies on the performance of solvent have shown that there is a

need for an alternative solvent with lower regeneration energy, high reactivity with CO_2, high resistance to degradation and is environmentally friendly (Zhou et al., 2010).

2.3.3 Modelling and simulation studies of the PCC process using PZ as a solvent in PB

Based on the review presented in section 2.3.2, the solvent-based PCC process using the 30 wt% MEA benchmark solvent has been studied severally. The downside of MEA solvent is that it is volatile, corrosive and requires high regeneration energy. It is also highly susceptible to oxidative and thermal degradation above 120 ^oC. Despite several process configuration modification efforts including absorber intercooling, lean vapour re-compression, heat integration, split flow addition of heat pumps and selective exhaust gas recirculation, the energy consumption of the solvent-based PCC process using MEA solvent is still high (Diego et al., 2018; Frimpong et al., 2019; Khalifa et al., 2022; Rezazadeh et al., 2017; Song et al., 2017; Steeneveldt et al., 2006). Mostafavi et al. (2021) pointed out that a significant reduction in the regeneration energy can be achieved through the use of an alternative solvent to MEA than through the modification of the process configuration.

PZ has been proposed as a possible replacement for MEA as a solvent for the PCC process (Freeman et al., 2010). It is highly reactive with CO_2 and has previously been used as a reaction rate promoter in blends with other amines such as MEA, MDEA, DEA (Zhang et al., 2017). It has been demonstrated that it can be utilized as a single solvent for the solvent-based PCC process (Rochelle et al., 2011). Compared to MEA, PZ has lower volatility, twice absorption rate, higher resistance to degradations (oxidative and thermal) and higher CO_2 absorption capacity (Chen et al., 2017; Rochelle et al., 2019). These superior properties of the PZ to MEA have led to more interest in PZ being used for CO_2 capture. The earliest studies on the suitability and performance of PZ as a solvent for PCC were conducted at the SRP pilot plant using the 40 wt% PZ. This concentration is generally referred to as the benchmark for the PZ process. In addition to this, various process modifications such as absorber intercooling, two-stage flash and flash skid stripper were tested with 40 wt% PZ solvent to reduce the energy consumption of the capture process. Results from these early pilot plant tests indicated that a more energy-efficient CO_2 capture process could be developed with PZ as solvent.

The performance parameter of 30 wt% MEA and 40 wt% PZ are compared to each other in Table 2.2. Despite its many advantages, PZ is limited by solid formation particularly in the lean stream below at a temperature less than 20 °C. At these conditions (lean CO_2 loading and low temperature), PZ forms Piperazine hydrate (PZ·6H2O(s)) which could result in blockage in the lean solvent line (Rabensteiner et al., 2015a). This could occur during plant start-ups and shutdowns. In situations where temperatures drop below certain values, the lean solvent line is heated to prevent solid formation.

Table 2.2 Comparison of Performance parameters of the benchmark 30 wt% MEA against 40 wt% PZ

Parameters	Unit	30 wt% MEA	40 wt% PZ	Reference
$K_{tot,\ average}$ at 40 °C	mol/s.Pa.m^2	4.3	8.5	(Chen et al., 2017)
Viscosity at 40 °C	Pa.s	0.003	0.011	(Chen et al., 2017)
CO_2 Capacity	mol_{CO2}/mol_{amine}	0.5	0.79	(Chen et al., 2017)
The heat of absorption	kJ/mol_{CO2}	85	75	(Svendsen, 2007)
Oxidative degradation @ 55 °C	$mmol_{amine}$/kg-hr	12	1.1	(Freeman et al., 2010)
Thermal degradation Amine loss at 150 °C	% per week	11	0.44	(Freeman et al., 2010)
Thermal stability	T_{max} °C	120	163	(Li et al., 2013)
Max. regeneration Pressures	bar	2.2	14.3	(Chen et al., 2017)
Volatility at lean loading, at 40 °C	ppm	31	8	(Nguyen et al., 2010)

There are several studies on CO_2 capture using PZ of concentration ranging from 30 wt% to 40 wt% (Chen et al., 2017; Cousins et al., 2014; Gao and Rochelle, 2020; Plaza and Rochelle, 2011; Rabensteiner et al., 2015a, 2015b; Rochelle et al., 2019; Van Wagener et al., 2013). Pilot-scale testing has shown that the regeneration energy consumption of the solvent-based PCC process can be reduced by 14% using 37.5 wt% PZ compared to 30 wt% MEA (Rabensteiner et al., 2015a). Another study achieved regeneration energy of 2.9

GJ/t_{CO2} using 40 wt% PZ. This represents a 15% reduction in regeneration energy consumption compared to 30 wt% MEA (Gao et al., 2019). Process configuration modifications such as absorber intercooling and an advanced flash stripper have demonstrated that the regeneration energy consumption of 1.9-2.5 GJ/t_{CO2} can be attained using 30 wt% PZ as a solvent for CO_2 capture from flue gas of a coal-fired power plant (Gao et al., 2019).

In an absorber model developed in Aspen Plus®, Plaza and Rochelle, (2011) found that the CO_2 capture level can be increased by 10% using absorber intercooling particularly when absorber operations are close to critical LG ratio. The Adiabatic, in-and-out, and pump-around intercooling are the different types of absorber intercooling that have been implemented and tested. The operational benefits of each of these intercooling types to the PCC process using PZ were quantified by Frailie, (2014). Also in addition to the standard stripper, the two-stage and advanced flash strippers have been modelled and tested at pilot scale (Frailie, 2014; Madan et al., 2013; Van Wagener et al., 2013) with flue gas from a coal-fired power plant. An 11% reduction in the energy demand was achieved in an optimized two-stage flash stripper compared to the standard stripper (Madan et al., 2013). The advanced flash stripper also achieved a 25% reduction in energy demand compared to the two-stage stripper (Lin et al., 2016).

Even though the capture efficiency and energy performance improvements achieved with the modified process configurations are important, the additional capital investments required to procure the heat exchangers and other extra process equipment need to be determined. This will help in the objective ranking of these process configurations in terms of energy performance and cost. An economic assessment of the different process configurations using the total annual cost (TAC) and the cost of CO2 capture (CCC) provide a more rigorous and objective assessment of the PCC process. The CCC has been used severally to rank the performance of different process configurations since it accounts for the capital, operating and maintenance cost as well as the energy performance of the PCC process (Li et al., 2016; Manzolini et al., 2015; Schach et al., 2010). Thus, in addition to the energy performance assessment of the different process configurations of a large-scale PCC process using 30, 35, and 40 wt% PZ concentrations, this thesis also carried out the

economic performance assessment of the different process configurations using the TAC and CCC as key economic performance indicators.

2.4 Solvent-based PCC process using rotating packed bed (RPB) technology

2.4.1 Review of RPB absorber rigs for solvent-based PCC process

Many research activities on CO_2 capture in RPB have been conducted globally. Detailed descriptions of the different RPB rigs and experimental studies around the world was presented by Wang et al. (2015). A few of the RPB rigs and key information about their operation are presented in Table 2.3. These pilot-plant scale absorber rigs have been used to study different aspects of CO_2 capture from a mixture of gases. Jassim et al. (2007) examined the CO_2 capture efficiency in an RPB absorber using MEA concentrations of 30 55, 75 and 100 wt%. Yi *et al*. (2009) investigated CO_2 capture in an absorber utilizing hot potassium carbonate otherwise known as Benfield solution as a solvent. The volumetric mass transfer coefficient of CO_2 capture with ionic liquid in an RPB absorber was measured by Zhang *et al*. (2011). Similarly, Luo *et al*. (2012) proposed an empirical correlation for the interfacial area based on a study conducted in an RPB absorber using different types of wire mesh packings.

The RPB absorber rigs in Table 2.2 are either counter-current flow RPB absorbers or cross-flow RPB absorbers. Tan and Chen, (2006) investigated CO_2 capture in a counter-current flow RPB absorber. In a later study, Cheng and Tan, (2011) used the same RPB absorber to examine CO_2 absorption from indoor air. Also, Yu *et al*. (2012) used 30 wt% MEA and a blend of MEA, PZ and Diethylenetriamine (DETA) to obtain the height of the transfer unit (HTU) and the overall mass transfer coefficient. It was found that the HTU was less than 1 cm and the overall mass transfer coefficient was more than 5.8 (1/s). The cross-flow RPB absorber was employed for CO_2 capture in the study of Lin *et al*. (2010) and Lin and Chen, (2011). This cross-flow RPB absorber has a higher velocity and lower resistance to gas flow. Rahimi and Mosleh (2015) examined the effect of MEA concentrations, rotor speed, gas and liquid flow rates on the HTU in an RPB absorber packed with expamet and wired mesh packings. It was found that the HTU ranges from 0.024 m to 0.04m and depended on the MEA concentrations, rotor speed, gas flow rate and liquid flow rate.

Table 2.3 Summary of RPB absorbers used in solvent-based PCC worldwide

Institutions	Dimensions			Packing			Rotor speed	CO_2 conc.	Reference
	ID (m)	OD (m)	Height (m)	Type	Surface area (m^2/m^3)	Porosity ε	rpm	vol%	
Newcastle University, UK[a]	0.156	0.398	0.025	Expamet	2132	0.76	600-1000	3.4-4.7	Jassim *et al.* (2007)
	0.08	0.30	0.02	Expamet	663	0.80	600-1450	12-15	Lee *et al.* (2017)
Beijing University of Chemical Technology, China	0.156	0.336	0.05	Wire mesh	-	-	0-1440	10.0	Luo *et al.* (2012)
	0.08	0.20	0.031	Wire mesh	870	0.95	900-1300	4.1	Yi *et al.* (2009)
	0.02	0.06	0.02	Wire mesh	850	0.90	1130-3164	10.0	Zhang *et al.* (2011)
National Tsing Hua University, Taiwan	0.076	0.16	0.02	Wire mesh	803	0.96	600-1200	10.0	Yu *et al.* (2012)
	0.048	0.088	0.03	Wire mesh	897	0.95	300-1800	10.0	Lin and Chen (2011)
Yasouj University, Iran	0.06	0.12	0.04	Expamet	1300	0.9	400-1600	0.5	Rahimi and Mosleh (2015)

[a]The data used in chapter 6 to validate the RPB model develop in chapter 5 of this thesis were collected using this RPB rig.

2.4.2 Commercial deployment of RPB

RPB has been used at a commercial scale to remove H_2S from refinery gases at the Fujian Petroleum refinery Co, China (Qian *et al*. 2012). The process used MDEA solvent. It has also been used commercially since the 1990s in the deaeration of water and the production of hypochlorous acid. So far, there is no commercial application of the RPB in the solvent-based PCC process.

2.4.3 Modelling and simulation studies of the RPB absorber for solvent-based PCC process using MEA

The RPB technology has been increasingly used for CO_2 capture and many model-based studies have been published on its application in solvent-based PCC process (Borhani et al., 2019; Cheng et al., 2013; Im et al., 2020; Joel et al., 2017, 2014; Liu et al., 2020; Luo et al., 2021; Oko et al., 2018; Yi et al., 2009). There are two distinct differences between modelling and simulation of RPB and PB. The first difference is that of mass transfer which occurs only along the packing in PB and along the packing and the distance between the rotor and its casing in RPB. The second difference is that the absorption in PB takes place in a straight bed and is gravity driven thus the mass transfer coefficients of the gas and liquid phases do not vary as the flows of the liquid and gas does not vary in the bed. In contrast, the absorption in RPB takes place under centrifugal acceleration in a tapered bed with varied cross-sectional area, thus the gas and liquid velocities change in the radial direction resulting in changes in the mass transfer coefficients of the gas and liquid phases (Cortes Garcia et al., 2017).

The modelling and simulation of CO_2 absorption in RPB absorber have been demonstrated for solvents like NaOH (Munjal et al., 1989), Benfield solution (Yi et al., 2009), MDEA (Zhang et al., 2014), and MEA (Borhani et al., 2018; Im et al., 2020; Joel et al., 2015, 2014; Luo et al., 2021; Oko et al., 2018). Munjal et al., (1989) studied the influence of the rotor speed on the interfacial area and mass transfer coefficients for CO_2 capture with an aqueous solution NaOH. It was found that both increased with rotor speed. Yi et al. (2009) developed a model for an RPB absorber in MATLAB® using Benfield solution as solvent. This steady-state model assumed a spheral droplets liquid flow and accounted for both kinetic and CO2 mass balance in the droplets. The model correctly predicted the mole composition of CO_2 in the exit gas at different rotor speeds, gas flow rates and liquid flow rates.

Furthermore, the model was used to investigate the influence of liquid and gas flow rates and rotor speed on the overall mass transfer coefficient. An RPB absorber model was developed in FORTRAN® by Zhang et al., (2014) based on penetration theory for CO_2 absorption with MDEA. It was assumed in the model that mass transfer occurs in the whole packing surface. The model accurately predicted the experimental data with a maximum deviation of 10% as the rotor speed was increased from 400 to 1100 rpm. Additionally, the model was utilized to investigate the rate of CO_2 decarburization. It also accurately predicted the CO_2 decarburization rates at different rotor speeds, MDEA concentrations, gas flow rates and temperatures.

Modelling and simulation studies of MEA-based PCC process using RPB absorber are summarized in Table 2.4. This table provides information on the simulation tools used to develop the models, the model complexity as related to mass transfer and reaction kinetics, the source of data used for model validation and a description of the process analysis carried out with the model.

Table 2.4 Summary of literature review on modelling and simulation of CO_2 with MEA solvent in RPB absorber

Reference	Tool	Model complexity	Model type & validation	Model applications/process analysis
Joel et al. (2014)	Aspen Plus® plus Fortran®	Rate-based model, mass transfer and chemical equilibrium, reaction kinetics	Steady-state model, model validation was done using data collected by Jassim et al. (2007)	• Investigated the effect of rotor speed, MEA concentration and lean solvent temperature on capture level.
Kang et al. (2014)	gPROMS model builder® and Aspen Properties®	Rate-based model, mass transfer, chemical equilibrium and enhancement factor	Steady-state model, model validated with experimental data by Jassim et al. (2007) and Yu et al. (2012).	• Investigated the effects of various mass transfer and liquid holdups correlations on model predictions of CO_2 mole fraction, K_Ga and CO_2 removal.
Joel et al. (2015)	Aspen Plus® and Fortran	Rate-based model, mass transfer and chemical equilibrium, reaction kinetics	Steady-state model, model validated with experimental data collected by Jassim et al. (2007).	• Investigate the model predictions performance against experimental data based on 2 sets of mass transfer correlations. • Studied the effects of RPB size, lean solvent flowrates and higher lean MEA temperature CO_2 capture level.
Thiels et al. (2016)	Aspen Custom Modeller®	Rate-based model, mass transfer and chemical equilibrium, the enhancement factor	Steady-state model, model validated with experimental data collected by the authors	• Process design for the RPB absorber to achieve CO_2 capture levels of 80%, 90%, 95% and 99%. • Proposed the arrangement of RPB and PB in series to minimize packing volume.
Borhani et al. (2018)	gPROMS model builder® and Aspen Properties®	Rate-based model, mass transfer and chemical equilibrium, the enhancement factor	Steady-state model, model validated with experimental data collected by Jassim et al.(2007).	• Examined the influence of reaction kinetics and enhancement factors on CO_2 capture level. • Evaluated the influence of rotor speed, lean MEA concentrations, flow rates and temperatures on capture level

Oko et al. (2018)	gPROMS model builder® and Aspen Properties®	Rate-based model, mass transfer and chemical equilibrium, the enhancement factor	Steady-state model, model validated with experimental data collected by Jassim et al. (2007)	• Evaluated the impacts of temperature rise on the liquid phase speciation, equilibrium partial pressure and mass transfer resistance. • Investigated various design options for the RPB absorber intercooler.
Oko et al. (2019)	gPROMS model builder® and Aspen Properties®	Rate-based model, mass transfer and chemical equilibrium, the enhancement factor	Steady-state model, model validated with experimental data collected by Jassim et al. (2007).	• Tested and compared the predicting capability of various correlations of liquid and gas film mass transfers correlations and interfacial area correlations. • New data were derived for the gas-film mass transfer coefficient.
Im et al.(2020)	gPROMS model builder® and Aspen Properties®	Rate-based model, mass transfer and chemical equilibrium, the enhancement factor	Steady-state model, model validated with experimental data collected by Jassim et al. (2007) and Cheng et al. (2013)	• Steady-state process optimization to minimize the total energy consumption of the RPB-based CO_2 capture process with MEA
This study	Aspen Custom modeller® and Aspen Properties®	Rate-based model, mass and heat transfers, chemical equilibrium, Enhancement factor	Steady-state model, model validated with experimental data collected by Jassim et al. (2007)	• Detailed scale-up and large-scale process analysis • Evaluated the influence of rotor speed, lean MEA concentrations, flow rates and on capture level • Technical and economic analysis

2.5 Summary

The literature review of the solvent-based PCC process in PB and RPB carried out in this chapter has shown that:

- In spite of the few commercial deployments, the PCC process has major drawbacks including high capital and operating costs and high energy consumption for regeneration of solvent and operation of the PCC plant. In addition to these, the absence of incentives and adverse policies from the government are parts of the challenges of the solvent-based PCC process.
- There are many pilot plants of the solvent-based PCC process using PB globally and experimental data collected from these pilot plants are very useful for model validation. There are two major approaches used to model the PCC process. These are the rate-based modelling approach and the equilibrium-based approach. The rate-based approach provides a more realistic representation of the PCC process and is therefore deemed more accurate than the equilibrium-based modelling approach. The modelling and simulation of the PCC process using MEA have been carried out at pilot scale and at large-scale. Model validation with pilot plant data is necessary to verify the accuracy and reliability of the model.
- The large-scale studies are often based on validated models scaled up to large-scale PCC plants. The scale-up of the PCC process in PB is based on the GPDC chart and assumed pressure drop. However, the pressure drops curves in the range applicable to PB design is limited. Due to this, a scale-up method that eliminates this limitation of the GPDC method when determining the diameter of the absorber and stripper is needed.
- The PZ solvent has many superior properties compared to MEA and has been proposed as an alternative to the 30 wt% MEA solvent for the PCC process. There are many pilot-scale studies of CO_2 capture in PB using PZ solvent. Pilot plant testings indicated that the energy consumption of the solvent-based PCC process can be reduced with PZ solvent. Experimental data useful for model validation are also available in the literature. The modelling and simulation of the individual components (absorber only and stripper only) of the solvent-based PCC process in PB using PZ have been carried out by many researchers at the pilot scale. The modelling and simulation of the whole PCC process using PZ solvent have not been demonstrated at pilot and large-scale.

Furthermore, the energy and economic assessment of the large-scale PCC process using PZ in comparison to the benchmark MEA solvent has not been performed.

- The RPB has the potential to significantly reduce the size of the absorber and stripper in the PCC process. The size reduction benefits of the RPB has been demonstrated via several experimental studies. There are many RPB absorber rigs worldwide. Many experimental and model-based studies on CO_2 capture in RPB absorbers using MEA solvent also exist. However, all these studies were performed using tiny RPB absorber rigs. There is no study on the scale-up of the RPB absorber for the solvent-based PCC process. Furthermore, the technical and economic assessment of the large-scale RPB absorber for large-scale RPB absorber has not been reported.

Chapter 3: Modelling, simulation and scale-up of solvent-based PCC process using monoethanolamine in packed columns

3.1 Overview

This chapter describes the modelling and simulation of the solvent-based PCC process using MEA in PB. The model was implemented in Aspen Plus® V8.4. It also proposes a new method for the scale-up of the process. There are extensive experimental and model-based studies on the PCC process using MEA. Due to the lack of data for the large-scale PCC process, the validated pilot scale model of the process is scaled to large-scale. Such models could be used for technical and economic performance studies, optimisation and sensitivity analysis of the large-scale PCC process. A new scale-up method is proposed in this study. It calculates the diameter of the packed columns based on the flooding gas velocity. The flooding point establishes the upper boundary of operation in PB in terms of hydrodynamic capacity. Therefore, the velocity of the gas at flooding conditions is particularly important and is an important design parameter for the PB. This is worthwhile as this method does not require users to assume the column pressure drop as is the case in other studies in the literature. It also eliminates the difficulty of interpolating between data in the GPDC method.

Section 3.2 discusses model development of the solvent-based PCC in Aspen Plus®. Section 3.3 focused on model validation of the solvent-based PCC process at the pilot scale. A new scale-up method is proposed in Section 3.4, and detailed validation of the proposed scale-up method is the focus of Section 3.5. Large-scale PCC process simulation and analysis are presented in Section 3.6. The chapter conclusions are drawn in Section 3.7.

3.2 Model development for the PCC process

The rate-based model of the CO_2 absorption and desorption was developed in Aspen Plus® V8.4 using the Radfrac block model. The Radfrac block allows the absorber and the stripper to be set up using either the equilibrium stage approach or the rate-based approach. The equilibrium stage approach assumes that well-mixed vapour and liquid phases exist at equilibrium on each theoretical stage. However, in reality, this is not so, thereby making the equilibrium approach an approximate method (Zhang et al., 2009).

The rate-based method on the other hand assumes equilibrium only at the vapour-liquid interface and considers reaction kinetics and film reaction in the calculation of the rate of mass transfer between the phases. In other words, separation is achieved by the mass transfer of components (CO_2) from the bulk vapour phase to the bulk liquid phase (MEA). The rate-based approach is used for this study because it has been reported to give more reliable and accurate predictions for CO_2 absorption with MEA compared to the equilibrium stage approach (Lawal et al., 2009). The details of the various aspects of the closed-loop model of the CO_2 capture process are described in the flowing subsections. The assumptions used in the model includes;

- Steady-state model
- No accumulation in the bulk gas as well as the liquid and gas films
- The vapour phase consists of CO_2, H_2O, N_2 and MEA.
- One-dimensional differential mass and energy balances for both the liquid phase and the gas phase.
- Gas and liquid flow counter-currently.
- All reactions are assumed to occur in the liquid phase
- The liquid phase consists of ionic species namely OH^-, H_3O^+, HCO_3^-, CO_3^{2-}, $MEAH^+$, and $MEACOO^-$ in addition to the four original components CO_2, H_2O, N_2 and MEA.
- Rate-controlled reactions are considered in the mass transfer between the liquid and the vapour phases.

3.2.1 Thermodynamic and kinetic models

The absorption of CO_2 with MEA creates a solution containing electrolytes. These electrolytes must be accounted for when developing models of the solvent-based PCC process in Aspen Plus®. The Electrolyte Non-Random-Two-Liquid (ElecNRTL) activity coefficient model developed by Chen and Evans (1986) was used to account for the electrolytes in the solution and to calculate the properties of the liquid phase. The SRK equation of state was used to calculate the properties of the vapour phase (Soave, 1972). In addition to this, available correlations within the ElecNRTL model were utilized to calculate other important thermodynamic properties namely, vapour pressure, Henry's constant, heat of absorption and vapour pressure.

The liquid film is characterised by various equilibrium reactions which are described by the following equations (Aspentech, 2008):

$$2H_2O \leftrightarrow H_3O^+ + OH^- \quad 3.1$$

$$CO_2 + 2H_2O \leftrightarrow H_3O^+ + HCO_3^- \quad 3.2$$

$$HCO_3^- + H_2O \leftrightarrow H_3O^+ + CO_3^{2-} \quad 3.3$$

$$MEACOO^- + H_2O \leftrightarrow MEA + HCO_3^- \quad 3.4$$

$$MEAH^+ + H_2O \leftrightarrow MEA + H_3O^+ \quad 3.5$$

The temperature-dependent equilibrium constants (K_{eq}) for reactions 3.1 to 3.5 are determined from the expression in Eq. 3.6.

$$K_{eq} = Exp^{\left(A+\frac{B}{T}+C\ In\ T+DT\right)} \quad 3.6$$

The values of the constants A, B, C and D in Eq. 3.6 on mole fraction basis for reactions 3.1-3.5 are shown in Table 3.1.

Table 3.1: Constants for calculating K_{eq} (Edwards et al., 1975; Posey and Rochelle, 1997)

Reactions	A	B	C	D
Eq 3.1	132.899	-13445.9	-22.4773	0.0
Eq 3.2	231.465	-12092.1	-36.7816	0.0
Eq 3.3	216.049	-12431.7	-35.4819	0.0
Eq 3.4	0.79960	-8094.81	0.0	-0.007484
Eq 3.5	1.282562	-3456.170	0.0	0.0

The various rate-controlled reactions used in the model are presented in Eqs. 3.7-3.10. Eqs. 3.7 and 3.8 are the forward and reverse reactions for bicarbonate formation while Eqs. 3.9 and 3.10 are the forward and reverse reactions for carbamate formation (Zhang and Chen, 2013).

$$CO_2 + OH^- \rightarrow HCO_3^- \quad 3.7$$

$$HCO_3^- \rightarrow CO_2 + OH^- \quad 3.8$$

$$MEA + CO_2 + H_2O \rightarrow MEACOO^- + H_3O^+ \quad 3.9$$

$$MEACOO^- + H_3O^+ \rightarrow CO_2 + H_2O + MEA \quad 3.10$$

The rate of reaction (R_{rxn}) for the reaction (j) expressed in Eqs. 3.7 – 3.10 are estimated by the power law. The expression describing the power law is presented in Eq. 3.11.

$$R_{rxn,j} = k_j^o \exp\left[-\frac{E_j}{R}\left(\frac{1}{T} - \frac{1}{298.15}\right)\right]\prod_{i=1}^{N} C_i^{\alpha_{ij}} \quad 3.11$$

Where k_j^o and E_j are the pre-exponential factor and the activation energy of the reactions in Eqs. 3.7-3.10. Their values are presented in Table 3.2. R is the universal gas constant.

Table 3.2 Pre-exponential factor and activation energy for the rate-controlled reactions (Aspentech, 2008; Pinsent et al., 1956)

Reactions	k^o_j (kmol/m^3 s)	E_j (kJ/kmol)
Eqn 3.7	4.32 x 10^{13}	55430
Eqn 3.8	2.38 x 10^{17}	123220
Eqn 3.9	9.77 x 10^{10}	41240
Eqn 3.10	2.18 x 10^{19}	59190

3.2.2 Transport properties models

The Radfrac model in Aspen Plus® requires the values of transport properties such as the density, viscosity, thermal conductivity, surface tension, and diffusivity to be determined for the liquid and gas phases. The transport properties are essential as they are part of the correlations used to calculate the mass transfer, heat transfer and liquid holdup in the Radfrac model. The transport properties are calculated using models within the ElecNRTL property method. These models used are presented in Table 3.3.

Table 3.3 Transport properties models (Aspentech, 2001).

	density	Viscosity	Thermal conductivity	Surface tension	Diffusivity
Liquid phase	Clark density model	Jones-Dole model	Riedel model	Onsager-samaras model	Wilke-Chang model
Gas-phase	COSTALD model by Hankinson and Thomson	Chapman-Enskog-Brokaw model	Wassiljewa-Mason-Sexena model	Nil	Chapman-Enskog-Wilke-Lee model

3.2.3 Heat and mass transfer correlations

The heat and mass transfers in the absorber and the stripper of the PCC process are accounted for using the correlations listed in Table 3.4. This includes the liquid film mass transfer coefficient, gas film mass transfer coefficient, liquid holdup, interfacial area and heat transfer coefficient.

Table 3.4 Mass and heat transfers correlations

	Liquid film mass transfer coefficient	gas film mass transfer coefficient	Effective Interfacial area	Liquid holdup	Heat transfer coefficient
Absorber	Onda et al. (1968)	Onda et al. (1968)	Onda et al. (1968)	Stichlmair et al. (1989)	Chilton and Colburn (1934)
Stripper	Bravo et al. (1985)	Bravo et al. (1985)	Bravo et al. (1985)	Bravo et al. (1992)	Chilton and Colburn (1934)

3.3 Model validation at pilot-scale

The performance of the rate-based model described in Section 3.2 is validated using experimental data from two pilot plants. The two pilot plants are (1) Separation Research Programme (SRP) pilot plant operated by the University of Texas at Austin, USA (2) Brindisi pilot plant located in Brindisi, Italy. Detailed descriptions of the two pilot plants are presented in the following sub-sections.

3.3.1 The SRP pilot plant data

The SRP pilot plant is a multifunctional PCC test facility operated by the research group led by Prof. Gary Rochelle at the University of Texas at Austin. The pilot plant is operated with synthetic flue gas consisting of air and CO2 gas. The absorber and the stripper have a diameter of 0.427 m and two packing beds of height 3.05 m each. There is a plate collector and a distributor between the beds. The absorber and the stripper have a total height of 11.1 m. It can capture up to 250 kg_{CO_2}/h. The experimental data collected by Dugas (2006) in the SRP pilot plant are used to validate the rate-based model. The absorber was packed with IMTP 40 and the stripper was packed with Flexipac 1Y. The flue gas flow rate was varied between 5.49-13.75 m^3/min, likewise, the solvent flow rate was varied between 0.0132-0.1041 m^3/min. Up to 99% capture levels were achieved in some of the experiments.

Out of the 48 experimental cases reported by Dugas (2006), three cases representing different liquid to gas ratios and CO_2 concentrations were chosen for the model validation. Detailed of the three selected cases are shown in Table 3.5.

Table 3.5 SRP Pilot plant experimental cases used for model validation (Dugas, 2006)

		Cases		
		28	32	47
Flue gas	Flow rates (m^3/min)	11.00	5.48	8.22
	Concentration (mol%)	16.54	17.66	18.41
	Temperature (°C)	47.98	46.56	59.23
	Pressure (bar)	1.05	1.05	1.03
Lean solvent	Flow rate (m^3/min)	0.08	0.04	0.03
	Temperature (°C)	40.00	40.56	40.07
	Lean loading (mol_{CO2}/mol_{MEA})	0.29	0.28	0.28
Rich solvent	Flow rate (m^3/min)	0.083	0.04	0.03
	Temperature (°C)	50.83	51.95	45.57
Absorber	Pressure (bar)	1.00	1.00	1.00
Stripper	Pressure (bar)	1.62	1.62	0.68
	Feed Temperature (°C)	72.31	85.52	81.18
	Reboiler duty (kW)	365.75	152.39	204.86

The model predictions of the CO_2 capture level, CO_2 loading and the temperature profiles in the absorber and the stripper were compared to the experimental data for the three cases considered. The CO_2 capture level is determined using the expression in Eq. 3.12.

$$CO_2 \text{ capture level } (\%) = \left(\frac{y_1 - y_2}{y_2}\right) \times 100 \qquad 3.12$$

Where y_1 mole fraction of CO_2 in the inlet gas and y_2 is the mole fraction of CO_2 in the outlet gas. The CO_2 loading in the lean and rich MEA solvent is calculated with Eq. 3.13

$$CO_2 \text{ Loading} = \frac{[CO_2] + [HCO_3^-] + [CO_3^{2-}] + [MEACOO^-]}{[MEA] + [MEA^+] + [MEACOO^-]} \qquad 3.13$$

The results of the model predictions against experimental data are shown in Table 3.6 for the CO_2 capture levels and CO_2 loadings. In each case, the model predictions agree with

the experimental data. The percentage relative errors (PRE) between the experimental data and the model predictions are estimated with Eq. 3.14.

$$PRE = \left(\frac{i_{exp} - i_{prediction}}{i_{exp}} \right) \times 100 \qquad 3.14$$

Where i_{exp} is the experimental data measured in the pilot plant and $i_{prediction}$ is the value predicted by the rate-based model.

Table 3.6 Model predictions versus experimental data from the SRP pilot plant

		Cases		
		28	32	47
Lean loading (mol_{CO_2}/mol_{MEA})	Exp	0.28	0.27	0.28
	Model	0.28	0.27	0.30
	PRE (%)	0.00	0.00	6.60
Rich loading (mol_{CO_2}/mol_{MEA})	Exp	0.41	0.43	0.53
	Model	0.41	0.43	0.48
	PRE	0.00	0.00	9.43
CO_2 capture level (%)	Exp	86.0	95.0	69
	Model	85.0	90.0	69
	PRE	1.16	5.26	0.00

The temperature profiles of the liquid phase along the height of the absorber and the stripper predicted by the model are plotted against the ones measured in the pilot plant for the three cases in Figures 3.1-3.6. The model predictions generally followed the experimental trend indicating a good agreement. However, the model slightly over-predicted the temperatures in the absorber and the stripper. These are particularly prominent in the middle (height of 2.2 to 5.5 m) of the absorber and the stripper. These mismatches in temperature profiles are due to the over-prediction of the heat of CO_2 absorption by the Gibbs-Helmholtz equation used in the ElecNRTL model. Since the rise in temperature of the liquid and vapour phases in the absorber and the stripper is based on the heat of absorption, this over-prediction of the heat of absorption affects the final results for the temperature. This is the reason for the mismatch between the experimental data and model predictions of the temperature profiles. The model also predicted

correctly the location of the temperature bulge in both the absorber for all the cases. The location and size of the temperature bulge depend on the L/G ratio (Plaza and Rochelle, 2011). Dugas (2006) reported that at L/G ratios below 5 (kg/kg) the temperature bulge was located at top of the absorber. At above this (5kg/kg) L/G ratio, the temperature bulge was located at the bottom of the absorber. Findings in this study agree with this. The temperature bulge is located close to the bottom of the absorber (Figures 3.2 and 3.3) when the L/G ratio is 6.6 kg/kg and close to the top of the absorber (Figure 3.5) when the L/G ratio is 3.4 kg/kg.

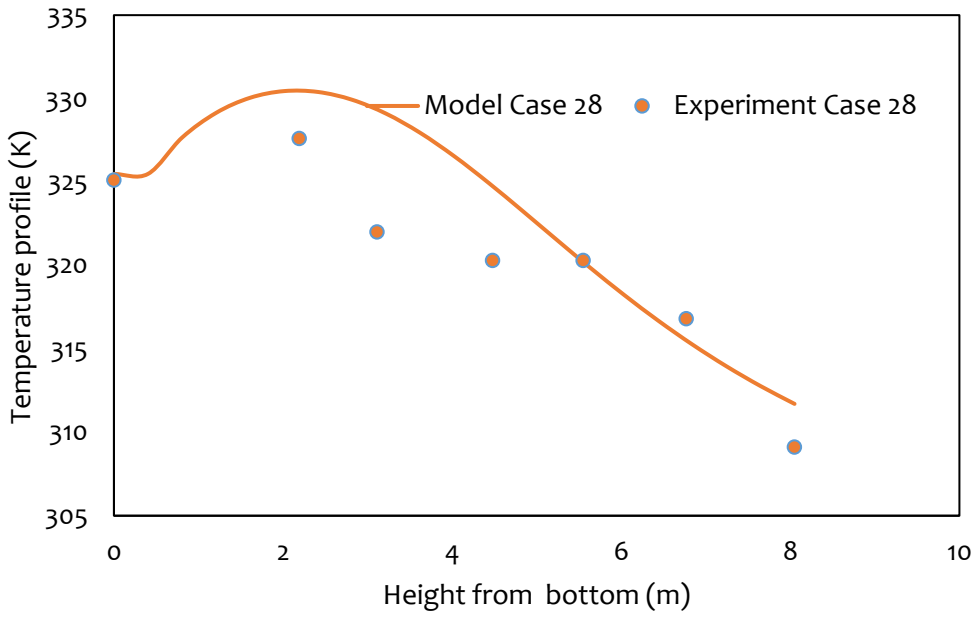

Figure 3.1 Experimental data versus model predictions for temperature profiles in the absorber for Case 28

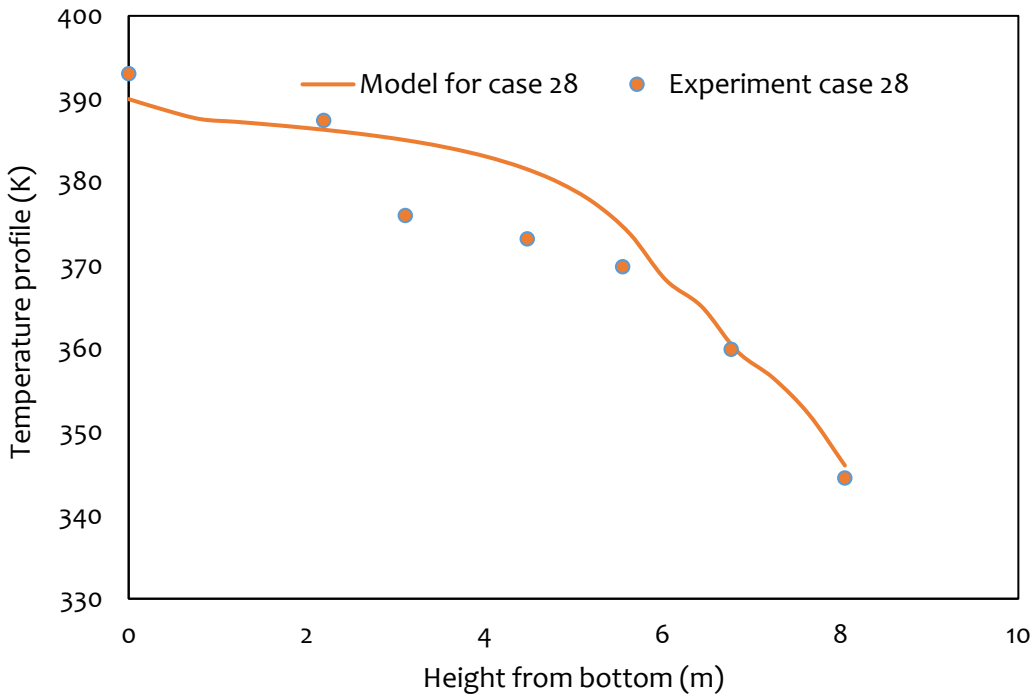

Figure 3.2 Experimental data versus model predictions for temperature profiles in the stripper for Case 28

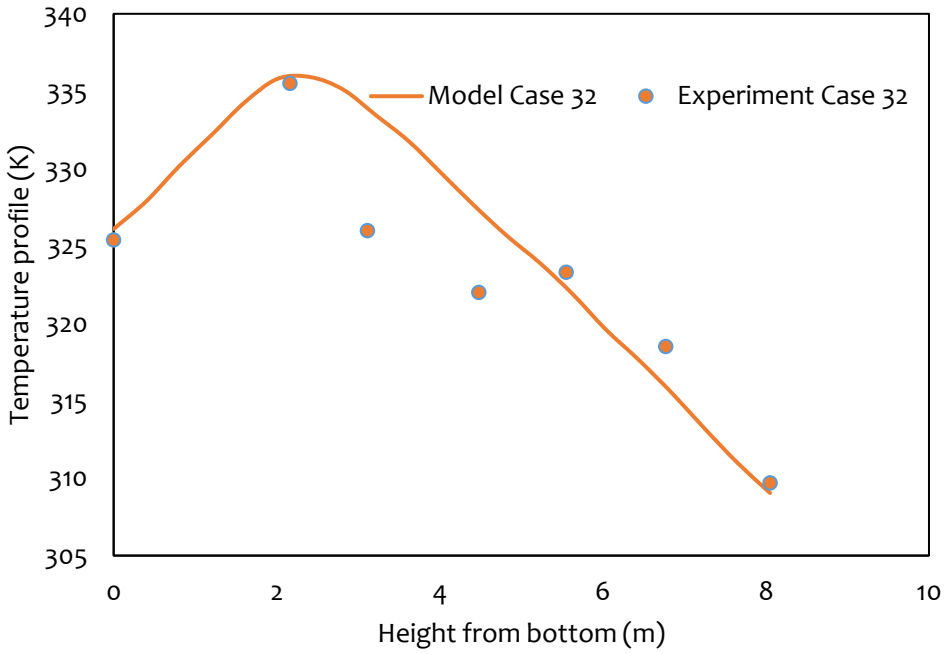

Figure 3.3 Experimental data versus model predictions for temperature profiles in the absorber for Case 32

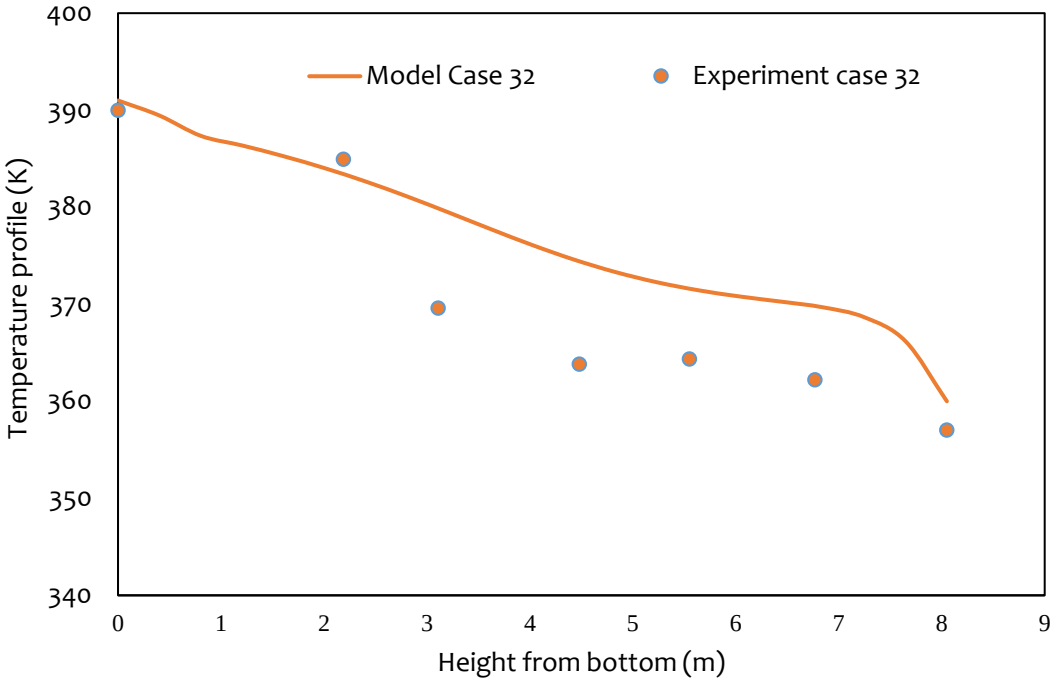

Figure 3.4 Experimental data versus model predictions for temperature profiles in the stripper for Case 32

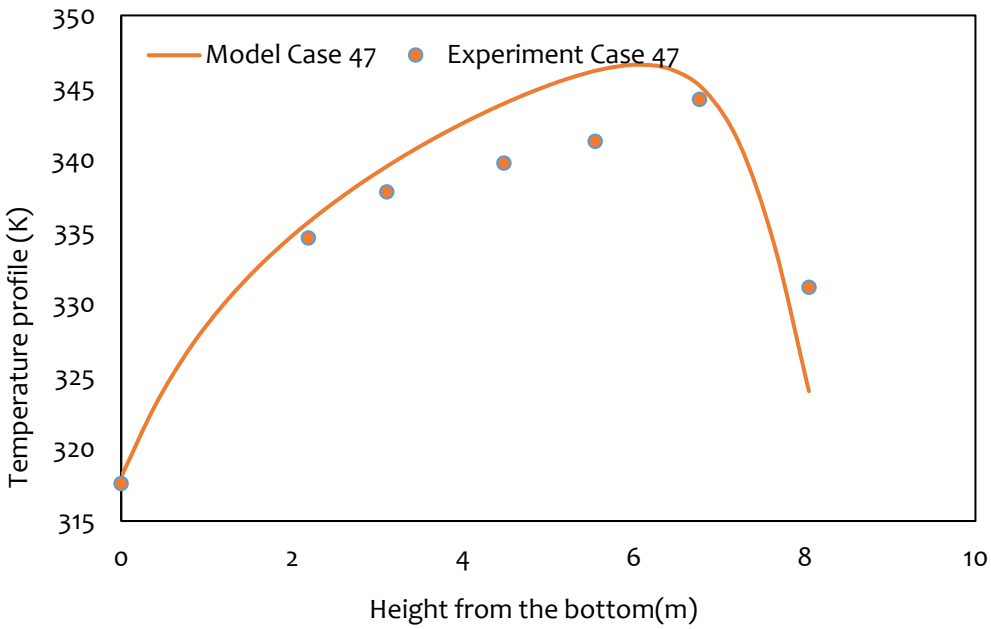

Figure 3.5 Experimental data versus model predictions for temperature profiles in the absorber for Case 47

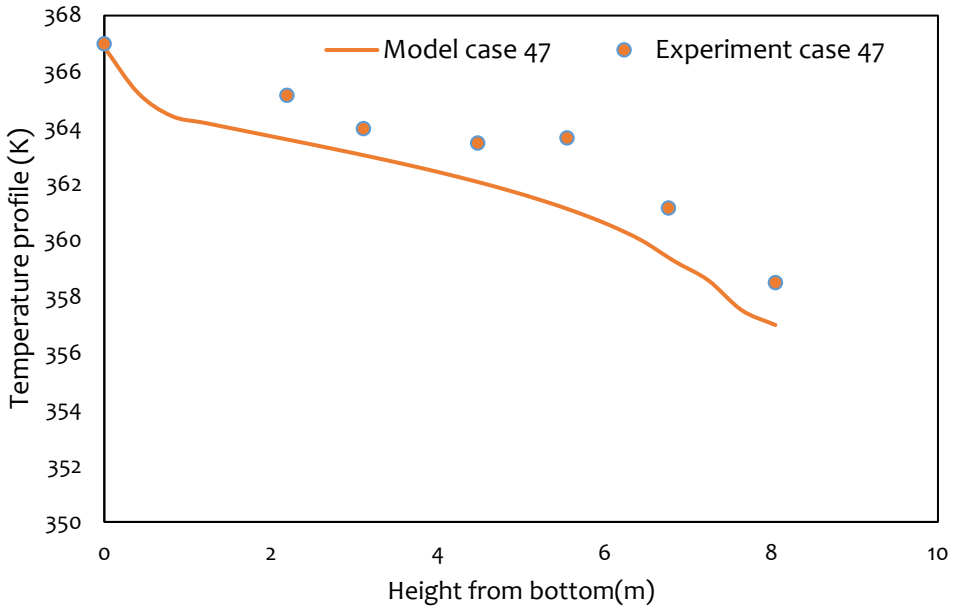

Figure 3.6 Experimental data versus model predictions for temperature profiles in the stripper for Case 47

3.3.2 Brindisi pilot plant data

The PCC rate-based model was further validated using experimental data collected at the Brindisi pilot plant located in Brindisi Italy (Enaasen, 2015). This is a much bigger pilot plant compared to the SRP pilot plant. It is operated with a split stream of flue gas from one of the four units in a coal-fired power plant. The absorber has a diameter of 1.5 m, a packing height of 22 m and is packed with Mellapak 250X. The stripper has a diameter of 1.3 m, a packing height of 11 m and is packed with IMTP 50. It can process up to 9212 m^3/h of flue gas and can capture 60 t_{CO_2}/day. This represents about 0.45 % of the total flue gas produced from one of the four units of the power plant (Lemaire et al., 2014). The lean solvent flow rate in the pilot plant experiments was varied between 20-80 m^3/h. The main process conditions used as inputs to the model are shown in Table 3.7.

Table 3.7 Brindisi Pilot plant experimental cases used for model validation (Enaasen, 2015)

		Cases				
		2	3	4	5	7
Flue gas	Flow rate (Nm^3/s)	2.743	2.758	2.748	2.764	2.756
	CO_2 conc. (mol%)	11.0	12.5	12.0	10.4	11.0
	temperature (^oC)	46.2	44.8	45.6	44.7	46.9
Lean solvent	Flow rate ($m^3/$)	0.0083	0.0083	0.0083	0.0097	0.0097
	Temperature (^oC)	46.9	47.0	47.0	47.0	47.1
	MEA conc. (wt%)	29.6	29.8	29.8	29.8	29.7
Absorber Pressure (bar)	1.00	Stripper pressure (bar)			1.84	

The five experimental cases shown in Table 3.7 were used to validate the model. These five cases achieved the least relative deviations in CO_2 mass balance out of the 12 experimental cases reported in the experimental campaign. In addition to the original packings used in the absorber and the stripper during the pilot-plant campaign, the model was also validated using the same set of packings (IMTP 40 and Flexipac 1Y) used in the SRP pilot plants. The reason for this is to be able to use the model to validate the scale-up method proposed later in Section 3.4 of this thesis.

The comparison of the results of model predictions against experimental data for rich solvent CO_2 loading, desorbed CO_2 and reboiler duty in the pilot plant using the two sets of packing are presented in Tables 3.8-3.10.

Table 3.8 Results of model predictions against experimental data for rich loading in the Brindisi pilot plant

	Rich CO_2 loading (mol_{CO2}/mol_{MEA})				
		(Mellapak 250X and IMTP 50)		(IMTP 40 and Flexipac 1Y)	
Cases	Experiment	Model	PRE (%)	Model	PRE (%)
2	0.50	0.504	0.80	0.501	0.20
3	0.480	0.485	1.04	0.479	0.21
4	0.490	0.489	0.20	0.485	1.02
5	0.430	0.430	0.00	0.428	0.47
7	0.450	0.453	0.67	0.446	0.89

Table 3.9 Results of model predictions against experimental data for desorbed CO_2 in the Brindisi pilot plant

	Desorbed CO_2 (kg/hr)				
		(Mellapak 250X and IMTP 50)		(IMTP 40 and Flexipac 1Y)	
Cases	Experiment	Model	PRE (%)	Model	PRE (%)
2	1815	1812	0.16	1810	0.28
3	1654	1657	0.18	1652	0.12
4	1712	1712	0.00	1708	0.23
5	1772	1775	0.17	1770	0.11
7	1838	1837	0.05	1833	0.27

Table 3.10 Results of model predictions against experimental data for reboiler duty in the Brindisi pilot plant

		Reboiler duty (MJ/kg_{CO_2})			
		(Mellapak 250X and IMTP 50)		(IMTP 40 and Flexipac 1Y)	
Cases	Experiment	Model	PRE (%)	Model	PRE (%)
2	3.46	3.42	1.16	3.48	0.60
3	3.36	3.37	0.30	3.35	0.30
4	3.20	3.19	0.31	3.22	0.63
5	3.62	3.66	1.11	3.63	0.28
7	4.01	3.95	1.50	4.02	0.25

For all the cases considered, the model predictions agree with the experimental data. The results also demonstrated that the packings (IMTP 40 and Flexipac 1Y) used in the SRP pilot plant give identical results and show identical performance in terms of rich loading, desorbed CO_2 and reboiler duty. This is because despite having different nominal sizes, the IMTP 40 and IMTP 50 packings have the same void fraction (0.98). Also, the surface area of the Mellapak 250X and Flexipac 1Y packings are similar (Suess and Spiegel, 1992). The PREs between the model predictions and the experimental measurements are generally less than 2% for the cases considered. This further indicates the accuracy of the rate-based model.

3.4 A newly proposed method for scale-up of absorber and stripper

The generalized pressure drop correlation (GPDC) chart (Figure 3.7) is mostly used in the scale-up of the solvent-based PCC process. Several researchers have used it to design and investigate the requirements of a large-scale solvent-based PCC process (Agbonghae et al., 2014; Canepa et al., 2013; Dutta et al., 2017; Luo and Wang, 2017; Montañés et al., 2017; Nittaya et al., 2014). In these studies, pressure drops of either 21 or 42 mm-water per meter of packing were adopted when scaling the validated pilot-scale model of the PCC plant to a large-scale PCC plant. This is because they are the only two pressure drops at which correlation curves are available within the range of (15-50 mm-water per meter of packing)

recommended for the design of PB by Sinnott, (2005). In addition to this, interpolation of data on the GPDC chart is difficult and could lead to errors. The sizes of the absorbers and strippers obtained from some scale-up studies that used the GPDC method are shown in Table 3.11.

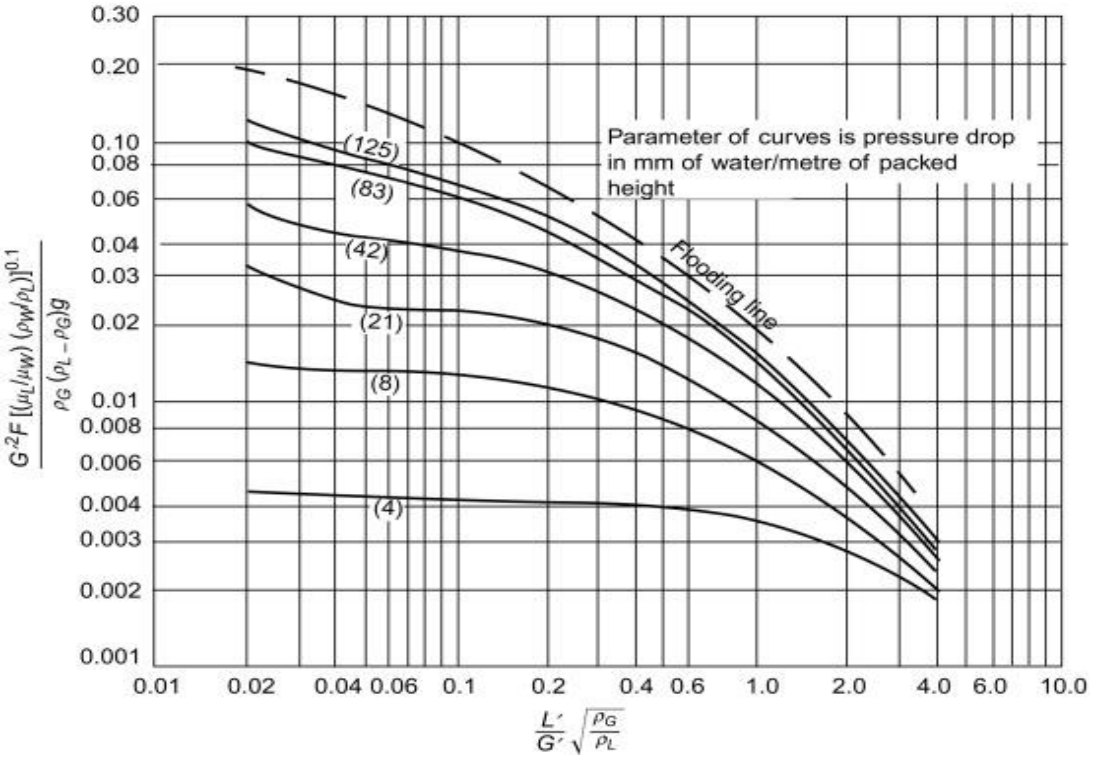

Figure 3.7 GPDC chart (Sinnott, 2005)

Table 3.11 Absorber and stripper size in large-scale PCC plant based on GPDC method

Power plant	Absorber		Stripper		Reference
	No	Dimensions	No	Dimensions	
250 MW_e CCGT	2	9.5	1	8.2	Canepa et al., (2013)
400 MW_e NGCC	2	11.93 m x 19.06m	1	6.76 m x 28.15 m	Agbonghae *et al.* (2014)
600 MW_e NGCC	2	15.8m x 27.2 m	1	10.4 m x 20 m	Dutta *et al.* (2017)
613 MW_e NGCC	2	16.3 m x 23.2 m	1	9.7 m x 23.2 m	Montañés *et al.* (2017)
500 MW_e Coal-fired	2	9.0 m x 17 m	1	9.0 m x 17 m	Lawal *et al.* (2012)
750 MW_e coal-fired	3	11.8 m x 34 m	2	10.4 m x 16 m	Nittaya *et al.* (2014)

In order to design the PBs (absorber and stripper), the diameter is an important key parameter that must be determined. PBs are designed to operate away from flooding. This is because flooding is capable of reducing the efficiency of the column and could lead to the breakdown of the column (Liu et al., 2019). Since the upper limit of hydrodynamic capacity in the columns is established by the flooding point, the flooding gas velocity is particularly important and is an essential design parameter for PBs (Brunazzi et al., 2008). The first correlation for predicting the flooding points was developed by Sherwood et al. (1938). It was developed using random packings in an air-water system. The experimental data collected were correlated into a curve on the GPDC chart. This ordinate of this chart was later modified by Lobo et al. (1945) to include the ratio of the specific surface area and the porosity (a/ε^3). This ratio characterised the packing shape and size. Later, Leva (1954) added several isobaric curves to the chart and determined that the ratio a/ε^3 introduced by Lobo et al. (1945) did not predict the packing hydraulic performance accurately. They proposed and used the packing factor to describe the packing size and shape. Eckert (1970) calculated the packing factor and further modified chart. This version by Eckert is known as the Sherwood-Leva-Eckert (SLE) GPDC chart (Figure 3.7). It has been used to predict the pressure drop and flooding points in PB with random packings for many years.

In later versions of the chart developed for random and structured packings, the flooding curve was omitted (Kister et al., 2007; Strigle, 1994; Wolf-Zöllner et al., 2019). An expression for the flooding curve in PB was written in equation form to show the relationship between the abscissa and the ordinate as follows (Kister and Gill, 1992, 1991; Piché et al., 2001).

$$\mathrm{CP} = \mathrm{A}\log^2(\mathrm{F_{LV}}) + \mathrm{B}\log(\mathrm{F_{LV}}) + \mathrm{C} \qquad 3.15$$

Where F_{LV} represents the flow parameter and is the ratio of the kinetic energy of the liquid entering the PB to that of the gas (Kister et al., 2007). It is described by Eq. 3.16.

$$\mathrm{F_{LV}} = \frac{\mathrm{L}}{\mathrm{G}}\sqrt{\frac{\rho_\mathrm{L}}{\rho_\mathrm{G}}} \qquad 3.16$$

Where F_{LV} is the flow parameter, L is the liquid mass flow rate and G is the gas mass flow rate. F_{LV} is low for vacuum operations but high for gas absorption operations due to their high liquid to vapour loadings. CP in Eq.3.15 is the capacity parameter. It is given by:

$$\mathrm{CP} = \sqrt{\mathrm{U}_{\mathrm{G,fl}}^2 \left(\frac{\rho_{\mathrm{G}}}{\rho_{\mathrm{L}} - \rho_{\mathrm{G}}}\right) v^{0.1} \mathrm{F_P}} \qquad 3.17$$

Where $\mathrm{U_{G.fl}}$ is the flooding velocity, ρ_{G} is the gas phase density, ρ_{L} is the liquid phase density and v is the kinematic viscosity. The pressure drops ($\Delta \mathrm{P_{fl}}$) at incipient flooding in PB has been correlated as a function of the packing factor (F_p) (Geankoplis, 2014; Kister and Gill, 1992, 1991) as follows;

$$\Delta \mathrm{P_{fl}} = 0.115 \mathrm{F_P^{0.7}} \qquad 3.18$$

Eq. 3.18 is useful when dealing with packings with F_P in the range 32-195 m^{-1}, Hence, it can predict pressure drop at flooding in PB from 14 to 51 mm-water/ m. The equation provides optimistic predictions of the pressure drop at flooding for F_p above 195 m^{-1}. Therefore, care must be taken when used for packings with F_p above this value (Geankoplis, 2014).

The parameters A, B and C in Eq. 3.15 are determined with expressions in Eqs. 3.19-3.21 from Piché et al. (2001).

$$\mathrm{A} = 0.07 \ln(\Delta \mathrm{P_{fl}}) - 0.11 \qquad 3.19$$

$$\mathrm{B} = -0.25 \ln(\Delta \mathrm{P_{fl}}) - 0.89 \qquad 3.20$$

$$\mathrm{C} = 0.12 \ln(\Delta \mathrm{P_{fl}}) + 0.71 \qquad 3.21$$

Eq. 3.15 can also be expressed as;

$$\mathrm{CP} = \mathrm{A}(\log \mathrm{F_{LV}})^2 + \mathrm{B} \log(\mathrm{F_{LV}}) + \mathrm{C} \qquad 3.22$$

Equating Eq. 3.17 to Eq. 3.22 and substituting Eq. 3.16 for F_{LV} in the obtained equation. An expression of the form in Eq 3.23 is obtained for the flooding velocity.

$$U_{G,fl} = 0.3048\left[\left(\frac{\rho_G}{\rho_L-\rho_G}\right)^{-0.5} v^{-0.05}\, F_P^{-0.5}\left\{A\left(\log\left(\frac{L}{G}\sqrt{\frac{\rho_G}{\rho_L}}\right)\right)^2 + B\left(\log\left(\frac{L}{G}\sqrt{\frac{\rho_G}{\rho_L}}\right)\right) + C\right\}\right] \quad (3.23)$$

The value of $U_{G,fl}$ in PB can be determined Eq 3.23 so long the packing factor, as well as the flow rate, density and kinematic viscosity of the liquid and gas phases, are known. The density and viscosity of the phases can be obtained from literature, experiment or software like Aspen Plus®, gPROMS and ProMax®.

The diameter required to handle the gas and liquid flow in PB is based on the maximum operating capacity (MOC) determined by the maximum pressure drop allowed. The MOC ranges from 60 to 85%, hence, PB is designed to operate at 60 to 80% of the flooding velocity (Marx-Schubach and Schmitz, 2019). In this study, the PB is assumed to operate at 70% flooding velocity. The operating superficial velocity is therefore determined as shown in Eq 3.24.

$$U_G = 0.7U_{G.fl} \quad 3.24$$

The diameter (D) of the PB needed at 70% flooding velocity is determined by Eq 3.35.

$$D = \sqrt{\frac{4G}{\pi U_G \rho_G}} \quad 3.25$$

Therefore, depending on the value of the F_P, different pressure drop values can be determined in the range recommended for the design of PB. And the diameter of the PB can be determined. This eliminates the limitations inherent in the GPDC chart.

3.5 Validation of the proposed scale-up method

The scale-up method proposed in Section 3.4 was validated by applying it to scale up between two existing PCC pilot plant sizes. That is from a small pilot plant (SRP pilot plant) to a bigger pilot plant (Brindisi pilot plant). The Brindisi pilot plant has about 22 times the capacity of the SRP pilot plant. Since the pilot plant have been operated in real life, using the proposed method to correctly estimate the diameter of the absorber and the stripper will demonstrate its reliability and guarantee accuracy when applied to carry out scale-up

from pilot-scale to large-scale. Therefore, in this section, the SRP pilot plant with a flue gas flow rate of 0.15 kg/s is scaled to the size of the Brindisi pilot plant with a flue gas flow rate of 3.22 kg/s. This step validates the proposed scale-up method. The method is later used in Section 3.6 to scale to a large-scale PCC plant that can treat a flue gas flow rate of 356 kg/s from a 250 MW_e CCGT power plant. The steps involved in the proposed method validation are provided in the following:

3.5.1 Calculation of lean solvent flow rate

The lean solvent flow rate required to capture 90% of the CO_2 from the flue gas entering the Brindisi pilot plant is calculated using an absorption capacity of 0.2 mol_{CO2}/mol_{MEA}, MEA concentration of 30 wt%, CO_2 mass fraction of 0.1608 and flue gas mass flow rate of 3.22 kg/s. This estimation is based on a constant flow rate for the gas and the solvent in the absorber. The required solvent flow rate is calculated based on the approach described by Agbonghae et al. (2014). The number of equivalents/moles of amine is 1 for MEA, therefore, the value of z in Eq 3.26 is 1.

$$L_{Lean} = \frac{Gx_{CO_2}\varphi_{CO_2}}{100\check{z}(\alpha_{Rich} - \alpha_{Lean})}\left[\frac{M_{MEA}}{44.009}\left(1 + \frac{1 - \omega_{MEA}}{\omega_{MEA}}\right) + z\alpha_{Lean}\right] \qquad 3.26$$

The solvent flow for the stripper is the sum of the rich solvent mass flow rate and the reflux rate. The gas in the stripper is the boil-up rate needed to keep the lean CO_2 loading at0.23 mol_{CO2}/mol_{MEA}. Following these calculations, the absorber solvent rate was determined to be 10.88 kg/s while the stripper solvent rate was determined to be 11.5 kg/s. The vapour phase in the stripper was calculated to be 1.62 kg/s. This vapour phase is calculated from the boil-up rate based on the steam in the reboiler.

3.5.1 Calculation of columns diameter

The diameters of absorber and stripper are calculated with Eqs. 3.23-3.25 described in Section 3.4. The density and viscosity of the liquid (MEA solvent) were obtained from the model of the SRP pilot plant. The absorber has the IMTP 40 packing (F_P=79 m^{-1} or 24 ft^{-1}) while the stripper has the Flexipac 1Y packing (F_P = 168.3 m^{-1} or 51.3 ft^{-1}). Using the data provided in Table 3.12 and the flue gas (3.22 kg/s) and solvent flow rate rates estimated

above (Section 3.5.1) the superficial gas velocity in the absorber was determined to be 1.83 m/s while that of the stripper was determined to be 1.2 m/s.

Table 3.12 Data used to calculate the superficial gas velocity in the absorber and stripper

	Parameters				
	ρ_L (kg/m^3)	ρ_G (kg/m^3)	A	B	C
Absorber	1017.10	1.030	-0.11	-0.91	0.72
Stripper	1019.90	1.020	-0.07	-0.89	0.79

The diameters of the absorber and stripper were obtained based on the superficial gas velocity using Eq 3.25 as 1.46 and 1.28 m. These values are very close to the value of the absorber diameter (1.5m) and stripper diameter (1.3m) in the Brindisi pilot plant. Also, the % deviations between the real diameters of the columns in the Brindisi pilot plant and the diameters estimated by the proposed scale-up method are just 2.6 and 1.54 % respectively. The ability of the proposed method to correctly predict the diameter of the PB (absorber and the stripper) in a real-life (existing) pilot-scale PCC plant validates it and shows that it can be used reliably to calculate the diameter of PB in the CO_2 capture process.

3.6 Calculation of packing height

In addition to the diameter of the PB, the packing height also needs to be determined. Therefore, in addition to the method to calculate the diameter of the PB proposed and validated in previous sections (Sections 3.4 and 3.5). The procedures for estimating the packing heigh required in a PB are also provided. This is the main focus of this section. The packing height required for a particular level of separation is expressed in terms of the gas flow rate, gas composition and the overall gas mass transfer coefficient as shown in Eq 3.27 (Seader et al., 2006).

$$Z = \frac{F_{g\_a}}{K_{tot}P}\int_{y_1}^{y_2}\frac{dy}{y - y_e} \qquad 3.27$$

F_{g_a} is the gas molar flow rate per cross-sectional area, y_1 is the mole fraction of CO_2 in the inlet gas, y_2 is the mole fraction of CO_2 in the outlet gas, y is the mole fraction of CO_2 in the gas phase at any point in the column and y_e is the Gas-phase mole fraction of CO_2 in equilibrium with CO_2 concentration in the liquid. K_{tot} is the overall gas-phase mass transfer coefficient and P is the pressure.

Eq. 3.27 can also be written as

$$Z = H_{OG}.NTU \tag{3.28}$$

Where H_{OG} is the height of a transfer unit and NTU is the number of the transfer unit. It is given as:

$$NTU = \int_{y_1}^{y_2} \frac{dy}{y - y_e} = In\left(\frac{y_2}{y_1}\right) \tag{3.29}$$

It is assumed that y_e is negligible in Eq 3.29 due to the fast reaction between CO_2 and MEA CO_2 (Aroonwilas and Veawab, 2004; Fu et al., 2014; Khan et al., 2011). The packing height of the PB, therefore, depends on how big the NTU is.

H_{OG} demonstrates the packing efficiency, therefore a smaller value of H_{OG} demonstrates the efficiency of the packing used in the PB for the separation process (Coulson and Richardson, 2002). It can be calculated from the expression in Eq 3.30.

$$H_{OG} = \frac{F_{g\_a}}{K_G a P} \tag{3.30}$$

In experiments carried out at the SRP pilot plant, Dugas (2006) reported the values of K_Ga for the IMTP 40 packing. Since the flue gas conditions, solvent conditions, and packing material used in those experiments are the same as those used in this study, the K_Ga values reported in Dugas (2006) were utilized to calculate the value of the H_{OG} for the absorber. The parameter used to determine the height of the absorber and their values are given in Table 3.13. The height of packing in the absorber was calculated as 22.6 m.

Table 3.13 Parameters to calculate the absorber packing height and their values

Parameters	Unit	Values
NTU	-	4.10
K_Ga	kmol/m^3 s. bar	0.0122
F_{g_a}	(kmol/s m^2)	0.06
P	(bar)	1.00
H_{OG}	(m)	5.50

The height of packing in the stripper was calculated using a different approach. This is because the values of K_{Ga} were not reported in Dugas (2006) for the Flexipac 1Y packing used in the stripper. This was due to the negative CO_2 driving force at the top of the stripper. The packing height in the stripper was estimated using Eq 3.31 described in detail by Agbonghae et al. (2014). It is the summation of the height equivalent to a theoretical plate (HETPs) of the stages in the stripper.

$$Z_{,Stripper} = \sum_{i=2}^{N-1} HETP_i \qquad 3.31$$

Where N is the total number of stages. This approach was implemented in Aspen Plus® with the calculator block function. The calculator block determines the end-stage in the packed section by fixing the starting stage at a particular value. The start stage was fixed at 2. This is because stage 1 in the stripper is treated as the condenser. In addition to this, the design specification functionality in Aspen Plus® was used to maintain the lean CO_2 loading at 0.23 mol_{CO2}/mol_{MEA}. Starting from N=5, the value was increased (by 1) until there was a negligible change in the reboiler duty. The packing height in the stripper was estimated as 11.40 m. Table 3.14 shows the comparison of the pilot plant dimensions to the ones obtained from using the method described in this study.

Table 3.14 Comparison of the pilot plant dimensions to the proposed scale-up method results

	Pilot plant dimensions		Proposed Scale-up method	
	Abs.	Stripp.	Abs.	Stripp.
D (m)	1.50	1.30	1.46	1.28
Z (m)	22.0	11.0	22.60	11.40

3.7 Scale-up to large-scale solvent-based PCC plant

Since the proposed scale-up method has been validated by using it to scale up between two existing pilot plant sizes. It is then used to develop a large-scale PCC process to treat flue gas from a 250 MW_e CCGT power plant. The input conditions into the large-scale PCC are shown in Table 3.15. These input conditions are the same as those used to design the large-scale PCC plant reported in Canepa et al. (2013). This is to enable scale-up results from

this study to be compared to those obtained by Canepa et al. (2013) using the GPDC method.

Table 3.15 Inlet conditions for the large-scale of the PCC plant (Canepa et al., 2013)

Input parameters		Value
Flue gas	Capture level	90 %
	Flow rate (kg/s)	356
	Temperature (°C)	40.0
	Compositions (wt%)	CO2: 7.60
		H_2O: 4.70
		N2: 86.2
		Ar: 1.50
Lean solvent	Temperature (°C)	40.0
	MEA (wt%)	30.0
Absorber	Pressure (bar)	1.01
	Packing	IMTP 40
Stripper	pressure (bar)	1.62
	Packing	Flexipac 1Y

Using Eq. 3.26 and the information in Table 3.15, the initial lean solvent flow rate required in the absorber of the large-scale PCC process was calculated to be 669 kg/s. The L/G term of 1.88 was used in Eq 3.23 together with the density and viscosity of the phases obtained from the validated pilot-plant model to calculate the flooding velocity in the absorber as 3.25 m/s. The absorber operating superficial velocity was obtained as 2.27 m/s. Likewise, an L/G term of 10.05 was used in Eq 3.23 together with the density and viscosity of the phases obtained from the validated pilot-plant model to calculate the flooding velocity in the stripper as 1.83 m/s. The operating superficial velocity in the stripper was obtained as 1.28 m/s. The larger value of the L/G term for the stripper is why the diameter of the stripper is usually smaller than that of the absorber.

Based on these values, the diameter of the absorber for the large-scale PCC process was estimated with Eq 3.25 as 13.86 m. That of the stripper was estimated to be 7.50 m. Figure 3.8 shows the relationship between the diameter and the number of absorbers and

strippers needed by the large-scale PCC plant. This was based on a maximum column diameter of 18 m and what can be delivered by the state-of-the-art PCC technology (IEA-GHG, 2006; Reddy et al., 2013, 2008; Scherffius et al., 2013). Furthermore, an absorber with a diameter similar to this has been designed and constructed by Fluor, also stripper with a diameter similar to this has been built for SO_2 stripping (Dutta et al., 2017; Reddy et al., 2008).

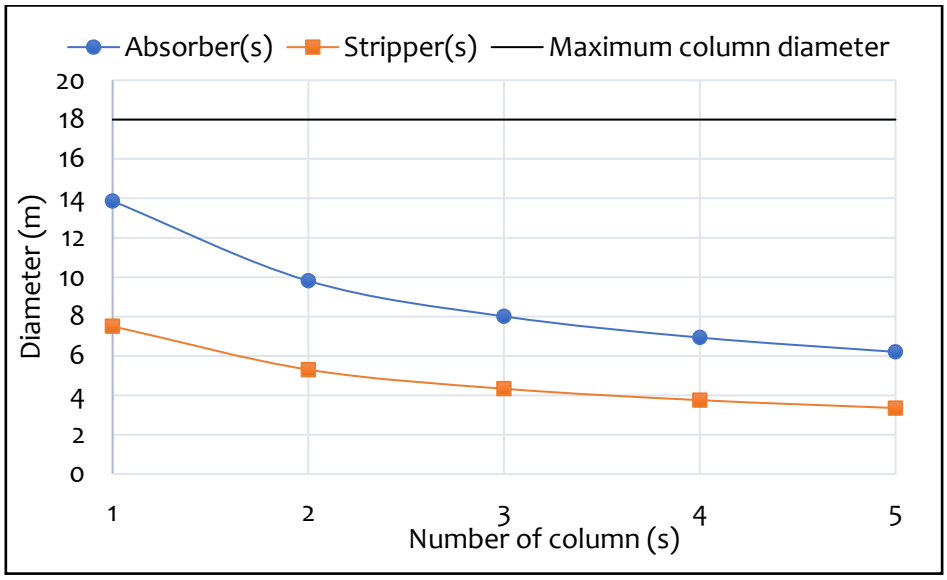

Figure 3.8 Diameter and number of columns relationship

Since the diameter estimated for the absorber and stripper is less than 18 m. One absorber and one stripper column were chosen for the large-scale PCC plant. This also reduces the footprint and the complexity of the process. A packing height of 28.5 m was used for both the absorber and the stripper.

3.7.1 Large-scale PCC plant simulation

The flowsheet of the large-scale PCC process simulated using Aspen Plus® V8.4 is shown in Figure 3.9.

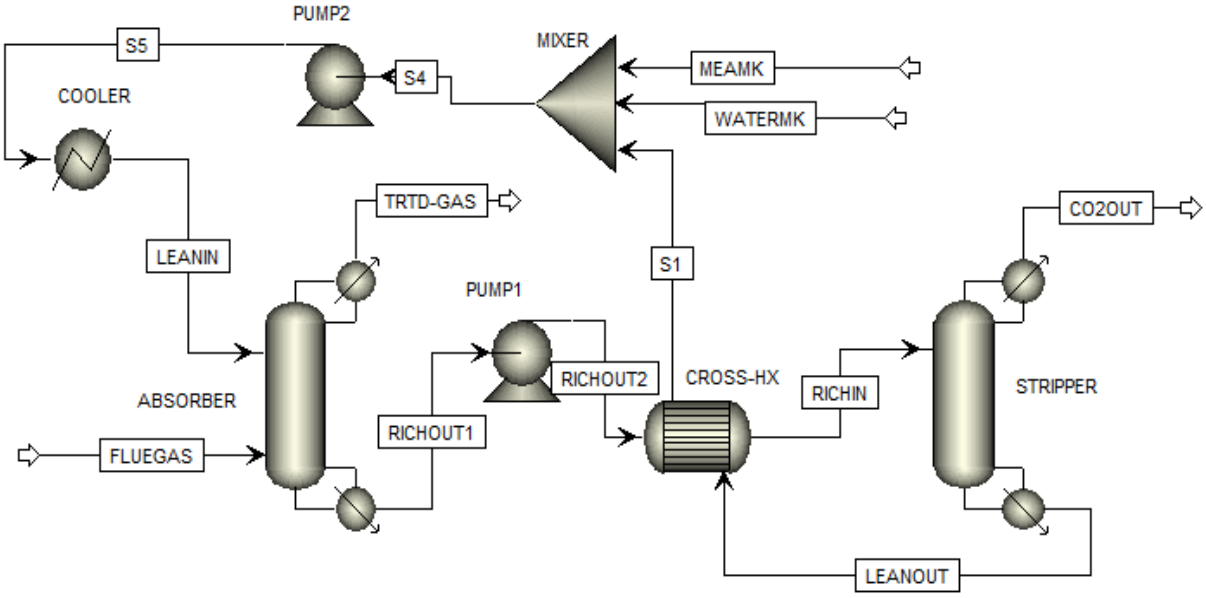

Figure 3.9 Process flowsheet of the solvent-based PCC process

The results obtained from the large-scale simulation are compared to those obtained by Canepa et al. (2013) in Table 3.16. The diameter of the absorber and stripper developed using the scale-up method proposed in this study are less than those developed using the GPDC method by Canepa et al. (2013). In this study, a single absorber of diameter 13.8 m will be needed by the large-scale PCC process as opposed to the two absorbers of 9.5 m diameters in Canepa et al. Also, a stripper of 7.5 m will be needed for the large-scale PCC process as opposed to 8.2 m reported in Canepa et al. (2013). The higher diameters for absorber and stripper obtained by Canepa et al. (2013) may be as a result of a pressure drop of 42 mm-water/ m assumed to design the absorber and the stripper. This could be higher than the actual pressure drops in the columns.

The large-scale PCC developed in this study achieved a pressure drop of 24.6 mm-water/m in the absorber and 5.81 mm-water/m in the stripper. The pressure drop in the stripper is smaller due to the structured packing used and the lower vapour flow rate compared to the absorber. The lower pressure drops in this study indicate that less power would be required for pumping compared to Canepa et al. (2013).

Table 3.16 Comparison of results from the large-scale PCC process in this study to Canepa et al. (2013)

		Canepa et al. (2013)	This study
Lean solvent	Flow rate (kg/s)	720.5	705
	L/G ratio (kg/kg)	2.02	1.98
CO_2 loading	Lean (mol_{CO2}/mol_{MEA})	0.30	0.30
	Rich (mol_{CO2}/mol_{MEA})	0.45	0.47
Capture level	(%)	90.0	90.0
Flooding ratio		N/a	0.7
Absorber	Numbers	2[a]	1
	Packing type	IMTP40	IMTP40
	Diameter (m)	9.5	13.86
	Packing height (m)	30.0	28.5
	Pressure drop (mm-water/m)	42	24.5
Stripper	Number	1.0	1.0
	Diameter (m)	8.2	7.5
	Packing height (m)	30.0	28.5
	Pressure drop (mm-water/m)	42.0	5.8
Reboiler	Temperature (°C)	117.0	115.7
	Duty (MW)	121.0	115.3
	Specific duty ($GJ/tonCO_2$)	4.97	4.69
Condenser	Temperature (°C)	25.0	25.0

[a]With one absorber the diameter is 14.1 m

The packing heights for the absorber and the stripper in this study are also lower compared to Canepa et al. (2013). This could lead to a reduction in the capital cost of the PCC process. The solvent flow rate and the specific reboiler duty of the large-scale PCC developed in this study are also 2.12 % and 5.63 % less. The lower solvent flow rate is due to more CO_2 uptakes in this study as shown by a higher rich CO_2 loading. This lower solvent flow rate also leads to lower regeneration energy consumption. This would also reduce pumping energy and ultimately the operating cost of the process.

3.8 Conclusion

In this chapter, a steady-state model of the solvent-based PCC process using MEA was developed in Aspen Plus®. The model was validated at a pilot scale using experimental data from the SRP pilot plant and Brindisi pilot plant respectively. The model results showed a very good agreement with the experimental data. Furthermore, a new scale-up method based on the superficial gas flooding velocity was proposed. The proposed method was validated by applying it to scale up between real pilot plant sizes. The method accurately predicted the diameters of the absorber and stripper in the pilot plant. This method was then used to develop a large-scale PCC process with capacity for flue gas from a 250 MW_e CCGT power plant. The following are the key findings from this chapter:

- The PCC model predicted the pilot plants performance with maximum deviations of 9.43% using the SRP pilot plant data and 1.50% using the Brindisi pilot plant data. The model also correctly predicted the temperature profiles in the absorber and stripper of the SRP pilot plant depicting the locations of the temperature bulges in all the cases considered.
- The proposed scale-up method was able to correctly predict the absorber and stripper diameters with differences of just 2.6 and 1.54 % thereby demonstrating the reliability of the scale-up method.
- The design of the large-scale PCC process using the proposed scale-up method and the simulation in Aspen Plus® showed that diameters estimated using the GPDC method are slightly bigger. Also, solvent flow rate and regeneration energy consumptions were 2.12 % and 5.63% more for the GPDC method. Therefore, the costs of the solvent-based PCC could be lower based on estimates of the column dimensions, solvent flow rate and reboiler duty obtained from this study.

Chapter 4: Simulation, technical and economic performance assessment of large-scale PCC process using piperazine in a packed column

4.1 Overview

This chapter describes the simulation of the solvent-based PCC process using PZ in PB. This includes model development, model validation, model scale-up and technical and economic assessment of the large-scale PCC process using PZ. This study was carried out using Aspen Plus® V8.4. In addition to the standard configuration of the PCC process using 40 wt% PZ, the energy consumption and cost of the process using other process configurations (absorber intercooling (AI) and absorber intercooling plus advanced flash stripper AFS (AIAFS)) different concentrations of PZ (30 wt% and 35 wt%) were also investigated. The energy consumptions and costs of the PCC processes using PZ are compared to a PCC process using 30 wt% MEA.

Section 4.2 presents the descriptions of the various process configurations. Section 4.3 describes model development of the solvent-based PCC using PZ in Aspen Plus®. Model validation at the pilot scale is the focus of Section 4.4. A brief description of the model scale-up is given in Section 4.5. Section 4.6 discusses the simulation of the large-scale PCC process using PZ in Aspen Plus®. The technical and economic assessments are presented in Section 4.7. The chapter conclusions are drawn in Section 4.8.

4.2 Description of different process configurations

4.2.1 Standard solvent-based PCC process using PZ

The process flowsheet depicting the standard configuration of the PCC process is presented in Figure 4.1. It includes the absorber, the stripper, a cooler, a cross-heat exchanger and pumps. A compression unit has also been included in the flowsheet. Other process configurations are normally compared to this configuration.

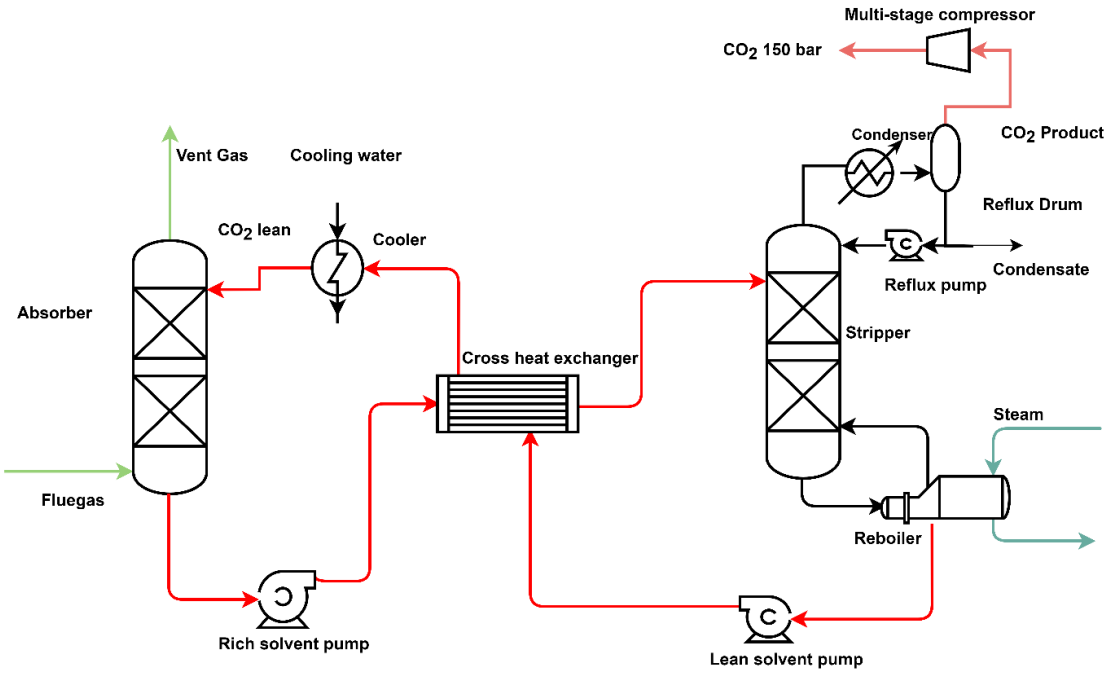

Figure 4.1 Standard configuration of the solvent-based PCC process using PZ as a solvent

4.2.2 Absorber intercooling

A variation of the standard PCC process with an intercooler in the absorber is presented in Figure 4.2. During CO_2 absorption, the temperature of the solvent gradually increases. This reduces the absorption capacity of the solvent. Absorbers are often fitted with Intercoolers to cool and reduce the temperature of the solvent. This lowers the equilibrium CO_2 partial pressure and enhances the mass transfer and cyclic capacity of the solvent. This could lead to a reduction in packing height and regeneration energy consumption.

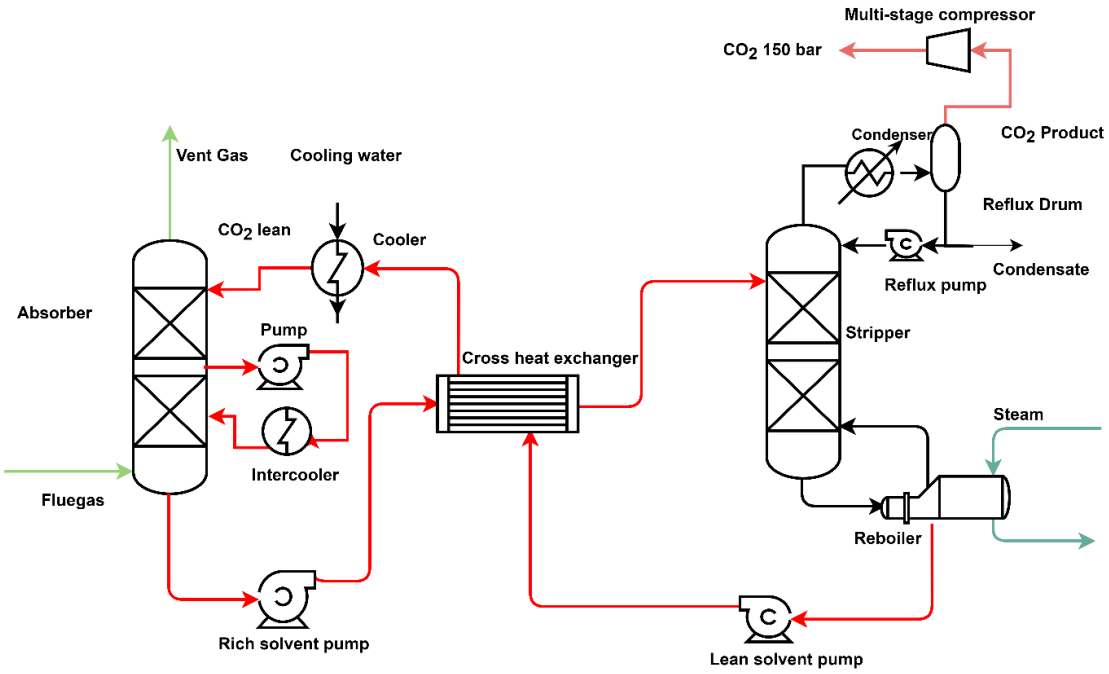

Figure 4.2 Absorber intercooling configuration of the solvent-based PCC process using PZ as a solvent

4.2.3 Absorber intercooling with advanced flash stripper

The AIAFS was proposed and tested at a pilot scale by researchers from the University of Texas at Austin (Gao et al., 2019; Gao and Rochelle, 2020; Lin et al., 2016). In contrast to the standard configuration of the PCC process, there are two cross-heat exchangers in the AIAFS namely the cold rich exchanger and the warm rich exchanger. They are used to raise the temperature of the rich solvent from the stripper. It includes the splitting of the rich solvent into a cold rich bypass (CRB) and a warm rich bypass (WRB) before and after the cold-cross exchanger. An additional cold rich exchanger that raises the temperature of the cold rich bypass using the hot vapour from the stripper is also included. The CRB and WRB are mixed before entering the top of the stripper. Compared to the feed stream in a standard striper configuration, the temperature of the mixed (CRB and WRB) bypasses are lower. This enhances energy performance by recovering latent heat and condensing water vapour. The remaining stream from the hot-cross exchanger enters the steam heater where it is heated further and then enters the flash tank located at the bottom of the stripper. The flash tank and the steam heater correspond to the reboiler in the standard stripper configuration. The flowsheet of the AIAFS is presented in Figure 4.3.

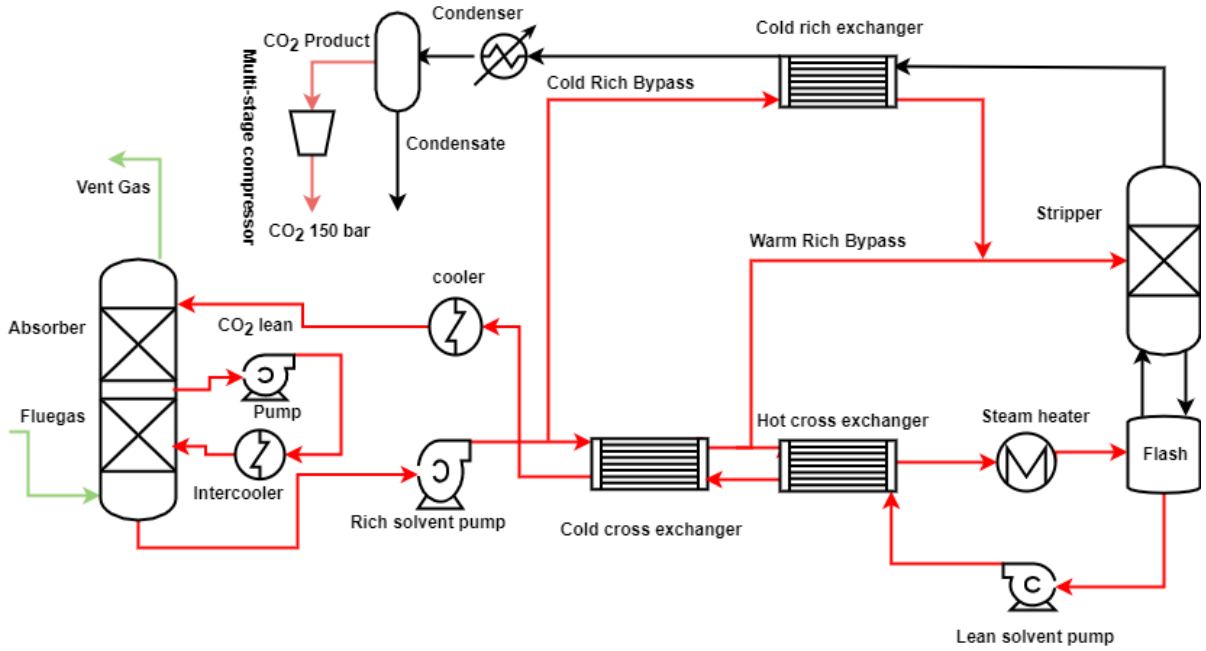

Figure 4.3 The absorber intercooling plus advanced flash stripper configuration of the solvent-based PCC process using PZ

4.3 Model development for PCC process using PZ

The rate-based model of the solvent-based PCC process using PZ was developed in Aspen Plus® V8.4. This model includes the electrolyte (component speciation) chemistry, correlations for calculating mass and heat transfers, and correlations for determining the hydrodynamic properties of the column. In addition to this, correlations for determining the physical properties, thermodynamic properties, and kinetic properties are also included in the model. The assumptions used in the model includes

- Steady-state model
- No accumulation in the bulk gas as well as the liquid and gas films
- The vapour phase consists of CO_2, H_2O, N_2 and PZ.
- One-dimensional differential mass and energy balances for both the liquid phase and the gas phase.
- Gas and liquid flow counter-currently.
- All reactions are assumed to occur in the liquid phase
- The liquid phase consists of ionic species namely OH^-, H_3O^+, HCO_3^-, CO_3^{2-}, PZH^+, $PZCOO^-$, H^+PZCOO^- and $PZ(COO^-)_2$ in addition to CO_2, H_2O, N_2 and PZ.

- Rate-controlled reactions are considered in the mass transfer between the liquid and the vapour phases.

4.3.1 Thermodynamic and kinetic models

Aspen Plus consists of various physical properties methods that are used to develop the model of a chemical process. For a process that involves the formation of electrolytes such as CO2 absorption with amines, the electrolytes non-random two liquids (ElecNRTL) physical property method is the most widely used. It consists of an electrolyte thermodynamic model (ElecNRTL) and an equation of state (Redlich-Kwong (RK)) model. The ELECNRTL thermodynamic model was used to calculate the various properties of the liquid phase while the RK equation of state was used to calculate the various properties of the vapour phase. Eqs 4.1-4.7 are the equilibrium reactions describing the absorption of CO2 with PZ (Ermatchkov et al., 2006). The equilibrium constants (K_{eq}) of these reactions are calculated from the expression in Eq 4.8.

$$2H_2O \rightleftarrows H_3O^+ + OH^- \quad 4.1$$

$$CO_2 + 2H_2O \rightleftarrows HCO_3^- + H_3O^+ \quad 4.2$$

$$H_2O + HCO_3^- \rightleftarrows CO_3^{2-} + H_3O^+ \quad 4.3$$

$$PZH^+ + H_2O \rightleftarrows PZ + H_3O^+ \quad 4.4$$

$$PZ + HCO_3^- \rightleftarrows PZCOO^- + H_2O \quad 4.5$$

$$H^+PZCOO^- + H_2O \rightleftarrows PZCOO^- + H_3O^+ \quad 4.6$$

$$PZCOO^- + HCO_3^- \rightleftarrows PZ(COO^-)_2 + H_2O \quad 4.7$$

$$\ln K_{eq} = A + \frac{B}{T} + C \ln T + DT \quad 4.8$$

The coefficients A, B, C and D for calculating the equilibrium constants in each reaction (Eqs 4.1-4.7) are given in Table 4.1.

Table 4.1 Coefficients of equilibrium constant (K_{eq})

Reactions	A	B	C	D	References
Eq 4.1	132.899	-13446	-22.4773	0	Posey and Rochelle, (1997)
Eq 4.2	231.465	-12092	36.7816	0	Posey and Rochelle, (1997)
Eq 4.3	216.049	-12432	-35.4819	0	Posey and Rochelle, (1997)
Eq 4.4	18.135	3814.4	0	-0.0151	Hetzer et al. (1967)
Eq 4.5	-4.6185	3616.1	0	0	Ermatchkov et al. (2003)
Eq 4.6	14.042	3443.1	0	0	Ermatchkov et al. (2003)
Eq 4.7	0.3615	1322.3	0	0	Ermatchkov et al. (2003)

The rate-controlled reactions are presented in Eqs 4.9-4.14. They control the mass transfer and the rate of absorption of CO2 by the PZ solvent.

$$CO_2 + OH^- \rightarrow HCO_3^- \quad 4.9$$

$$HCO_3^- \rightarrow CO_2 + OH^- \quad 4.10$$

$$PZ + CO_2 + H_2O \rightarrow PZCOO^- + H_3O^+ \quad 4.11$$

$$PZCOO^- + H_3O^+ \rightarrow PZ + CO_2 + H_2O \quad 4.12$$

$$PZCOO^- + CO_2 + H_2O \rightarrow PZ(COO^-)_2 + H_3O^+ \quad 4.13$$

$$PZ(COO^-)_2 + H_3O^+ \rightarrow PZCOO^- + CO_2 + H_2O \quad 4.14$$

Like the solvent-based PCC process using MEA described in Chapter 3, the power law is also used to calculate the rate of reaction for reactions in Eqs 4.9-4.14. The expression for the power-law was previously provided in Eq 3.11 of Chapter 3. The pre-exponential factor kinetic (k_j^o) and the activation energy (E_j) used in the power-law equation to calculate the rate of reactions ($R_{rxn,j}$) for reactions 4.9 to 4.14. are given in Table 4.2.

Table 4.2 Pre-exponential factor and activation energy for calculating the rate of reaction (Eqs 4.9-4.14) (Bishnoi and Rochelle, 2000; Pinsent et al., 1956)

Reactions	k_j^o $(m^3/kmol.s)$	E_j (kJ/kmol)
Eq 4.9	4.32×10^{13}	5.55×10^4
Eq 4.10	2.38×10^{17}	1.23×10^5
Eq 4.11	4.14×10^{10}	3.36×10^4
Eq 4.12	7.94×10^{21}	6.59×10^4
Eq 4.13	3.62×10^{10}	3.36×10^4
Eq 4.14	5.56×10^{25}	7.69×10^4

The Radfrac column used for the absorber and the stripper were divided into 20 stages. The counter-current flow model was used to estimate the bulk gas phase and liquid phase properties. It closely predicts the flow in the absorber and stripper and determines the bulk properties of the gas and liquid phases as an average of the inlet and outlet conditions (Razi et al., 2013). These bulk properties contribute to the calculation of reaction rates, mass and energy fluxes. The liquid phase film resistance was modelled with the "Discrxn" option. This is because the rapid reaction between CO_2 and PZ takes place in the liquid phase. In addition to this, this option accounts for reactions and diffusion resistance in the liquid film. Ten discretization points were used for the liquid phase in this study. The vapour phase film resistance was modelled with the "Film" option. This option accounts for diffusion resistance but not reaction. It does not require the vapour phase to be discretized into small segments.

4.3.2 Transport properties models

The thermo-physical properties otherwise known as transport properties such as density, viscosity, thermal conductivity, surface tension, and diffusivity were calculated in the rate-based model using the models in Table 4.3.

Table 4.3 Transport properties models used in the PCC rate-based model

	Liquid phase		Gas-phase	
Properties	Model	Reference	Model	Reference
Density	Rackett model	Rackett, (1970)	Redlich-Kwong EOS	Soave, (1972)
Viscosity	Jones-Dole model	Horvath, (1985)	Chapman-Enskog model	Bird et al. (2007)
Thermal conductivity	Riedel model	Aspentech, (2001)	Wassiljewa-Mason-Saxena model	Aspentech, (2001)
Surface tension	Hakim-Steinberg-Stiel with Onsager-Samaras model	Horvath, (1985)	Nil	Nil
Diffusivity	Wilke-Chang model	Wilke and Chang, (1955)	Chapman-Enskog-Wilke-Lee model	Aspentech, (2001)

4.3.3 Heat and mass transfer calculations

The mass and heat transfers in the absorber and the stripper of the process are accounted for using the correlations listed in Table 4.4. This includes the liquid film mass transfer coefficient, gas film mass transfer coefficient, liquid holdup, interfacial area and heat transfer coefficient.

Table 4.4 Mass and heat transfers correlations used in the absorber and stripper

	Liquid film mass transfer coefficient	Gas film mass transfer coefficient	Effective Interfacial area	Liquid holdup	Heat transfer coefficient
Absorber	Hanley and Chen, (2012)	Hanley and Chen, (2012)	Hanley and Chen, (2012)	Bravo et al. (1992)	Chilton and Colburn (1934)
Stripper	Hanley and Chen, (2012)	Hanley and Chen, (2012)	Hanley and Chen, (2012)	Bravo et al. (1992)	Chilton and Colburn (1934)

4.4 Model validation of PCC process using PZ at pilot-scale

4.4.1 Description of pilot plant test data

The rate-based model of the PCC process using PZ was validated at a pilot scale using experimental data reported by Plaza (2011) and Van Wagener (2011) for the absorber and the stripper respectively. The experiments were conducted at the SRP pilot plant located at the University of Texas at Austin. Fourteen experimental cases were conducted using a constant flue gas flow rate of 0.165 m^3/s. The absorber and the stripper have a diameter of 0. 427 m and packing height of 6.1 m. Mellapak 2X packing was used in the absorber and the stripper. The flue gas used in the experiments has a CO_2 concentration of 12 mol%. The details of data from the pilot plant used as input into the model during model validation are provided in Table 4.5.

Table 4.5 Details of the pilot plant data used as input into the rate-based PCC model using PZ (Plaza, 2011; Van Wagener, 2011)

Variables	Cases													
	1	**2**	**3**	**4**	**5**	**6**	**7**	**8**	**9**	**10**	**11**	**12**	**13**	**14**
PZ conc. (wt%)	38.85	40.15	43.87	41.06	39.97	41.17	40.69	40.15	40.06	39.51	29.06	29.65	29.44	28.32
Lean flow (kg/hr)	3744	3852	3780	3924	3024	4608	3852	3060	4536	3888	4464	4392	3636	2916
Lean temp (°C)	49.90	46.50	49.50	39.70	44.10	45.40	48.20	44.90	51.70	45.30	44.80	48.60	46.50	42.60
Lean loading (mol/mol)	0.26	0.31	0.25	0.39	0.28	0.30	0.31	0.30	0.27	0.33	0.32	0.27	0.26	0.26
Flue gas temp (°C)	15	0	0	21	7	-5	22	7	21	22	14	7	-9	8
Stripper pressure (bar)	1.379	1.378	1.379	1.379	1.379	1.378	4.136	4.136	3.156	3.156	3.156	3.446	3.446	3.446
Captured CO_2 (kg/hr)	118.80	93.6	129.60	39.60	100.80	111.60	93.60	82.80	115.20	64.80	79.20	115.20	111.60	93.60
Condenser temp (°C)	14.90	15.50	9.00	22.00	11.30	4.70	19.60	16.20	20.10	25.20	8.00	11.50	4.80	4.80
Condenser rate (kg/s)	0.02	0.008	0.019	0.002	0.011	0.012	0.005	0.004	0.011	0.013	0.004	0.011	0.010	0.009
Reboiler temp (°C)	107.20	103.00	108.90	87.50	105.70	104.10	127.50	127.50	129.00	116.10	119.70	127.60	128.20	127.00
Reboiler duty (kW)	130.60	101.00	155.50	45.90	111.10	125.30	112.70	105.60	141.30	79.00	99.80	134.60	129.00	114.50

4.4.2 Validation results

The rate-based model is validated using the fourteen experimental cases shown in Table 4.5. The model predictions are plotted against experimental data in Figures 4.4-4.6 Figure 4.4 displays the results for the model predictions against experimental data for CO2 capture level. It shows that the model predictions agree with the experimental data. The model predicted the CO2 capture level for all experimental cases except for cases 6 and 13 where the deviations are not within ±10%. The reason for this might be as a result of the negative flue gas temperature used for these cases during the experiments.

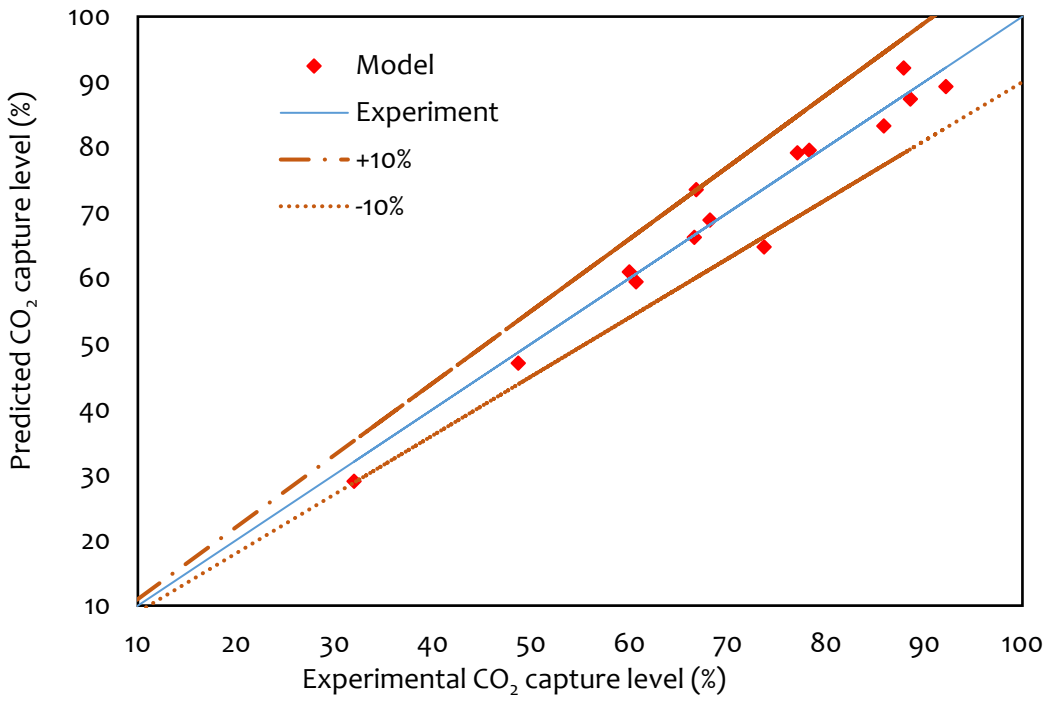

Figure 4.4 Model predictions of CO_2 capture level against experimental data for the fourteen experimental cases

The model predictions of the rich CO_2 loading are plotted against experiment data in Figure 4.5. The model predictions agree with the experimental data. Generally, the deviations between the model predictions and the experimental data are within ±10% for all the fourteen cases.

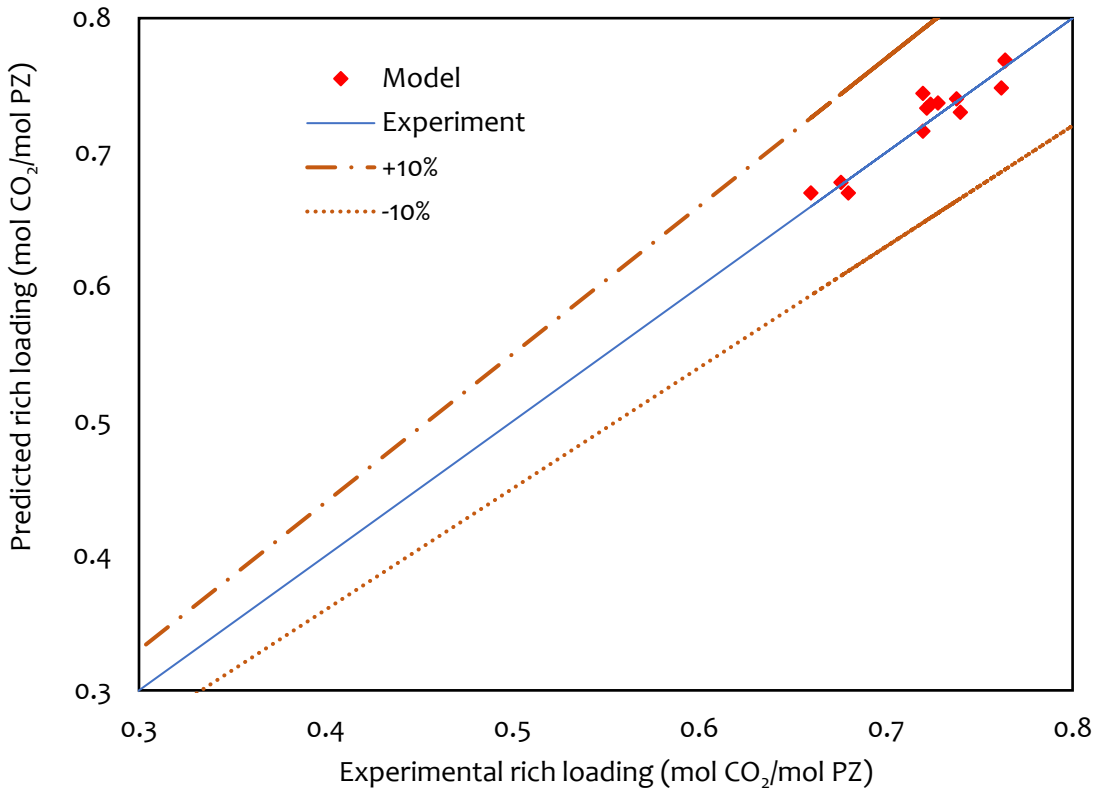

Figure 4.5 Model predictions of rich CO_2 loading against experimental data for the fourteen experimental cases

Figure 4.6 outlined the results for the model predictions against experimental data for specific reboiler duty. This figure shows that the model predictions are in good agreement with the experimental data. Although the deviations between the model and experimental data are generally less than ±10% for all the fourteen cases, the deviations are higher at stripper pressures above 3 bar than at stripper pressures below this value. This is because the heat losses at stripper pressures above 3 bar are 2 times the losses at stripper pressure below this value. These good agreements between the model predictions and the experimental data demonstrate the reliability of the solvent-based PCC rate-based model developed in this study.

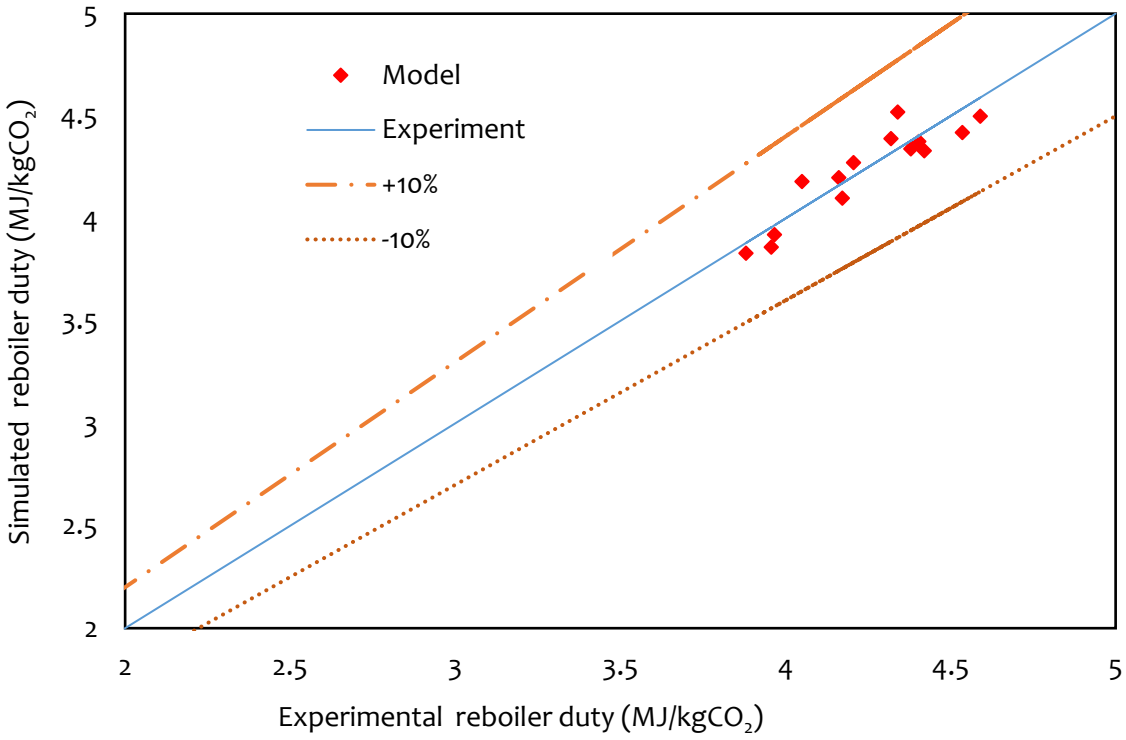

Figure 4.6 Model predictions of specific reboiler duty against experimental data for the fourteen experimental cases

4.5 Model scale-up for 250 MWe CCGT power plant

The rate-based model set up in section 4.3 and validated at pilot scale in section 4.4 is scaled up to a large-scale solvent-based PCC process using PZ. The large-scale PCC process will operate with flue gas from a 250 MW_e CCGT power plant at a 90% CO2 capture level. The flue gas conditions are the same as those used for the large-scale PCC process using MEA developed in Chapter 3. The flue gas conditions are from Canepa et al. (2013) and are presented in Table 4.6. The lean PZ solvent flow rate needed by the large-scale PCC to achieve a 90% CO2 capture level was calculated using Eq 3.26 presented previously in chapter 3. The number of equivalents/moles of amine is 2 for PZ, therefore the value of ž in Eq 3.26 is 2 for PZ solvent. A solvent absorption capacity of 0.2 mol_{CO2}/mol_{PZ} from the pilot plant was used to calculate the amount of lean PZ solvent required by the large-scale PCC process.

Table 4.6 Flue gas condition from a 250 MW_e CCGT power plant

Input parameters		Value
Flue gas	Flow rate (kg/s)	356
	Temperature (°C)	40.0
	Compositions (wt%)	CO2: 7.60
		H_2O: 4.70
		N2: 86.2
		Ar: 1.50

The diameters of the absorber and stripper of the large-scale PCC process using PZ was calculated using the scale-up method proposed in Chapter 3 of this thesis (Otitoju et al., 2020). The diameters were calculated from the flooding velocity using Eqs 3.23-3.25. The diameter of the absorber was estimated to be 12.50 m while that of the stripper was estimated to be 8 m. The packing type (Mellapak 2X) used in the absorber and the stripper of the pilot plant during the experiments was used in the large-scale PCC process. Three different configurations (standard, absorber intercooling (AI) and absorber intercooling with advanced flash stripper (AIAFS)) of the large-scale PCC process using PZ were simulated. The dimension of the absorber and stripper in each configuration of the PCC process using PZ are presented in Table 4.7.

Table 4.7 Absorber and stripper dimensions used for the various configurations of the large-scale PCC process using PZ

	Absorber		Stripper	
	Diameter (m)	Packing height (m)	Diameter (m)	Packing height (m)
Standard configuration	12.5	20	8	20
AI configuration	12	15	8	15
AIAFS configuration	12	15	7.6	10

4.6 Large-scale solvent-based PCC process using PZ solvent

4.6.1 Simulation of the various PCC process configuration in Aspen Plus®

The three process configurations described in section 4.2 are simulated in this section using PZ concentrations of 30, 35 and 40 wt% for each configuration. These PZ concentrations are chosen to avoid operational issues due to high solvent viscosity. Above 40 wt%, the viscosity of PZ solvent greatly increases. For instance, an increase in PZ concentration from 40 wt% to 45 wt% resulted in a 54% increase in viscosity from 0.011 to 0.024 Pa.s (Chen et al., 2017; Freeman and Rochelle, 2011). High viscosity would impede heat transfer in the heat exchanger, interfere with mass transfer and hinder the free flow of solvent in the system. These can increase the size of heat exchangers, pumps and other process equipment. This could consequently lead to an increase in the capital and operating costs of the process. In addition to this, the CO_2 loading of the lean solvent was varied from 0.16 to 0.3 mol_{CO2}/mol_{PZ} for all the configurations. The stripper pressure in all the configurations was maintained at 1.65 bar, thereby leading to changes in temperatures required to attain the value of lean loading in the regenerated solvent leaving the stripper bottom (Otitoju et al., 2021). Although PZ is resistant to thermal degradation up to 150 °C (Mazari et al., 2014), a maximum temperature of 120 °C was utilized for PZ solvent regeneration in this work. The flue gas conditions in Table 4.6 are kept constant throughout the simulations.

Table 4.8 Input parameters used to simulate the large-scale PCC process using PZ

	Quantity	Value
Capture level	(%)	90.0
Lean solvent	PZ Conc. (wt%)	30.0, 35.0, 40.0
	Temperature (°C)	40.0
Pump pressure (bar)	Rich solvent pump outlet	2.10
	Lean solvent pump outlet	1.65
Cross-heat exchanger	Approach temp. (°C)	10.0
Column pressure (bar)	Absorber	1.01
	Stripper	1.65
Condenser temperature	Temperature (°C)	25.0

The standard configuration of the PCC process was simulated first. The parameters presented in Table 4.7 and Table 4.8 were used as inputs to the large-scale PCC process model in Aspen Plus®. Following this, the AI configuration was simulated. This was done by incorporating an intercooler into the absorber. The pump-around intercooling was used due to its better performance compared to the in-and-out intercooling when dealing with flue gas from gas-fired power plants (Gao and Rochelle, 2020). The AI was implemented in Aspen Plus® by withdrawing liquid from a lower stage, cooled to 35 °C in the intercooler and fed back to an upper stage in the absorber. Figure 4.7 shows the model topology of the standard configuration of the solvent-based PCC process using PZ in Aspen Plus®. The only difference between the standard configuration and the AI is the intercooler in the absorber. However, since the AI was implemented in the absorber using the pump-around functionality in Aspen plus®, there is no physical presence of the AI on the absorber as previously depicted Figure 4.2. This makes the model topology of the standard configuration to have the same physical appearance as the model topology for the AI. For this reason, the model topology for AI is not included in this thesis.

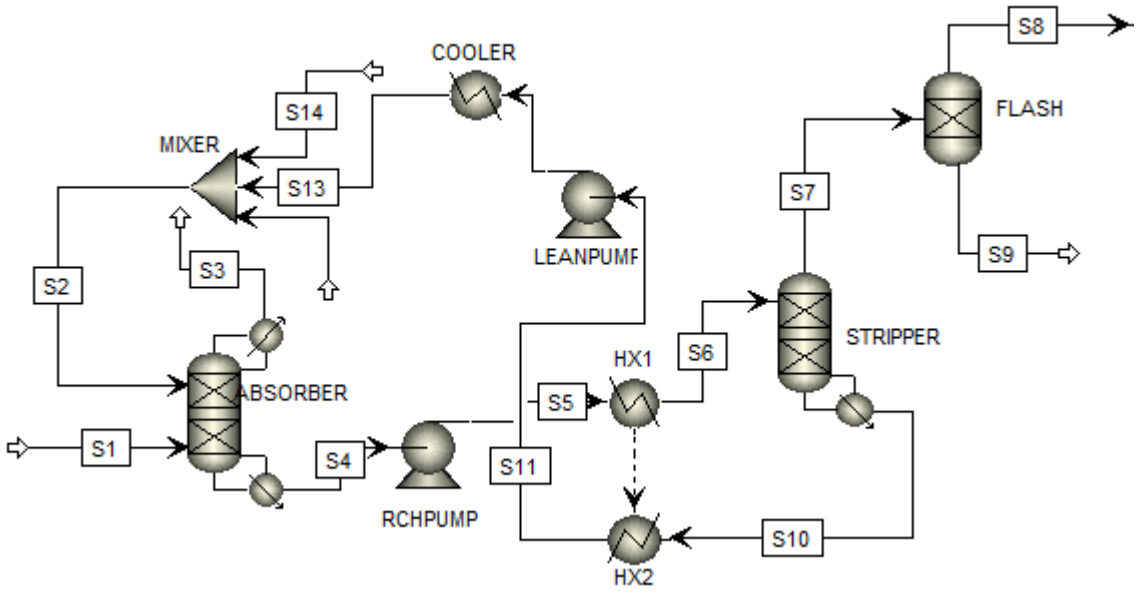

Figure 4.7 Model topology of the standard configuration in Aspen Plus®

In the AIAFS configuration, the stripper is modified to include more heat exchangers and splitters. The stripper of the AIAFS was implemented with the Radfrac block. The heat exchangers were implemented with two heater blocks connected with a heat stream. The

stripper was configured with 20 stages. Stage 1 to stage 19 is the packed sections of the packing. The last stage 20 is the flash tank. The last stage (stage 20) was modelled with lower solvent hold-up and residence time than stages 1 to 19 to reduce the degradation of the solvent. Figure 4.8 shows the model topology for the AIAFS in Aspen Plus®.

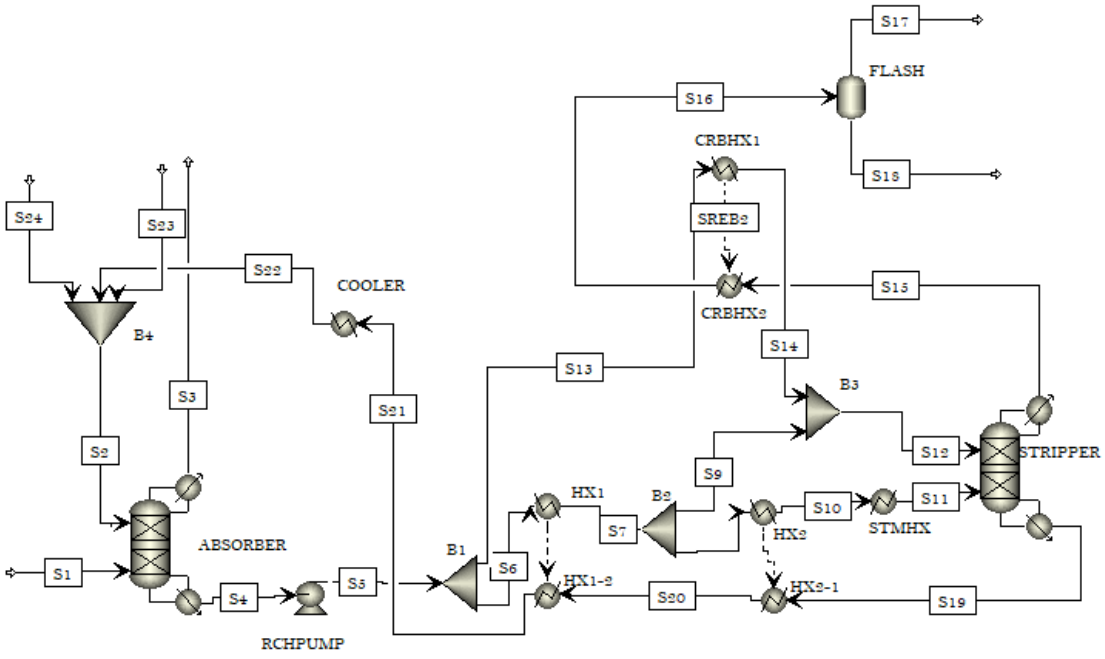

Figure 4.8 Model topology for the AIAFS in Aspen Plus®

4.6.2 Comparison of the solvent-based PCC process using 30 wt% PZ against 30 wt% MEA

The standard configuration of the solvent-based PCC process using the 30 wt% MEA benchmark solvent is generally regarded as the baseline of the process. Process performance based on modifications to the process configuration, change in solvent type or change in solvent concentrations is often compared to the baseline process. Therefore, the performance of the standard configuration of the solvent-based PCC process using 30 wt% PZ is compared to that of the standard configuration of the large-scale solvent-based PCC using 30 wt% MEA reported in Chapter 3 (Otitoju et al., 2020) and Canepa et al. (2013). The same flue gas conditions are used in these studies. The only difference between the studies by Otitoju et al. (2020), Canepa et al. (2013) and Otitoju etal. (2021) is the packing type used in the absorber and the stripper.

Figure 4.9 shows the influence of the lean CO_2 loading on the regeneration energy for the standard PCC process using 30 wt% PZ. The highest regeneration energy of 3.88 GJ/t_{CO_2} was realized at lean loading of 0.3 $mol_{CO_2}/mol_{PZ.}$ Compared to the regeneration energies achieved at the same lean loading for the 30 wt% PCC process (Table 4.9) the 30 wt% PZ process attained lower regeneration energy. The regeneration energy of the standard PCC process using 30 wt% PZ is lower than that of the standard PCC process using 30 wt% MEA (shown in Table 4.9) by 17.3% and 22% respectively. The lowest regeneration energy of 3.20 GJ/t_{CO_2} was realized at lean loading of 0.2 $mol_{CO_2}/mol_{PZ.}$ This is about 32% and 36% lower than the regeneration energy for the 30 wt% MEA process. The low sensible heat of PZ and less PZ solvent flowrate into the stripper are essential to the low energy consumption (Otitoju et al., 2021).

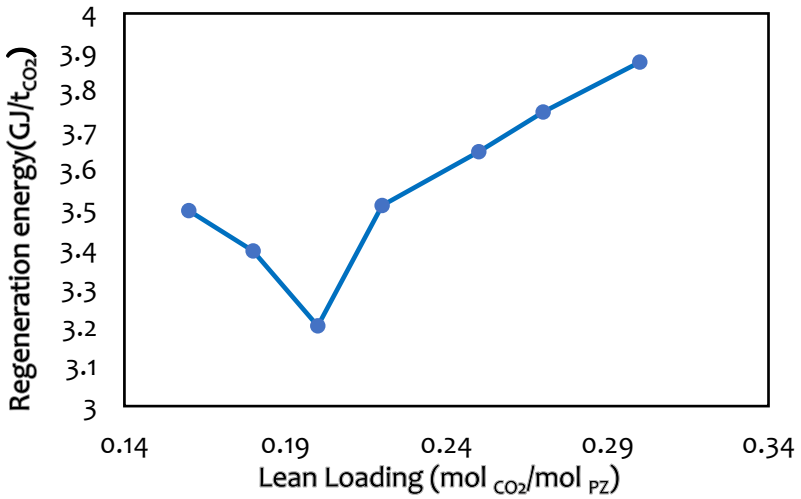

Figure 4.9 Influence of lean loading on regeneration energy for the standard PCC process using 30 wt% PZ.

Table 4.9 shows the comparison between the standard PCC process using 30 wt% MEA and using 30 wt% PZ. The L/G ratio of the 30 wt% PZ process is lower due to the lower solvent flow rate required to attain a 90% capture level. The solvent flow rate for the 30 wt% PZ process is 405 kg/s resulting in an L/G ratio of 0.90 kg/kg. The L/G ratio for the 30 wt% MEA process is 2.02 kg/kg. The reason for the lower L/G ratio by the 30 wt% PZ process is the higher absorption capacity of the PZ solvent. This higher absorption capacity resulted in higher rich loading of 0.57 mol/mol for the 30 wt% PZ process in contrast to the 0.46 mol/mol attained in the 30 wt% MEA process. The lower L/G ratio translates to lower

solvent flow to the process and consequently lower regeneration energy consumption, lower pumping and cooling energy demands and lower heat dissipation in the cross-heat exchangers.

The column dimensions are also smaller for the PCC process using 30 wt% PZ. The absorber diameter is lower by about 11% while the stripper diameter is lower by about 2.4%. The packing heights for both columns are lower by about 33%. The reason for this is the higher absorption capacity of PZ (Freeman et al., 2010) and the structured packing (Mellapak 2X) used in the columns. This packing is highly efficient and has a lower HTU thereby resulting in lower total packing height. These lower column dimensions and solvent flow rate could lead to lower capital and operating costs for the solvent-based PCC process using 30 wt% PZ compared to the baseline process.

Table 4.9 Process performance comparison for standard PCC process using 30 wt% PZ against standard PPC process using 30 wt% MEA

	30 wt% MEA process		30 wt% PZ
	Canepa et al. (2013)	Otitoju et al. (2020) (Chapter 3)	Otitoju et al. (2021) (This chapter)
Diameter (m)	14.0	13.8	12.5
Packing height (m)	30.0	28.5	20.0
L/G ratio	2.02	1.98	0.90
Regeneration energy (GJ/t_{CO_2})	4.97	4.69	3.20

4.7 Technical performance assessment

4.7.1 Regeneration energy performance assessment

The technical performance of the three process configurations of the PCC process using 30, 35 and 40 wt% PZ was assessed based on the energy required to regenerate the PZ solvent in the PCC process. The regeneration energies of the standard, AI and AIAFS configurations of the PCC process using PZ was estimated at different PZ concentrations (30 wt%, 35 wt% and 40 wt%) and lean loading (0.16-0.3 mol_{CO_2}/mol_{PZ}).

Figure 4.10 presents the regeneration energy for the standard PCC process using 30, 35 and 40 wt% PZ. The regeneration energies were determined at different lean loadings. The highest regeneration energies were attained with 30 wt% PZ. At this PZ concentration, the regeneration energy was between 3.20 GJ/t_{CO_2} and 3.87 GJ/t_{CO_2}. For 35 wt% PZ the regeneration energy was between 2.93 GJ/t_{CO_2} and 3.78 GJ/t_{CO_2}. This range decreases from 2.73 GJ/t_{CO_2} to 3.69 GJ/t_{CO_2} when the PZ concentration was increased to 40 wt%. The dip in the curves in Figure 4.10 at lean loading of 0.2 mol_{CO_2}/mol_{PZ} represent the lowest regeneration energy for the PZ concentrations. The value of 2.73 GJ/t_{CO_2} is the lowest regeneration energy achieved with the standard configuration. This was achieved at 40 wt% PZ and lean loading of 0.2 mol_{CO_2}/mol_{PZ}. Likewise, the highest regeneration energies for each PZ concentration were attained when the lean loading was increased to 0.3 mol_{CO_2}/mol_{PZ}. At this lean loading (0.3 mol_{CO_2}/mol_{PZ}) there is more CO2 in the lean solvent. This impact the absorption capacity of the solvent and consequently results in more solvent being required to capture 90% of CO2. This increases solvent flow and the regeneration energy in the stripper.

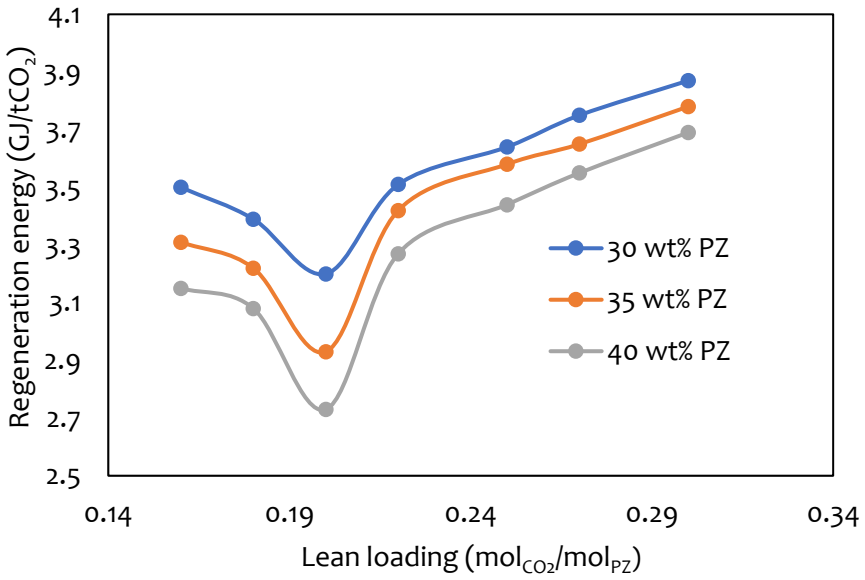

Figure 4.10 Influence of lean loading on regeneration energy for standard PCC process configuration at different PZ concentrations

The regeneration energy for the AI process configuration using 30, 35 and 40 wt% PZ are presented in Figure 4.11. Compared to the standard PCC process configuration, the AI

process configuration attained lower regeneration energy for all PZ concentrations. At 30 wt% PZ, the regeneration energy is about 4 to 10% less. It is about 6 to 10% less at 35 wt% PZ and 4 to 8 % less at 40 wt% PZ. As with standard PCC process configuration, the lowest and highest regeneration energies for the AI process configuration are attained at lean loading of 0.2 mol_{CO_2}/mol_{PZ} and 0.3 mol_{CO_2}/mol_{PZ} respectively. The lowest regeneration of 2.61 GJ/t_{CO_2} attained with the AI configuration is about 4.4% less than those the lowest regeneration attained in the standard process configuration. With the AI configuration, the lowest regeneration energy was attained with 40 wt %.

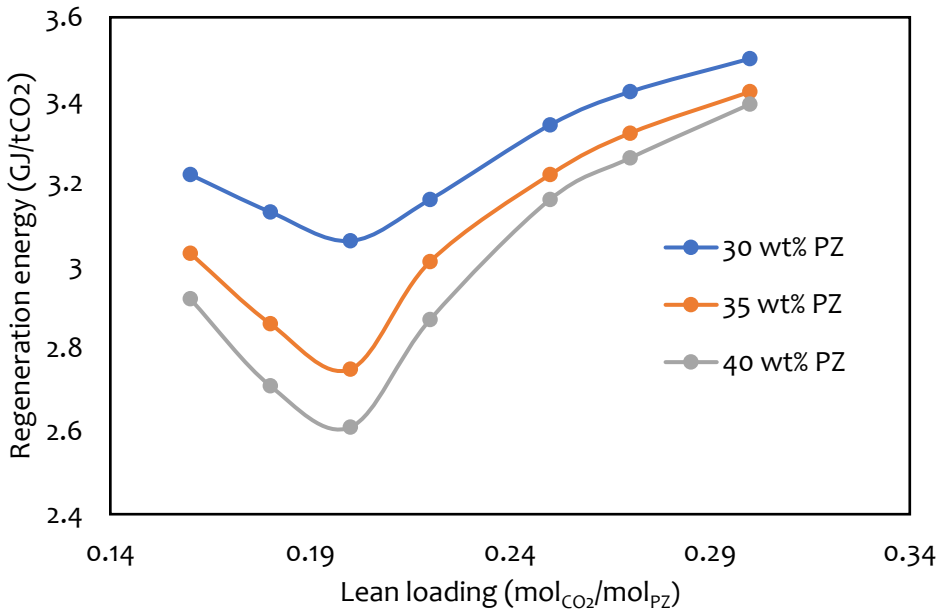

Figure 4.11 Influence of lean loading on regeneration energy for AI PCC process configuration at different PZ concentrations

Figure 4.12 shows the regeneration energy for the AIAFS PCC process configuration at 30, 35 and 40 wt% PZ concentration. The AIAFS process configuration enhances the energy performance of the PCC process. However, this configuration adds to the complexity of the PCC process. At 30 wt% PZ, the AIAFS attained regeneration energy of 2.5 $GJ/_{CO_2}$ to 2.99 GJ/t_{CO_2}. It attained regeneration energy of 2.5 GJ/t_{CO_2} to 3.1 GJ/t_{CO_2} at 35 wt% and 2.4 GJ/t_{CO_2} to 3.2 GJ/t_{CO_2} at 40 wt% PZ. For all the process configurations and PZ concentrations, the lowest generation energy of 2.41 GJ/t_{CO_2} was attained with AIAFS using 40 wt% PZ at lean loading of 0.22 mol_{CO_2}/mol_{PZ}.

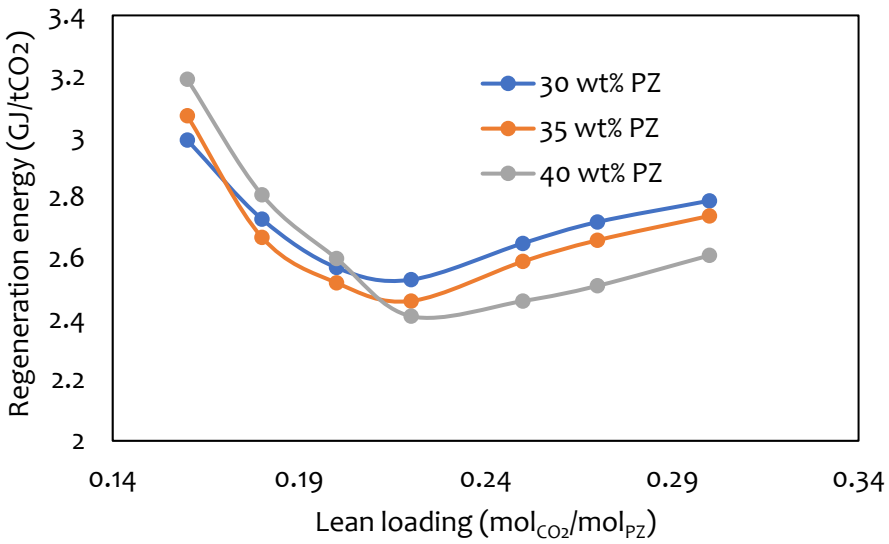

Figure 4.12 Influence of lean loading on regeneration energy for AIAFS PCC process configuration at different PZ concentrations

4.7.2 Equivalent work performance assessment

In addition to the regeneration energy, the performance of the different configurations of the PCC process at different PZ concentrations is also assessed based on the amount of energy required for pumping and compression of CO2. The sum of these energies is the total energy needed by the PCC process to capture and compress one tonne of CO2. The regeneration energy is estimated based on the steam used in the reboiler for solvent regeneration while the energy consumed by pumps are compressor are estimated based on the electrical energy used for their operation. The equivalent work can be used to present these energies on the same basis (Oyenekan and Rochelle, 2007). The equivalent work helps to determine the amount of electricity that can be produced from the steam used for solvent regeneration.

Additionally, the total equivalent work required of a baseline PCC process using 30 wt% MEA is estimated and compared to that of the PZ processes. The equivalent work of the steam utilized for solvent regeneration (W_{reg}) was determined using Eq 4.14 which is based on Carnot efficiency method.

$$W_{reg} = \eta_{turbine} Q_{reb} \left(\frac{T_{reb} + \Delta T - T_{sink}}{T_{reb} + \Delta T} \right) \qquad 4.14$$

Where Q_{reb} is the reboiler duty, T_{reb} is the temperature in the reboiler, T_{sink} is the sink temperature (40 °C) and ΔT is the steam side temperature approach (10 °C). The turbine efficiency ($\eta_{turbine}$) is 76% (Lin and Rochelle, 2014; Oyenekan and Rochelle, 2007).

Eq 4.15 gives the total equivalent work (W_{eq}) of the PCC process. It is the addition of the equivalent work for the regeneration, pump and compression(Lin and Rochelle, 2014).

$$W_{eq} = \eta_{turbine} Q_{reb} \left(\frac{T_{reb} + \Delta T - T_{sink}}{T_{reb} + \Delta T} \right) + W_{comp} + W_{pump} \qquad 4.15$$

$W_{pump}$is the pump work and it is based on the total head needed to circulate the solvent through the process. It was obtained from the energy required to operate the pump block in the Aspen Plus® simulation. W_{comp} is the compression work. This was obtained from the energy required to compress the CO2 from 1.65 bar (stripper pressure) to about 150 bars. The compression train was simulated in Aspen Plus®. It comprises four compressors with coolers between them. The coolers are used to reduce the temperature of the CO2 gas after each compression stage. The CO2 gas was cooled to 26 °C after the last compression stage (Otitoju et al., 2021).

The contributions of W_{reg}, W_{pump} and W_{comp} to W_{eq} for the standard PCC process configuration at 30, 35 and 40 wt% PZ are shown in Table 4.10. Additionally, the W_{eq} of the baseline process with 30 wt% MEA was evaluated. The values of each component of W_{eq} are were normalized by the tonnes of CO_2 captured. For each process configuration, the values of W_{eq} were determined only for cases with the lowest regeneration energy based on assessments in section 4.7.1.

The baseline process (standard PCC process using 30 wt% MEA) has a W_{eq} of 5.43 GJ/t_{CO2}. For each of the PZ concentrations, the highest and lowest contributions to W_{eq} are from W_{reg} and W_{pump} respectively. The W_{reg} of the standard PCC process using PZ reduced by 35% at 30 wt% PZ, 41% at 35 wt% PZ and by 45% at 40 wt% PZ compared to W_{reg} of the baseline process. This resulted in a corresponding decrease in W_{eq} for the standard PCC process using PZ. In addition to the W_{eq}, the cooling demands of the standard PCC process for each solvent were also calculated and included in Table 4.10.

Table 4.10. Equivalent work of the standard PCC process configuration with 30 wt% MEA and 30 wt% -40 wt% PZ

	Solvent concentration (wt%)			
	30 (MEA)	30 (PZ)	35 (PZ)	40 (PZ)
W_{reg} (GJ/t_{CO_2})	4.97	3.20	2.93	2.72
W_{comp} (GJ/t_{CO_2})	0.37	0.35	0.35	0.35
W_{pump} (GJ/t_{CO_2})	0.003	0.002	0.001	0.001
W_{eq} (GJ/t_{CO_2})	5.34	3.56	3.28	3.07
Cooling (GJ/t_{CO_2})	2.10	1.92	1.52	1.36

The contributions of W_{reg}, W_{pump} and W_{comp} to W_{eq} for the AI PCC process configuration at 30, 35 and 40 wt% PZ are shown in Table 4.11. The AI PCC process configuration attained the lowest W_{reg} (2.61 GJ/t_{CO_2}) and W_{eq} (2.96 GJ/t_{CO_2}) at 40 wt% PZ. These values are 4% and 3.6% lower than the lowest values of W_{reg} and W_{eq} obtained with the standard PCC configuration. Additionally, the cooling demands of the AI PCC process for each PZ concentration are also included in Table 4.11

Table 4.11 Equivalent work of the AI PCC process configuration using 30 wt% -40 wt% PZ

	PZ concentrations (wt%)		
	30	35	40
W_{reg} (GJ/t_{CO_2})	3.05	2.75	2.61
W_{comp} (GJ/t_{CO_2})	0.35	0.35	0.35
W_{pump} (GJ/t_{CO_2})	0.002	0.001	0.001
W_{eq} (GJ/t_{CO_2})	3.42	3.11	2.96
Cooling (GJ/t_{CO_2})	1.80	1.39	1.35

When the PZ concentration increased from 30 wt% to 40 wt%, the cooling demands reduced for the AI configuration by 25%. The cooling demand of 1.35 GJ/t_{CO_2} obtained at 40 wt% is the lowest for this process configuration. Compared to the standard process with 40 wt% PZ, the cooling demands reduce by about 1 %.

The contributions of W_{reg}, W_{pump} and W_{comp} to W_{eq} for the AIAFS PCC process configuration at 30, 35 and 40 wt% PZ are shown in Table 4.12. The lowest value of W_{eq} (2.76 GJ/t_{CO_2}) for the AIAFS configuration was obtained at a PZ concentration of 40 wt%. The W_{reg} (2.41 GJ/t_{CO_2}) is also lowest at this concentration. The value of 2.51 GJ/t_{CO_2} obtained for the W_{reg} of the AIAFS using 30 wt% PZ is very close to the value of 2.5 GJ/t_{CO_2} reported by Gao et al. (2019) using the same configuration and PZ concentration at the pilot scale. The W_{reg} and the W_{comp} are the two highest contributors to W_{eq} showing that the highest energy penalties result from solvent regeneration and CO_2 compression.

Table 4.12 Equivalent work of the AIAFS PCC process configuration using 30-40 wt% PZ

	PZ concentrations (wt%)		
	30	35	40
Cold rich bypass split fraction	0.30	0.30	0.20
Warm rich bypass split fraction	0.50	0.50	0.60
W_{reg} (GJ/t_{CO_2})	2.51	2.45	2.41
W_{comp} (GJ/t_{CO_2})	0.35	0.35	0.35
W_{pump} (GJ/t_{CO_2})	0.002	0.002	0.001
W_{eq} (GJ/t_{CO_2})	2.87	2.81	2.76
Cooling (GJ/t_{CO_2})	1.28	1.16	1.09

When PZ concentration was increased from 30 wt% to 40 wt%, the cooling demand of the AIAFS configuration was reduced by 14%. The lowest cooling energy demand (10.9 GJ/t_{CO_2}) for the AIAFS configuration was attained using a PZ concentration of 40 wt%. This is 20% and 19% lower than the lowest cooling demands attained with the standard and AI configurations. The AIAFS configuration has the best energy performance among the three PCC process configurations. For each process configuration, the best energy performances were obtained at a PZ concentration of 40 wt%. Therefore, economic analysis assessments are carried out only for the standard, AI and AIAFS PCC process configurations using 40 wt% PZ in section 4.7.3.

4.8 Economic performance assessments

In this section, the economic performance of the process configurations (standard, AI and AIAFS) with the least regeneration energy and equivalent work from section 4.7 is assessed. For each of these configurations, the least regeneration energy and equivalent work were attained using 40 wt% PZ. The economic assessment of the baseline process with 30 wt% MEA was also carried out and used as a reference to which the PZ processes were compared. The economic assessment was carried out in Aspen Economic Process Analyzer® (APEA). APEA is a platform within the Aspen Plus® simulator with costing models for different process equipment. It is based on material and energy balances, process flowsheet and equipment parameters.

Before exporting the simulated PCC process from Aspen Plus to APEA for economic assessment, it must be ensured that the PCC models give very accurate results and converge without any errors. Additionally, utilities such as cooling water, electricity, make-up solvent and water, etc and their costs must be set up with the model. Any error in the model or the costing procedures could lead to errors in the final economic analysis results generated by APEA. Upon exporting to APEA, the various model blocks are mapped with appropriate equipment cost models. Following this, the model blocks are sized according to the relevant design codes. The APEA does not have any equipment cost model for the splitters used in the AIAFS configuration. The splitters were therefore mapped and sized as an item with zero cost (Aspentech, 2012).

After mapping and sizing, APEA estimates and generates comprehensive cost results for the PCC process. This includes the direct costs for individual process equipment, capital expenditure (CAPEX) and operating expenditure (OPEX). The CAPEX is calculated from the individual and direct costs of process equipment such as the absorber, stripper, heat exchangers, pumps and compressor, while the OPEX is calculated from the fixed operating and maintenance cost (FOMC) and variable operating and maintenance cost (VOMC). FOMC includes costs for labour, administration, laboratory, total maintenance etc. It was estimated as 3% of the CAPEX (Luo, 2016). VOMC includes costs of solvent and utilities (cooling water, electricity, solvent and water make-ups). It was estimated as the product of the amount of the utilities (derived from Aspen Plus simulation) and their unit price is shown in Table 4.13.

Due to the lower rate of degradation, solvent loss in the PZ process is lower compared to the MEA process. In MEA process, solvent loss is between 0.3 kg/t_{CO2} to 2.4 kg/t_{CO2} (Lepaumier et al., 2011; Moser et al., 2011), while it is 0.05 kg/t_{CO2} in PZ process (Manzolini et al., 2015). Therefore, solvent loss of 1.5 kg/t_{CO2} and 0.05 kg/t_{CO2} was adopted when costing the make-up solvent for the MEA and the PZ processes respectively. The electricity was cost using the default value in APEA.

Table 4.13 Utility unit price (Li et al., 2016)

Utilities	Unit	Value
Cooling water	($/m^3)	0.35
Make-up (unit cost)	MEA cost ($/tonne)	1500
	PZ cost ($/tonne)	8000
	water cost ($/m^3)	3.0
Electricity	($/kW)	0.0775
plant operating time/yr	(hr)	8000

The annual capital cost (ACC) and the annual operating cost add up to the total annual cost (TAC) of the PCC process. The ACC was determined from the annualized CAPEX using Eq.4.16 (Agbonghae et al., 2014; Karimi et al., 2011). The TAC was calculated from Eq. 4.17 as the sum of the ACC and OPEX.

$$\mathrm{ACC} = \frac{\mathrm{CAPEX}}{((1+\mathrm{i})^{\mathrm{n}}-1)\Big/\mathrm{i}(1+\mathrm{i})^{\mathrm{n}}} \qquad 4.16$$

Whereas *n* denotes the project life with the value of 20 years, *i* denotes the interest rate at 10%. The project life was chosen to be 20 years because the PCC process is not yet to be fully mature.

$$\mathrm{TAC} = \mathrm{ACC} + \mathrm{OPEX} \qquad 4.17$$

4.8.1 Results of economic assessments

The results of the economic performance assessments of the standard, AI and AIAFS PCC process configurations using 40 wt% PZ are presented in this section. The results for the economic performance assessment of the baseline PCC process using 30 wt% MEA are also presented. The PZ processes are compared to the 30 wt% MEA process. The economic performance is assessed based on the CAPEX, TAC and CO_2 avoided costs (Otitoju et al.,

2021). The direct cost (DC) and total direct cost (TDC) extracted from APEA for each of the four processes considered are shown in Table 4.14. The largest contributions to the TDC are from the cost of the absorbers. This is followed by the cost of compressors and strippers.

Table 4.14. TDC for solvent-based PCC process using 30 wt% MEA and 40 wt% PZ

	Standard configuration		AI configuration	AIAFS configuration
Solvent concentrations	30 wt% MEA	40 wt% PZ	40 wt% PZ	40 wt% PZ
Equipment	DC (M$)	DC (M$)	DC (M$)	DC (M$)
Absorber	25.20	14.70	12.63	12.63
Lean pump	0.30	0.15	0.15	0.15
Compressor	5.34	5.37	5.37	5.37
Storage tank	0.65	0.45	0.45	0.47
Rich pump	0.34	0.14	0.14	0.15
Flash separator	0.16	0.16	0.16	0.14
Condenser	0.36	0.32	0.29	0.23
Reflux drum	0.87	0.87	0.87	Nil
Reboiler	0.75	0.62	0.56	Nil
Reflux pump	0.28	0.28	0.28	Nil
Stripper	9.52	6.15	4.63	4.13
Lean cooler	0.37	0.19	0.14	0.23
Main cross-heat exchanger	5.56	0.72	0.59	Nil
TDC	49.68	30.10	Nil	Nil
		Absorber Intercooler	0.11	0.12
		Intercooler pump	0.13	0.25
		Cold-cross exchanger	Nil	0.44
		Hot-cross exchanger	Nil	0.34
		Cold-rich exchanger	Nil	0.21
		Steam heater	Nil	0.50
		Flash Tank	Nil	0.39
		TDC	26.46	25.75

The CAPEX and the breakdown used to calculate it for the PZ process using the standard, AI and AIAFS configurations and the baseline process using 30 wt% MEA are presented in Table 4.15. The CAPEX breakdown followed Li et al. (2016) approach. The three configurations of the PZ process attained a significantly lower CAPEX compared to the

baseline process with 30% MEA. This is because of the lower column (absorber and stripper) diameter and packing height achieved by the PZ processes. The PZ processes required packing heights of 20 and 15 m in the absorber and stripper for standard and AI configurations. The AIAFS configuration required an absorber and stripper diameter of 15 and 10 m for 90% CO2 capture while the baseline process required a packing height of 30 m in both columns. This difference in packing height led to a 39.6%, 46.7%Y% and 48.3% reduction in the CAPEX of the standard, AI and AIAFS PCC process using 40 wt% PZ compared to the baseline PCC process using 30 wt% MEA.

For the processes using 40 wt% PZ, despite adding an intercooler and a pump to the absorber of the AI process configuration, its CAPEX is 11.7% lower than that of the standard process configuration. The reason for this is that intercooling reduces the PZ solvent temperature in the absorber and enhances its absorption capacity. This resulted in about a 5 m reduction in absorber packing height and 356 m^3 (about 17%) reduction in absorber packing volume for the AI process configuration compared to the standard process configuration. In cost terms, the absorber in the AI process configurations is less by about M$2.1 compared to the absorber in the standard process configuration. The intercooler and pump added a total of M$0.24 to the cost of the absorber in the AI configuration. Overall, the AI reduced the cost of the absorber in the PCC process by M$1.86 compared to the standard PCC process with 40 wt% PZ.

Furthermore, the addition of heat exchangers, steam heater and a flash tank to the AIAFS configuration although increased the complexity of the process, did not add significantly to the CAPEX. The lowest CAPEX was attained by the AIAFS configuration. The majority of the reduction in CAPEX is from the stripper and its components such as the steam heater and condenser. In the stripper, the temperature of the hot vapour (mostly CO_2) leaving the stripper top is cooled in the condenser to about 25 °C. As a result, sensible heat and latent heat of excess water vapour are lost. The lost work in the cross exchanger and the condenser could be as high as 70% of the total lost work during regeneration (Lin and Rochelle, 2016; Otitoju et al., 2021). This is responsible for the lower efficiency of the standard stripper compared to the advanced flash stripper (AFS) used in the AIAFS configuration. In the AIAFS configuration, the AFS recovers heat from the hot vapour using the cold rich heat exchanger. This eliminates the condenser lost work and improves the

energy performance of the process. Therefore, compared to the stripper used in the standard and AI configurations, the AFS used in the AIAFS configuration has a smaller condenser which cost about M$0.1 less. Additionally, the cost of the steam heater used in the AIAFS configuration is M$0.12 and M$0.06 less than the cost of the reboiler used in the standard and AI configurations. This translates to about 19 and 11% increase in the cost of the reboiler in the standard and AI configurations to the steam heater used in the AIAFS configuration.

Table 4.15 CAPEX breakdown for the large-scale process using 40 wt% PZ and the baseline process 30 wt% MEA

	TDC	TIC	BEC	EC	EPC	PC	PJC	TPC	OC	CAPEX
	TDC	20%TDC	TDC+TIC	27%BEC	127%BEC	25%BEC	20%EPC+5%BEC	120%EPC+30%BEC	15%TPC	115% TPC
SC 30 wt% MEA (M$)	49.68	9.93	59.60	16.10	75.70	14.90	18.10	109	16.30	125.35
SC 40 wt% PZ (M$)	30.10	6.10	36.10	9.74	45.80	9.02	11.00	65.80	9.87	75.67
AI configuration 40 wt% PZ (M$)	26.46	5.30	31.80	8.59	40.40	7.96	9.68	58.10	8.71	66.82
AIAFS 40 wt PZ (M$)	25.75	5.15	30.90	8.35	39.30	7.73	9.40	56.40	8.46	64.86

SC: Standard configuration; TIC: Total indirect cost; BEC: Bare erected cost; EC: Engineering and contractor; EPC: Engineering Procurement and construction; PC: Process contingency; PJC: Project contingency; TPC: Total plant cost; OC: Owner's cost; CAPEX: Total capital expenditure

The ACC, FOMC and VOMC of the different configurations of the PCC process using 40 wt% PZ are compared in Table 4.16 to the baseline PCC process (standard PCC using 30 wt% MEA). The values of ACC, FOMC and VOMC are less for the PZ processes. Among the components that make up the VOMC, the cost of electricity is the largest. The VOMC is the highest contributor to the total annual cost (TAC) of the PCC process. The AIAFS configuration using 40 wt% PZ has the smallest values of ACC, FOMC, VOMC and TAC. The CO2 capture cost (CCC) for the AIAFS configuration is also the smallest at 34.65 $/t$_{CO_2}$ while the CO2 capture cost of the baseline process is the highest at 61.13 $/t$_{CO_2}$. This is about a 42% reduction in the CO2 capture cost. Among the PZ processes, the CO2 capture cost was reduced from 40 $/t$_{CO_2}$ with standard configuration to 37.7 $/t$_{CO_2}$ with AI configuration to 34.65 with AIAFS configuration.

Table 4.16 TAC and CO2 capture cost the large-scale PCC process using 40 wt% PZ and the baseline process 30 wt% MEA

		Standard configuration		AI configuration	AIAFS configuration
		30 wt% MEA	40 wt% PZ	40 wt% PZ	40 wt% PZ
CAPEX (M$)		125.35	75.67	66.82	64.86
ACC (M$/yr)		14.70	8.89	7.84	7.62
FOMC (M$/yr)		3.75	2.27	2.00	1.95
VOMC (M$/yr)	Electricity	24.54	18.32	18.14	16.02
	Cooling water	0.42	0.22	0.30	0.13
	make-up Water	0.52	0.56	0.56	0.55
	make-up solvent	0.88	0.31	0.31	0.31
TAC (M$/yr)		44.81	30.60	29.15	26.58
CCC ($/t$_{CO_2}$)		61.13	40.00	37.71	34.65

4.9 Conclusion

In this chapter, a steady-state closed-loop model of the solvent-based PCC process using PZ was developed in Aspen Plus®. The model was validated at a pilot scale using experimental data collected by Plaza (2011) and Van Wagener (2011). The model results agree with the experimental data and model predictions were within ±10% of experimental

data. The validated pilot-scale PCC process model was scaled to a large-scale PCC process model with capacity for flue gas from a 250 MW_e CCGT power plant. Technical and economic assessments of the various configurations of the large-scale PCC process using 30, 35 and 40 wt% PZ were carried out and compared to a large-scale standard PCC process using 30 wt% MEA (baseline). The following are the key findings from this chapter;

- The technical assessment of the large-scale PCC process shows that the regeneration energy of the standard PCC process can be reduced from 4.97 GJ/t_{CO_2} using 30 wt% MEA to 3.20 GJ/t_{CO_2} using 30 wt% PZ. With the AIAFS configuration and 40 wt% PZ solvent, the least regeneration energy of 2.41 GJ/t_{CO_2} was attained.
- The total energy needed to capture and compress one tonne of CO2 by the PCC process was assessed using the equivalent work (W_{eq}). For the standard configuration, the PCC process using 30 wt% PZ has the highest W_{eq} of 5.34 GJ/t_{CO_2}. With PZ, this was reduced to 3.56 GJ/t_{CO_2} with 30 wt% PZ, 3.28 GJ/t_{CO_2} with 35% PZ and 3.07 GJ/t_{CO_2} with 40 wt% PZ. The W_{eq} were further reduced with the absorber intercooling configurations and PZ solvent. The AIAFS PCC process configuration using 40 wt% PZ gave the lowest W_{eq} value of 2.76 GJ/t_{CO_2} among all the cases considered.
- The economic assessment of the large-scale PCC process shows that the total annual cost (TAC) and the CO_2 capture cost (CCC) of the standard PCC process using 30 wt% MEA was M$44.81/year. This reduces to M$30.60/year with 40 wt% PZ. The AIAFS PCC process configuration using 40 wt% PZ gave the lowest TAC and CCC of M$26.58/year and $34.65/$t_{CO_2}$ respectively.
- This is the first study to provide insights on the energy and cost requirements of the large-scale PCC process using PZ based on a detailed technical and economic assessment

Chapter 5: Steady-state model development of the RPB absorber for solvent-based PCC process

5.1 Overview

This chapter describes the development of a steady state rate-based model for CO_2 absorption with MEA in RPB absorber. The model equation framework is implemented in ACM®. To begin with, the RPB operating principle is described in Section 5.2. The material and energy balances of the gas and liquid phases are presented in section 5.3. This is followed in Section 5.4 by a detailed explanation of the mass and heat transfer correlations used in the RPB model. Section 5.5 summarizes the hydrodynamic models used to calculate the liquid holdup, effective interfacial area and pressure drop in the RPB model. The thermodynamic properties calculations namely the Vapour Liquid Equilibrium (VLE) and the chemical equilibrium are described in Section 5.6. In Section 5.7, the various physical properties calculations and physical properties procedural calls from Aspen Properties are described. The motor power consumption calculation equation is presented in Section 5.8 and the procedures for RPB model implementation in ACM® is described in Section 5.9. The details of the convergence criteria used to limit errors in the obtained solutions are described in Section 5.10. The Chapter conclusion is given in Section 5.11.

5.2 RPB operating principles

The RPB consists of an annular packed bed attached to two side disks that are mounted on a rotating shaft and housed in a casing. A sectional view of the RPB is shown in Fig 5.1. The RPB may be used as an absorber or as a stripper. The gas and the liquid flow across the bed in either co-current (flow in the same direction) or counter-current (flow in opposite direction) flow depending on the design of the RPB. The liquid generally flows radially outward from the inner periphery of the packing due to centrifugal acceleration. The gas, on the other hand, enters into the casing and then flows radially inward from the outer periphery of the RPB due to the pressure gradient. The gas and the liquid phases are exposed to enormous centrifugal acceleration that is many times the gravitational acceleration in packed columns. This extends flooding limits and enhances mass transfer in the bed and areas between the packing and the casing (Luo et al., 2012a; Rao et al., 2004). This is the reason for the substantial reduction in packing volume in RPBs compared

to PB. The bed in RPB is often made of materials such as beads (Chen and Liu, 2002), expamet (Jassim et al., 2007) or wire mesh (Luo et al., 2012b).

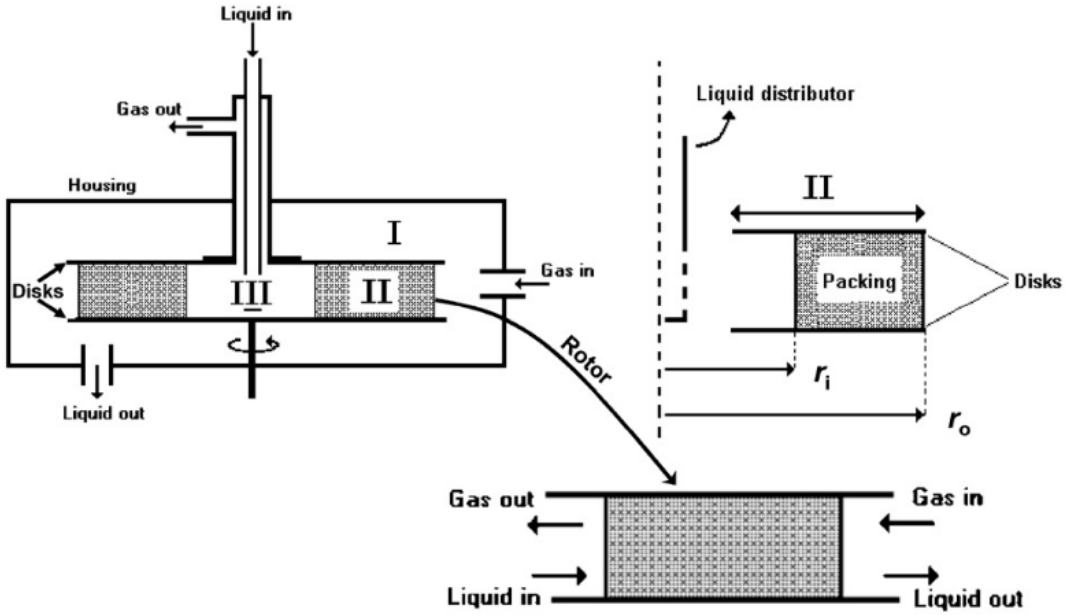

Figure 5.1 Cross-sectional view of RPB (Llerena-Chavez and Larachi, 2009)

5.3 Material and energy balances

5.3.1 Model assumptions

The material and energy balances equations are an essential part of the model describing CO_2 absorption in RPB. These balance equations for RPB are a modified version of the balance equations for PB. The following assumptions are made for the steady-state model development of the RPB absorber and stripper.

- No accumulation in the bulk gas as well as the liquid and gas films
- The gas phase is assumed to be an ideal gas.
- The vapour phase consists of CO_2, H_2O, N_2 and MEA.
- One-dimensional differential mass and energy balances for both the liquid phase and the gas phase.
- Gas and liquid flow in the radial direction only.
- All reactions are assumed to occur in the liquid phase and an enhancement factor is used to account for these reactions
- The liquid phase consists of ionic species namely OH^-, H_3O^+, HCO_3^-, CO_3^{2-}, $MEAH^+$, and $MEACOO^-$ in addition to the four original components CO_2, H_2O, N_2 and MEA.

- Mass transfer between the liquid and the vapour phases only include CO_2, H_2O, N_2 and MEA. Mass transfer is assumed to be zero for the ionic species.
- Heat losses to the surroundings are negligible.

5.3.2 Material balances for the gas and liquid phases

The equations describing the mass balances for the gas and liquid phases in an RPB are shown in Eqs 5.1 and 5.2. These model equations are derived based on the model assumptions listed in Section 5.3.1.

Material balance of the gas phase:

$$0 = \frac{1}{2\pi r Z}\frac{\partial\left(F_g y_i\right)}{\partial r} - a_{gl}N_i \qquad 5.1$$

Material balance for the liquid phase:

$$0 = -\frac{1}{2\pi r Z}\frac{\partial(F_l x_i)}{\partial r} + a_{gl}N_i \qquad 5.2$$

Where F_g and F_l are the gas and liquid molar flow rates, y_i and x_i are the components mole fractions in the gas and liquid phases, N_i are the components molar transfer fluxes and a_{gl} is the gas-liquid interfacial area. The cross-sectional area (A) of the RPB is represented by $2\pi r$ and Z is its height.

5.3.3 Energy balances for the gas and liquid phase

The equations for the energy balance in the gas and liquid phases are shown in Eqs. 5.3 and 5.4.

Energy balance of the gas phase:

$$0 = \frac{1}{2\pi r Z}\frac{\partial\left(F_g C_{p,g} T_g\right)}{\partial r} - a_{gl}h_{gl}\left(T_l - T_g\right) \qquad 5.3$$

Energy balance of the liquid phase:

$$0 = -\frac{1}{2\pi r Z}\frac{\partial\left(F_l C_{p,l} T_l\right)}{\partial r} + a_{gl}\left(h_{gl}\left(T_l - T_g\right) - \Delta H_{rxn}N_{CO2} - \Delta H_{vap,H2O}N_{H_2O}\right) \qquad 5.4$$

Where T_g and T_l are the temperatures of the gas and liquid phase, $C_{p,g}$ and $C_{p,l}$ are the specific heat capacity of the gas and liquid phases, h_{gl} is the interfacial heat transfer

coefficient, ΔH_{rxn} is the heat of absorption/desorption of CO_2 (87,000 kJ/kmol; (Kang et al., 2014)) and $\Delta H_{vap,H2O}$ is the heat of vaporization of H_2O at T_l in the RPB. It was calculated with the simple and reliable Watson's equation expressed in Eq. 5.5.

$$\frac{\Delta H_{vap,H2O,bp}}{\Delta H_{vap,H2O}} = \left(\frac{T_c - T_{bp}}{T_c - T_l}\right)^{0.38} \qquad 5.5$$

T_{bp} is the temperature of water at boiling point (373.15 K), Tc is the critical temperature (647.3 K) and $\Delta H_{vap,H2O,bp}$ is the heat of vaporization at boiling point (40,660 kJ/kmol).

5.4 Mass and heat transfer models

The mass transfer of CO_2 between the liquid and vapour phase is a very important component of the RPB modelling. The detailed correlations used for the mass and heat transfer coefficients calculation are explained in this section.

5.4.1 Mass transfer flux

The rate of mass transfer of components between phases in the RPB is derived based on the two-film theory wherein the mass transfer flux is calculated as follows (Kang et al., 2014):

$$N_i = K_{tot,i}\left(P_{g,i} - P_i^*\right) \qquad 5.5$$

N_i is the mass transfer flux of the components, $P_{g,i}$ is the partial pressure of component *i* in the gas phase and P_i^* is the equilibrium partial pressure of component i. The overall mass transfer coefficient of component *i* based on the gas phase ($K_{tot,i}$) is obtained by Eq. 5.6. It is expressed as the inverse of the sum of the gas and liquid film resistances.

$$K_{tot,i} = \frac{1}{\frac{RT_g}{k_{g,i}} + \frac{He_{l,i}}{E_i k_{l,i}}} \qquad 5.6$$

Where $k_{g,i}$ and $k_{l,i}$ are the gas and the liquid mass transfer coefficients, $He_{l,i}$ is Henry's constant for the components, and E_i is the enhancement factor of component *i*. The mass transfer resistance in the gas and the liquid film is considered only when calculating $K_{tot,i}$ for CO_2. For the other components (N_2, H_2O, and MEA), the liquid film resistance is neglected, therefore, the expression for $K_{tot,i}$ for these components is given by:

$$K_{tot,i} = \frac{k_{g,i}}{RT_g} \quad 5.7$$

R is the universal gas constant.

5.4.2 Enhancement factor

The enhancement factor is the factor used to quantify the effect of chemical reactions on mass transfer. It depends on the concentration, rate of reaction and the diffusivities of the reactants and the products. The enhancement factor is calculated using Eq 5.8 which is based on the pseudo-first-order reaction regime and is widely used in CO_2 absorption with MEA (Kang et al., 2014; Kvamsdal et al., 2009; Oko et al., 2018).

$$E_i = \frac{\sqrt{k_{app} D_{l,CO_2}}}{k_{l,CO_2}} \quad 5.8$$

Where D_{l,CO_2} is the liquid diffusivity of CO_2, k_{l,CO_2} is the liquid mass tranfer coefficient of CO_2. The apparent reaction rate constant (k_{app}) is calculated using a termolecular kinetic model described by Aboudheir et al. (2003). The model was developed by considering important operating variables in CO_2 absorption such as temperature, MEA concentration and CO_2 loading. This kinetic model is based on the overall reaction between CO_2 and MEA. The reaction rate based on the termolecular mechanism is expressed in Eq. 5.9.

$$r_{CO2-MEA} = k_{app} Cl_{CO2} = \left(k_{MEA} Cl_{MEA} + k_{H_2O} Cl_{H_2O}\right) Cl_{MEA} Cl_{CO_2} \quad 5.9$$

Where k_{MEA} and k_{H2O} are the third order reaction rate constant for components MEA and H2O. Cl_i is the concentration of component *i*. The kinetic expressions for k_{MEA} and k_{H2O} are obtained from linear regression of experimental data and are shown in Eqs. 5.10 and 5.11 (Aboudheir et al., 2003).

$$k_{MEA} = 4.61\ x\ 10^9 exp\left(\frac{-4412}{T}\right) \quad 5.10$$

$$k_{H_2O} = 4.55\ x\ 10^6\ exp\left(\frac{-3287}{T}\right) \quad 5.11$$

Substituting Eqs. 5.10 and 5.11 for k_{MEA} and k_{H2O} in Eq 5.9 and divide both sides of the equation by Cl_{CO_2} yields.

$$k_{app} = 4.61\ x\ 10^9 exp\left(\frac{-4412}{T}\right) Cl_{MEA}^2 + 4.55\ x\ 10^6\ exp\left(\frac{-3287}{T}\right) Cl_{H_2O} Cl_{MEA} \quad 5.12$$

This kinetic model has been demonstrated to be reliable for CO_2 absorption with high MEA concentrations (Kang et al., 2014; Oko et al., 2018).

5.4.3 Liquid film mass transfer coefficient

Different correlations have been proposed by researchers such as Chen et al. (2006, 2005a, 2005b), Munjal et al. (1989b), Onda et al. (1968), Tung and Mah, (1985) to predict the liquid film mass transfer coefficient in RPBs. In this study, the liquid film mass transfer coefficient was calculated using the correlation by Tung and Mah (1985) expressed in Eq. 5.13. This correlation has been reported to give the best predictions of the liquid film mass transfer coefficient in RPBs among the set of correlations validated against experimental data by Oko et al. (2019).

$$\frac{k_l\, d_p}{D_l} = 0.919 \left(\frac{\mu_l}{D_l\, \rho_l}\right)^{\frac{1}{2}} \left(\frac{\mathrm{a_t}}{a_{gl}}\right)^{\frac{1}{3}} \left(\frac{d_p^3 \rho_l^2\, r\omega^2}{\mu_l^2}\right)^{\frac{1}{6}} \left(\frac{u_l \rho_l}{\mu_l a_t}\right)^{\frac{1}{3}} \qquad 5.13$$

Where k_l is the liquid film mass transfer coefficient, D_l is the liquid diffusion coefficient, $\mathrm{a_t}$ is the total surface area of packing, dp is the packing pore diameter, ρ_l is the liquid density, u_l is the liquid superficial velocity and μ_l is the liquid viscosity.

5.4.4 Gas film mass transfer coefficient

The Onda et al. (1968) gas film mass transfer correlation which was originally developed for predicting gas film transfer coefficient (k_g) in packed columns have been applied in RPB by several researchers (Borhani et al., 2018; Im et al., 2020; Joel et al., 2015), however, the correlation did not contain the gravity (g) term and as such did not account for the influence of centrifugal acceleration present in RPB. When used in RPB, Oko et al. (2019) reported that the predictions of the Onda correlation were in order of 10^{-1} in contrast to experimental values of order 10^{-2}. These over-predictions were due to the absence of rotational induced gas side resistance. This makes the Onda correlation to be inadequate for predicting the gas mass transfer coefficient in RPB.

In this study, the correlation developed by Chen (2011) for RPB based on two-film theory was used to calculate the gas film mass transfer coefficient. The correlation considers the end effect, centrifugal acceleration and packing geometry thereby making it applicable for RPB.

$$\frac{k_g a_{gl}}{D_g a_t^2}\left(1-0.9\frac{V_o}{V_t}\right)=0.023\left(\frac{u_g\rho_g}{\mu_g a_t}\right)^{1.13}\left(\frac{u_l\rho_l}{\mu_l a_t}\right)^{0.14}\left(\frac{d_p^3\rho_g^2 r\omega^2}{\mu_g^2}\right)^{0.31}\left(\frac{u_l^2\rho_l}{a_t\sigma}\right)^{0.07}\left(\frac{a_t}{a_p'}\right)^{1.4} \quad 5.14$$

$$V_o=\pi(r_s^2-r_o^2)z \quad 5.15$$

$$V_t=\pi r_s^2 z \quad 5.16$$

Where $k_{g,i}$ is the gas film mass transfer coefficient, D_g is the gas diffusivity, V_o is the volume between the outer radius of the bed and the stationary housing, V_t is the total volume of the RPB, σ is the critical surface tension, a_p' is the surface area of the 2 mm diameter bead per unit volume of the bead and r_s is the radius of the stationary housing.

5.4.5 Interfacial heat transfer coefficients

The interfacial heat transfer coefficient was calculated using the Chilton-Colburn analogy expressed in Eq. 5.17 (Chilton and Colburn, 1934).

$$h_{gl}=k_{l,ave}\rho_l C_{p,l}\left(\frac{\lambda_l}{\rho_l C_{p,l} D_{l,ave}}\right)^{\frac{2}{3}} \quad 5.17$$

Where h_{gl} is the heat transfer coefficient, $C_{p,l}$ is the liquid specific heat capacity, λ_l is the thermal conductivity of the liquid, $k_{l,ave}$ is the average liquid film mass transfer coefficient and $D_{l,ave}$ is the average liquid diffusivity.

5.5 Hydrodynamic models

5.5.1 Effective interfacial area

The gas-liquid interfacial area is calculated using the Billet and Schultes, (1999) correlation expressed in Eq 5.18. The choice of this correlation is because it has been shown by Oko et al. (2019) to give more accurate and consistent predictions of the interfacial area in RPBs compared to other correlations.

$$\frac{a_{gl}}{a_t}=1.5(a_t d_h)^{-0.5}\left(\frac{\rho_l u_l d_h}{\mu_l}\right)^{-0.2}\left(\frac{\rho_L u_l^2 d_h}{\sigma_l}\right)^{0.75}\left(\frac{u_l^2}{r\omega^2 d_h}\right)^{-0.45} \quad 5.18$$

Where a_{gl} is the effective gas-liquid interfacial area, d_h is the hydraulic diameter, a_t is the specific surface area of packing, σ_L is the liquid surface tension and ω is the rotating speed.

5.5.2 Liquid holdup

The liquid holdup represents the fraction of the liquid present in the void fraction of the packing. A reasonable value of liquid holdup is essential for effective mass and heat transfers between the gas and the liquid phases. Also, its calculation is necessary to accurately estimate the rates of reaction in the liquid film. The liquid holdup is calculated using the correlations of Burns et al. (2000) as expressed in Eq. 5.19. The correlation was developed by performing multiple regression analysis on experimental data collected using a resistance measurement technique. This technique considered the influence of liquid flow, liquid viscosity and centrifugal acceleration on holdup thereby making it more accurate when used to determine the liquid holdup in a model.

$$\varepsilon_L = 0.039\left(\frac{g}{g_0}\right)^{-0.5}\left(\frac{u_L}{U_0}\right)^{0.6}\left(\frac{\nu_L}{\nu_o}\right)^{0.22} \qquad 5.19$$

Where ε_L is the liquid holdup, g is the acceleration due to gravity, g_0 is the characteristic acceleration with a value of 100 m/s^2, U_0 is the characteristics superficial liquid velocity with a value of 0.01 m/s, ν_L is the liquid kinematic viscosity and ν_o is the characteristic kinematic viscosity with a value of 10^{-6} m^2/s. The superficial liquid velocity (u_L) is calculated as the ratio of the liquid volumetric flowrate to the area of the RPB as shown in Eq. 5.20

$$u_L = \frac{Q_L}{2\pi r z} \qquad 5.20$$

The gas holdup ε_g is the difference between the packing porosity and liquid holdup. It is obtained as follow (Kang et al., 2014):

$$\varepsilon_g = \varepsilon - \varepsilon_L \qquad 5.21$$

5.5.3 Gas-phase pressure drop

The pressure drop across the RPB (ΔP_{RPB}) is determined using the pressure drop correlation of Llerena-Chavez and Larachi (2009) expressed in Eq. 5.22. This correlation is based on Ergun-type semi-empirical relationships in which the pressure drops in the RPB are recomposed through additive aggregation of (1) gas-slip and radial acceleration effects (2) laminar and inertial drag effects and (3) the centrifugal effects.

$$\Delta P_{RPB} = \frac{150(1-\varepsilon)^2\mu_g}{d_p^2\varepsilon^3}\left(\frac{Q_g}{2\pi z}\right)In\frac{r_o}{r_i} + \frac{1.75(1-\varepsilon)\rho_L}{d_p\varepsilon^3}\left(\frac{Q_g}{2\pi z}\right)^2\left(\frac{1}{r_i}-\frac{1}{r_o}\right) + \frac{1}{2}\rho_g\omega^2(r_o^2-r_i^2) + \varepsilon\left(-0.08 - Q_g + (2000(RPM)^{1.22} + \omega^{1.22})Q_g^2\right) \quad 5.22$$

Where Q_g is the volumetric flow rate of the gas, μ_g is the gas viscosity and ε is the porosity of the bed.

5.6 Thermodynamic properties calculations

5.6.1 Vapour-Liquid equilibrium

Thermodynamic properties calculation is an important aspect of CO_2 absorption modelling. The ElecNRTL base method which is a heterogeneous thermodynamic approach (that utilizes the activity coefficient model for liquid phase properties calculations and the Redlich-Kwong equation of state for the gas phase properties calculations) was used in this study. The default ElecNRTL model in the Aspen properties system is only valid for MEA concentration of about 30 wt%. Therefore, the ElecNRTL model with updated parameters for higher (>30 wt%) MEA concentrations is used in this study (Oko et al., 2018). The updated ElecNRTL Aspen properties file was configured through a special feature (Physical properties configuration) that allows the Aspen properties file to be embedded within the ACM® platform. The embedded Aspen properties file is used by the ACM® to calculate important thermodynamic properties that are used to estimate the VLE. For CO_2 absorption, the VLE is represented by Eqs 5.23 and 5.24.

$$P_i^* = \gamma_i x_i P_i^{vap} \quad \text{for } i = MEA, H_2O \quad 5.23$$

$$P_i^* = H_{e,i} C_{l,i} \gamma_i \quad \text{for } i = CO_2, N_2 \quad 5.24$$

Where γ_i and P_i^{vap} are the activity coefficient and vapour pressures of component *i*. The Henry constant of nitrogen (H_{N2}) was obtained as 6.5e-4 from Kang et al. (2014). The activity coefficient was estimated using the ElecNRTL model while the vapour pressure was estimated using the extended Antoine equation. Both properties were called in ACM® using the properties procedure call functionality in ACM®.

5.6.2 Chemical Equilibrium

Chemical equilibrium otherwise known as speciation describes the concentration of the different species present in the liquid phase. The simplified speciation model presented by Gabrielsen et al. (2005) for CO_2 absorption into an aqueous solution of MEA is adopted in this study. The model considered only one equilibrium reaction and eliminates the complexities and the time-consuming computations associated with other speciation models. It combines both Henry's law constant (He) and the chemical reaction equilibrium constant (Keq) for carbamate (MEACOO-) formation. In the CO2 absorption process, the chemical equilibrium characterising the liquid phase is represented by the following equilibrium reactions.

$$2H_2O \leftrightarrow H_3O^+ + OH^- \quad 5.25$$

$$CO_2 + 2H_2O \leftrightarrow H_3O^+ + HCO_3^- \quad 5.26$$

$$HCO_3^- + H_2O \leftrightarrow H_3O^+ + CO_3^{2-} \quad 5.27$$

$$MEAH^+ + H_2O \leftrightarrow H_3O^+ + MEA \quad 5.28$$

$$MEACOO^- + H_2O \leftrightarrow MEA + HCO_3^- \quad 5.29$$

The fast carbamate reaction dominates in the CO_2 loading (0.02-0.48 mol_{CO2}/mol_{MEA}) range that is of interest in CO_2 capture with MEA. In this loading range, the concentration of ions such as HCO_3^-, OH^- and CO_3^{2-} is very small and therefore can be neglected. Because of this, reactions (Eqs 5.25-5.29) can be approximated by this single chemical equilibrium reaction.

$$MEAH^+ + MEACOO^- \overset{K'_{eq,CO2}}{\longleftrightarrow} 2MEA + CO_{2(aq)} \quad 5.30$$

Based on Eq. 5.30, the concentration of CO_2 in the liquid phase can be expressed as

$$[CO_{2(aq)}] = K'_{eq,CO2}\frac{[MEAH^+][MEACOO^-]}{[MEA]^2} \quad 5.31$$

Where $K'_{eq,CO2}$ is the equilibrium constant for the absorption and desorption reactions between CO_2 and MEA. It is given as:

$$K'_{eq,CO2} = \frac{K_{eq,CO2}}{H_e} \quad 5.32$$

Where $K_{eq,CO2}$ is the combined Henry's law and chemical equilibrium constants. By substituting Eq. 5.32 for $K'_{eq,CO2}$ into Eq. 5.31 and expressing the concentration of MEA and $MEAH^+$ as a function of the initial MEA concentration and CO_2 loading, Eq. 5.31 becomes:

$$[CO_{2(aq)}] = \left(\frac{K_{eq,CO2}[MEACOO^-]}{H_e}\right)\frac{CL_{MEA,0}\alpha}{[CL_{MEA,0}(1-2\alpha)]^2} \qquad 5.33$$

Where $[MEA] = CL_{MEA,0}(1-2\alpha)$ and $[MEAH^+] = CL_{MEA,0}\alpha$. $K_{eq,CO2}$ is determined from the expression in Eq. 5.34

$$K_{eq,CO2} = exp^{\left(A+\frac{B}{T}+CCL_{MEA,0}\alpha\right)} \qquad 5.34$$

$CL_{MEA,0}$ is the initial concentration of MEA. The values of the adjustable parameters A, B and C in Eqn 5.34 are shown in Table 5.1

Table 5.1 Adjustable parameters for equilibrium constant (Gabrielsen et al., 2005)

System	A	B	C
MEA-CO_2	30.96	-10584	-7.187

5.7 Physical properties calculations

5.7.1 Henry constant

The physical solubility of CO_2 in MEA is described using the N_2O analogy suggested by Clark (1964). Since it is impossible to directly measure it due to the chemical reaction between CO_2 and MEA, the physical solubility of CO_2 in MEA is represented using Henry's law constant. Ying et al. (2012) used the N_2O analogy method and presented the correlation for the physical solubility of the CO_2-MEA system as follows:

$$He_{CO_2,MEA} = He_{N2O,liq}\left(\frac{He_{CO_2,H_2O}}{He_{N_2O,H_2O}}\right) \qquad 5.35$$

Eq.5.35 is valid for a temperature range of 298.15-323.15K and an MEA concentration range of 0-100 wt%. He_{CO_2,H_2O} and He_{N_2O,H_2O} are the physical solubilities of N_2O and CO_2 in water (H_2O) respectively. The physical solubility of N_2O in H_2O (He_{N_2O,H_2O}) is estimated using Eq. 5.36 and He_{CO_2,H_2O} is calculated using Eq 5.37.

$$He_{N_2O,H_2O} = 8.449x10^6 exp^{(-2283/T)} \qquad 5.36$$

$$He_{CO_2,H_2O} = 3.520x10^6 exp^{(-2113/T)} \qquad 5.37$$

$He_{N2O,liq}$ is Henry's constant of N_2O in the liquid (MEA+H_2O). It is calculated using the expression in Eq. 5.38.

$$He_{N2O,liq} = exp^{(He_{excess}+\varphi_{H_2O} lnHe_{N_2O,H_2O}+\varphi_{MEA} lnHe_{N_2O,MEA})} \quad 5.38$$

Where φ_{MEA} and φ_{MEA} are the mass percentage of MEA and H_2O in the system. He_{excess} is the excess Henry's coefficient for the MEA+H_2O binary system. It is calculated from Eq. 5.39.

$$He_{excess} = \varphi_{H_2O}\varphi_{MEA}\tau_{1,2} \quad 5.39$$

$\tau_{1,2}$ is the parameter to describe the two-body interaction between MEA and H_2O. It can be estimated using the polynomial function in Eq. 5.40.

$$\tau_{1,2} = k_1 + k_2(T - 273.15) + k_3(T - 273.15)^2 + b\varphi_{H_2O} \quad 5.40$$

Parameters k_1, k_2, k_3 and b in Eq. 5.40 are 1.71468, 0.03955, -0.00043 and -2.21209 respectively. The term $He_{N_2O,MEA}$ in Eq. 5.38 is the solubility of N_2O in pure MEA. It is calculated from Eq 5.41.

$$He_{N_2O,MEA} = 2.448x10^5 exp^{(-1348/T)} \quad 5.41$$

Eqs (5.35)-(5.41) have been validated with experimental data by Ying and Eimer, (2012) for a temperature of 295.15-323.15K and MEA concentration of 0-100 wt%. The physical solubility of CO_2 in aqueous MEA was predicted with an absolute average deviation (AAD) of 1.49% from experimental data.

5.7.2 Property procedure calls

Other physical properties such as the density, viscosity and diffusivity of the gas and liquid phases also need to be calculated. They were calculated using the built-in Aspen Property procedures. The built-in procedures rely on Aspen Properties for physical properties calculations. The built-in Procedures are Fortran subroutines available in the modeller library. It works by calculating the required properties based on the temperature, pressure and composition of the phases.

5.8 Motor power consumption calculations

The energy consumption of the motor used to rotate the RPB absorber and stripper is estimated using Singh et al. (1992) correlation (Eq 5.42). This correlation accounts for both the frictional losses and the power required to accelerate the inlet liquids to the rotational speed at the outer radius of the RPB. The frictional losses in RPB are highly dependent on its design, therefore an advanced knowledge of the RPB design is essential for its accurate prediction (Singh et al., 1992).

$$P_m = 1.2 + 0.0011\rho_L r_o^2 \omega^2 Q_L \qquad 5.42$$

Where P_m is the motor power in kW, ρ_L is the liquid phase density, ω is rotating speed (rad/s) and Q_l is the volumetric flow rate of MEA solvent.

5.9 Model implementation and solution in ACM®

In RPB, the gas and the liquid flow in opposite direction. In this model, the gas phase is designated to flow in the forward direction from the outer radius (r_o) to the inner radius (r_i) of the RPB. On the other hand, the liquid phase is designated to flow in the backward direction from the inner radius to the outer radius of the RPB. The RPB model was created by declaring a domain and specifying its various properties such as the length, highest order derivative, spacing preference, section location and discretization method. The domain is the space over which the model variables are distributed and it is the length between r_i and r_o of the RPB.

The RPB model is made up of systems of algebraic and partial differential equations. To provide a numerical solution for the model, the RPB absorber and stripper were discretized into 20 elements (21 nodes) using the first-order backward finite differences method. The first node (node, 0) corresponds to r_i and the last node (20) (otherwise known as the end node) corresponds to r_o. The solution of the discretized equations requires boundary conditions to be specified. The following boundary conditions (BCs) were used to obtain a unique solution for the variables of the gas and liquid phase at each discretized point along the radius of the RPB.

gas-phase mass balance BC: $y_i = y_0$ at r = r_o and $\frac{\partial(F_g y_i)}{\partial r} = 0$ at r = r_i

liquid phase mass balance BC: $x_i = x_0$ at r = r_i and $\frac{\partial(F_l x_i)}{\partial r} = 0$ at r= r_o

gas-phase energy balance BC: $T_g = T_{g0}$ at r = r_o and $\frac{\partial(F_g C_{p,g} T_g)}{\partial r} = 0$ at r = r_i

liquid phase energy balance BC: $T_l = T_{l0}$ at r = r_i and $\frac{\partial(F_l C_{p,l} T_l)}{\partial r} = 0$ at r = r_o

5.10 Convergence criteria

The numerical methods in ACM® are approximation methods with associated errors. The errors in the obtained solution are kept within acceptable limits by either the variable or residual convergence criterion. The variable convergence criterion ensures that the difference between the values obtained in the current and previous solutions is below the error limit. Other the other hand, the residual convergence ensures that the difference between the values obtained for the left-hand side and the right-hand side of all model equations is below the error limit. Both convergence criteria were used in this work to check when a solution has been reached. The solver options indicating the convergence criteria and tolerances set-up used in the ACM® are shown in Figs. 5.2 and 5.3.

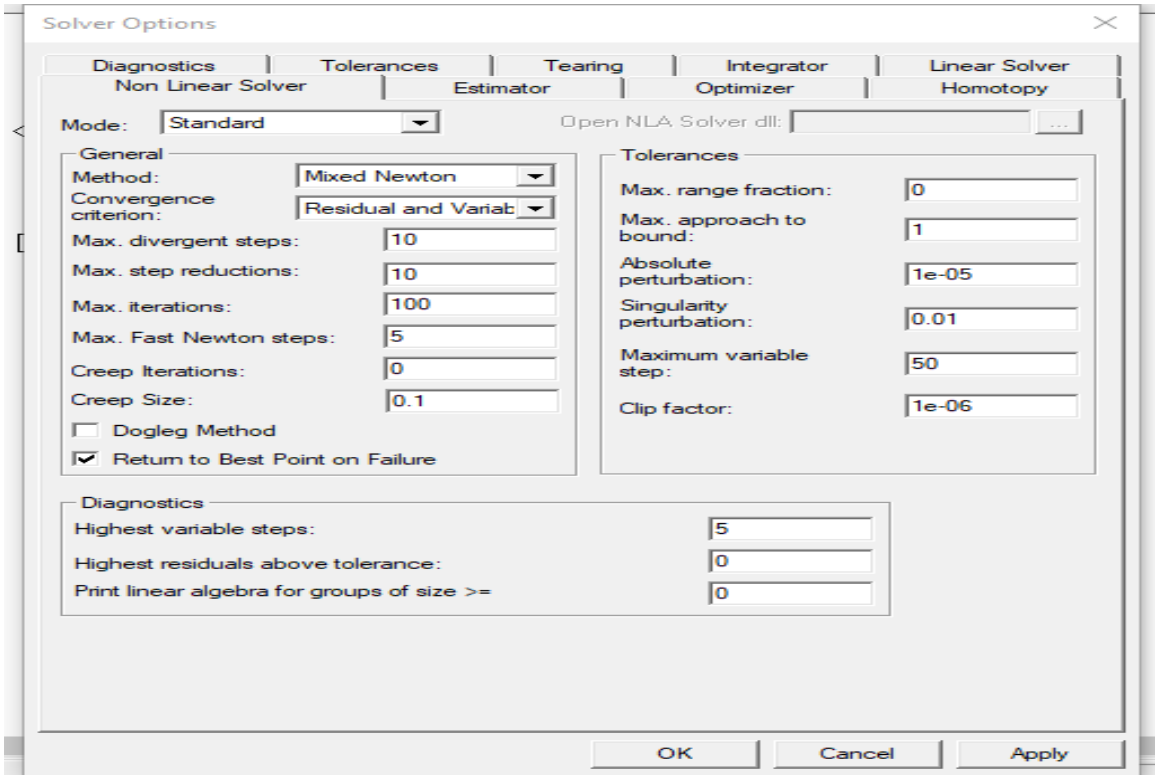

Figure 5.2 Non-linear Solver tab showing the convergence criterion and solution method in ACM®

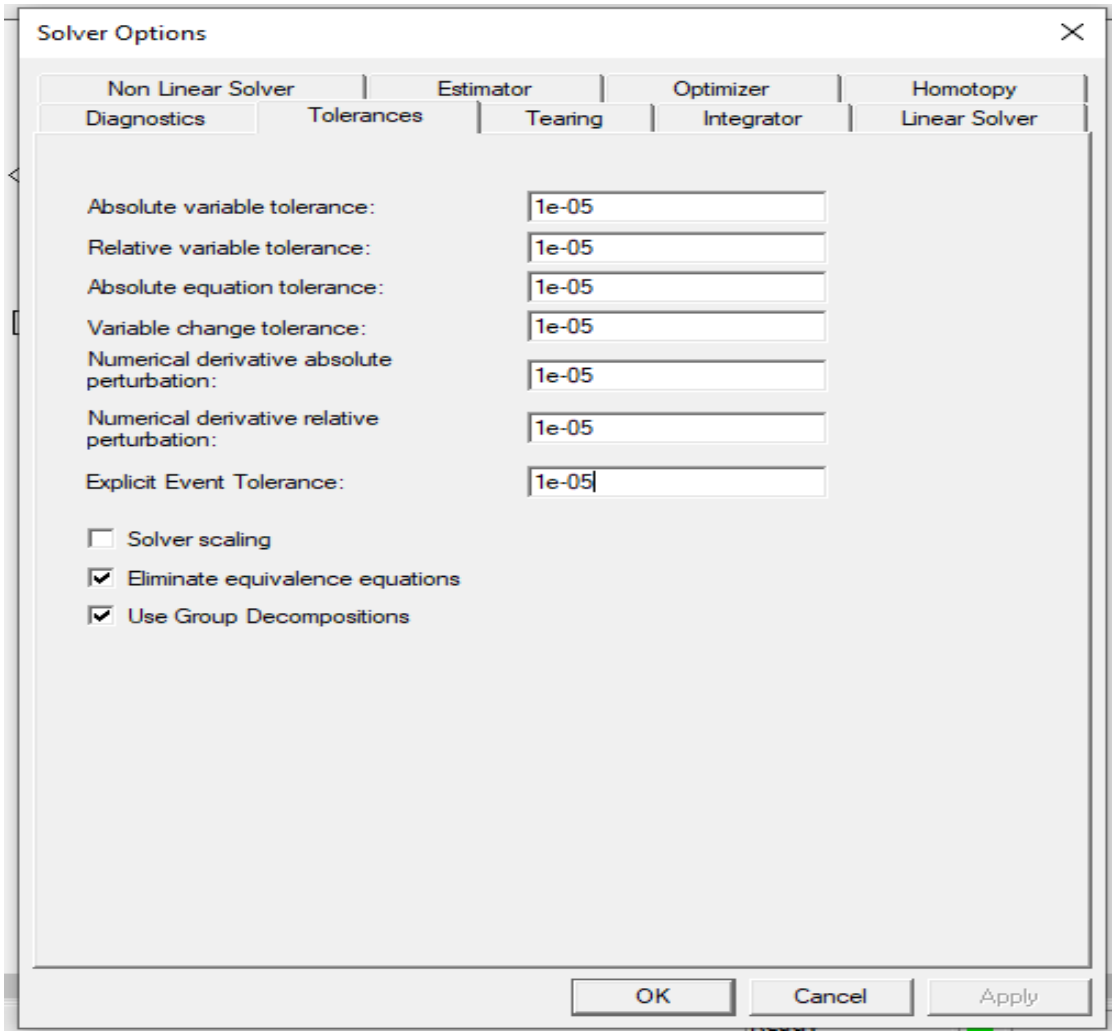

Figure 5.3 Tolerance tab showing the tolerances used in the ACM® simulation

5.11 Conclusion

In this chapter, the basic principle of RPB operation was introduced, followed by a detailed methodology for steady state rate-based model development for an RPB absorber in ACM®. The mass and energy balances equations in the gas and liquid phases were developed based on the assumptions presented in Section 5.3.1. Following this, a detailed discussion on mass and heat transfer in RPB using two-film theory was presented. For mass transfer, relevant correlations use to calculate the gas and liquid films mass transfer coefficient were discussed in detail. The effect of chemical reactions on mass transfer was accounted for in the model using the enhancement factor. The enhancement factor was calculated based on the assumption of a pseudo-first-order reaction regime. The correlation to calculate the interfacial heat transfer coefficient in the RPB model was also

presented. In addition to this, the reasons for choosing each correlation for their respective task in the model were also discussed.

Correlations for hydrodynamic properties namely effective interfacial area, liquid holdup, and pressure drop were also incorporated into the model. Thermodynamic properties which are important aspect of the CO_2 absorption modelling were calculated using the ElecNRTL thermodynamic method. Physical properties are fundamental to all modelling and simulation studies, therefore, good model predictions rest on selecting the right property package. A detailed discussion on how the various physical properties used in the model were calculated was presented. Model implementation strategy in ACM and the convergence criterion used to minimize error in the obtained solutions were also discussed.

Chapter 6: Model validation, scale-up and technical and economic performance analysis of a large-scale RPB absorber for solvent-based PCC

6.1 Overview

In this chapter, the steady-state model validation, scale-up and technical and economic analysis of a large-scale RPB absorber are presented. Section 6.2 describes the steady-state model validation of the RPB absorber at pilot scale using the experimental data reported by Jassim et al. (2007). A detailed iterative procedure for the scale-up of the RPB absorber model is presented in Section 6.3. In Section 6.4, the scale-up results for the RPB absorber used in the PCC process for a 250 MW_e CCGT power plant are presented. The technical assessment of the large-scale RPB absorber is presented in Section 6.5. The economic assessment of the large-scale RPB absorber is carried out in Section 6.6. In Section 6.7, a comparative study between the PCC process using PB and RPB technology is presented. A summary of the research findings is presented in Section 6.8 to end the chapter.

6.2 Steady-state model validation of the RPB absorber with experimental data

The model of the RPB absorber developed in Chapter 5 is validated with steady-state experimental data reported by Jassim et al. (2007). The flowsheet of the RPB rig used for Jassim's experiment is shown in Figure. 6.1.

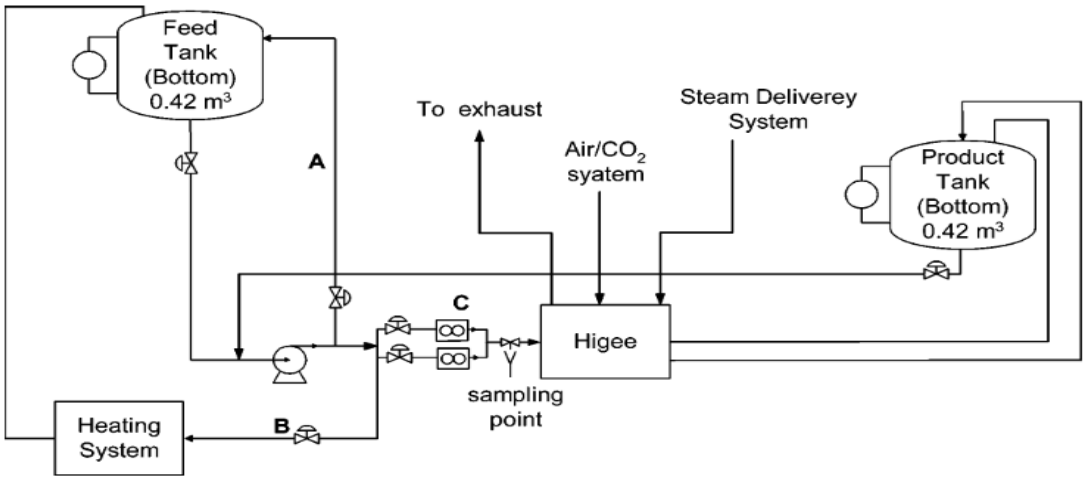

Figure. 6.1 Flowsheet of RPB facility used by Jassim (Jassim et al., 2007)

The rig was located in a flameproof enclosure equipped with adequate ventilation. The rotor of the RPB was made of stainless steel and the piping and storage tanks were made

of polypropylene. The dimensions of the RPB and the information about the packing in the RPB are shown in Table 6.1.

Table 6.1 RPB specification (Jassim et al., 2007)

Dimension	
Inner diameter (m)	0.156
Outer diameter (m)	0.396
Axial height (m)	0.025
Packing information	
Packing type	Expanded stainless steel small mesh
Total surface area per unit volume (m^2/m^3)	2132
Porosity (m^3/m^3)	0.76

The experimental data include four cases collected at average lean MEA concentrations of 55 and 75 wt% and lean MEA flow rates of 0.35 and 0.66 kg/s. Each case consists of four experimental runs with different lean CO_2 loading, lean temperature and rotational speed. For all the experimental runs, the flue gas flow rate was kept constant at 2.87 kmol/h thereby resulting in variable L/G ratios. Also, the flue gas temperature was kept constant at 283.15 K throughout the experiment. The details of each of the runs in the four cases considered are presented in Tables 6.2 to 6.5. The icon for the customized RPB absorber model is shown in Figure 6.2. The RPB model icon was created using a special feature in ACM® that allows the use of different object shapes to create an icon for a customized model. This feature also allows the user to specify the position of the inlet and outlet ports on the model icon.

Table 6.2 Process input conditions for Case 1 used for RPB absorber validation (Jassim et al., 2007)

Case	Run	% wt MEA	Rotor speed	Pressure	Lean temp	Lean flow	Lean loading	Gas mole fraction			Liquid mole fraction		
		% wt	RPM	bar	K	kg/s	mol_{CO2}/mol_{MEA}	CO2	H_2O	N_2	CO_2	H_2O	MEA
1	1	56	600	1.01325	312.75	0.66	0.0772	0.0471	0.1679	0.785	0.0216	0.697	0.2814
	2	53.2	600	1.01325	293.85	0.66	0.0897	0.0460	0.169	0.785	0.0234	0.7171	0.2595
	3	56	1000	1.01325	313.25	0.66	0.0772	0.0448	0.1702	0.785	0.0216	0.697	0.2814
	4	55	1000	1.01325	294.05	0.66	0.0924	0.0445	0.1705	0.785	0.0277	0.6967	0.2756

Table 6.3 Process input conditions for Case 2 used for RPB absorber validation (Jassim et al., 2007)

Case	Run	% wt MEA	Rotor speed	Pressure	Lean temp	Lean flow	Lean loading	Gas mole fraction			Liquid mole fraction		
		% wt	RPM	bar	K	kg/s	mol_{CO2}/mol_{MEA}	CO2	H_2O	N_2	CO_2	H_2O	MEA
2	1	55	600	1.01325	312.65	0.35	0.1000	0.0443	0.1707	0.785	0.0276	0.697	0.2754
	2	56	600	1.01325	295.45	0.35	0.0955	0.0447	0.1703	0.785	0.0274	0.689	0.2836
	3	55	1000	1.01325	312.75	0.35	0.0996	0.0435	0.1715	0.785	0.0276	0.6969	0.2755
	4	57	1000	1.01325	295.75	0.35	0.0945	0.0409	0.1741	0.785	0.0277	0.6801	0.2922

Table 6.4 Process input conditions for Case 3 used for RPB absorber validation (Jassim et al., 2007)

Case	Run	% wt MEA	Rotor speed	Pressure	Lean temp	Lean flow	Lean loading	Gas mole fraction			Liquid mole fraction		
		% wt	RPM	bar	K	kg/s	mol_{CO2}/mol_{MEA}	CO2	H_2O	N_2	CO_2	H_2O	MEA
3	1	75	600	1.01325	314.15	0.66	0.0492	0.044	0.171	0.785	0.024	0.4904	0.4856
	2	77	600	1.01325	294.55	0.66	0.0389	0.0436	0.1714	0.785	0.020	0.4688	0.5112
	3	74	1000	1.01325	313.35	0.66	0.0483	0.0436	0.1715	0.785	0.0229	0.5057	0.4714
	4	75.1	1000	1.01325	293.85	0.66	0.0355	0.0429	0.1721	0.785	0.0169	0.5008	0.4823

Table 6.5 Process input conditions for Case 4 used for RPB absorber validation (Jassim et al., 2007)

Case	Run	% wt MEA	Rotor speed	Pressure	Lean temp	Lean flow	Lean loading	Gas mole fraction			Liquid mole fraction		
		% wt	RPM	bar	K	kg/s	mol_{CO_2}/mol_{MEA}	CO_2	H_2O	N_2	CO_2	H_2O	MEA
4	1	72	600	1.01325	313.95	0.35	0.0582	0.0355	0.1795	0.785	0.0263	0.5262	0.4475
	2	76	600	1.01325	295.25	0.35	0.0443	0.0438	0.1712	0.785	0.0221	0.4795	0.4984
	3	75	1000	1.01325	312.55	0.35	0.0523	0.0438	0.1712	0.785	0.0256	0.4876	0.4868
	4	78	1000	1.01325	293.75	0.35	0.0407	0.0453	0.1697	0.785	0.0215	0.4515	0.527

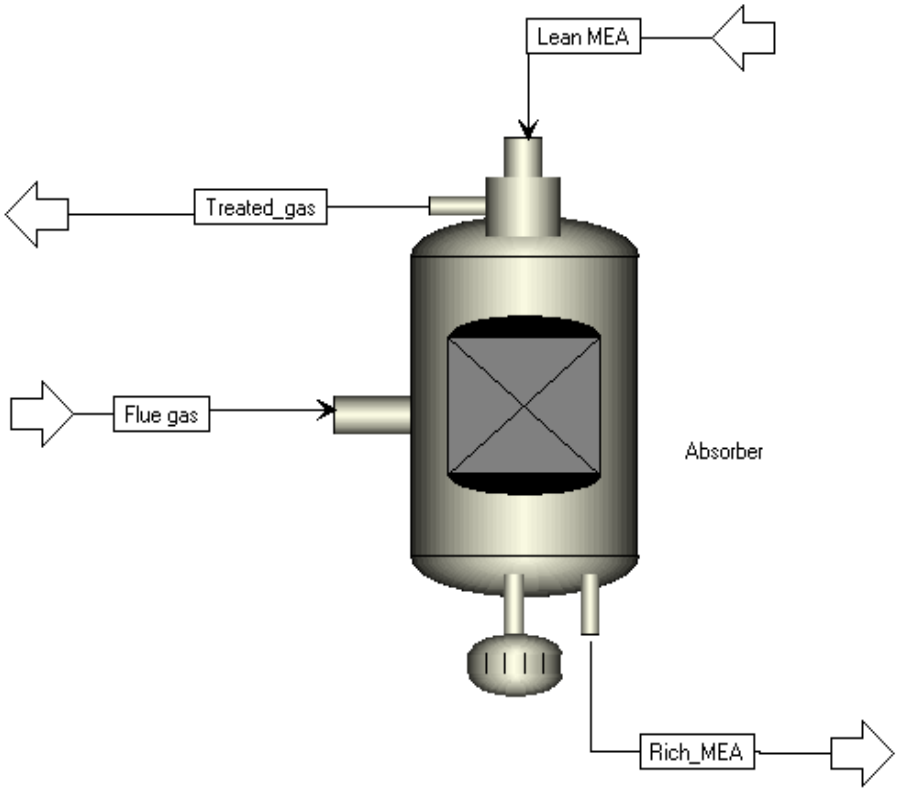

Figure 6.2 Icon for the customized RPB absorber model in ACM®

The RPB model predictions for CO_2 capture level and CO_2 rich loading were validated against experimental data for the different input conditions presented in Tables 6.2-6.5. The CO_2 capture level and the CO_2 loading are defined using Eqs. 6.1 and 6.2 respectively.

$$CO_2\ capture\ level\ (\%) = \left(\frac{y_{CO_{2,in}} - y_{CO_{2,out}}}{y_{CO_{2,in}}}\right) \times 100 \qquad 6.1$$

$$CO_2\ loading\ \left(\frac{mol_{CO_2}}{mol_{MEA}}\right) = \frac{x_{CO2} + x_{CO_3^{2-}} + x_{HCO_3^-} + x_{MEACOO^-}}{x_{MEA} + x_{MEA^+} + x_{MEACOO^-}} \qquad 6.2$$

Where $y_{CO2,in}$ is the mole fraction of CO_2 in the inlet flue gas and $y_{CO_{2,out}}$ is the mole fraction of CO_2 in the treated gas stream leaving the RPB absorber, x_i is the mole fraction of components in the liquid phase.

The model validation results showing comparisons of the model predictions to experimental data for all the runs in Cases 1 to 4 are shown in Tables 6.6 – 6.9. For all the runs, the relative error between the model predictions and experimental data is generally less than 6%. These results (Tables 6.6-6.9) showed a relative error of about 0.271-5.96% for the CO_2 capture level. The highest relative error of 5.96% was recorded in Case 3 Run 2 corresponding to an MEA concentration of 77 wt%. The model slightly over-predicted the CO_2 capture level except for Case 1 Run 1, Case 2 Run 2 and Case 4 Run 1 where the model predictions are lower than the experimental data. This could be because the Billet and Schultes (1999) correlation over-predicted the interfacial area required for mass transfer thereby resulting in more CO_2 uptake.

The model also closely predicted the rich CO_2 loading with relative errors of about 0-3.455%. These relative errors are lower than those obtained in previous studies (Borhani et al., 2018; Im et al., 2020; Oko et al., 2018) because the Gabrielsen et al. (2005) model used to calculate the liquid bulk concentration in this study gives a better prediction than the more complicated model used those studies. The more elaborate model used to predict the chemical equilibrium compositions in those studies are dependent on a high number of adjustable parameters that have to be fitted. Despite the deviations, the results show that the RPB absorber model developed in ACM® generally predicted the experimental data thereby demonstrating the accuracy of the model.

Table 6.6 Model predictions compared to experimental data for Case 1

Case	Run	CO_2 capture level (%)			Rich CO_2 loading (Mol_{CO2}/mol_{MEA})		
		Exp	Model	Relative error (%)	Exp	Model	Relative error (%)
1	1	94.90	94.64	0.271	0.0822	0.0823	0.122
	2	83.00	84.11	1.339	0.0951	0.0950	0.105
	3	95.40	99.17	3.956	0.0826	0.0826	0.00
	4	87.00	88.74	2.001	0.0955	0.0988	3.455

Table 6.7 Model predictions compared to experimental data for Case 2

Case	Run	CO_2 capture level (%)			Rich CO_2 loading (Mol_{CO2}/mol_{MEA})		
		Exp	Model	Relative error (%)	Exp	Model	Relative error (%)
2	1	87.00	89.83	3.258	0.1105	0.1100	0.452
	2	84.10	83.40	0.832	0.1044	0.1050	0.574
	3	89.90	93.60	4.202	0.1073	0.1074	0.093
	4	86.20	87.28	1.254	0.1021	0.1020	0.098

Table 6.8 Model predictions compared to experimental data for Case 3

Case	Run	CO_2 capture level (%)			Rich CO_2 loading (Mol_{CO2}/mol_{MEA})		
		Exp	Model	Relative error (%)	Exp	Model	Relative error (%)
3	1	98.20	99.21	1.030	0.0531	0.0525	1.130
	2	84.20	89.22	5.962	0.042	0.042	0
	3	97.50	98.90	1.435	0.0505	0.0515	1.980
	4	91.20	95.24	4.429	0.0402	0.04083	1.567

Table6.9 Model predictions compared to experimental data for Case 4

Case	Run	CO_2 capture level (%)			Rich CO_2 loading (Mol_{CO2}/mol_{MEA})		
		Exp	Model	Relative error (%)	Exp	Model	Relative error (%)
4	1	98.00	97.58	0.431	0.0635	0.0634	0.157
	2	84.00	86.05	2.441	0.0495	0.0496	0.202
	3	98.10	99.68	1.616	0.0586	0.0591	0.853
	4	91.0	95.65	5.111	0.0477	0.04896	2.642

6.3 Scale-up methodology and procedure for of the RPB absorber

The basic dimensions of the RPB include the inner packing radius (r_i), the outer packing radius (r_o) and the axial height (Z). These dimensions affect flooding and the CO_2 capture level in RPB. Therefore, a rigorous design approach must be adopted to determine their values when designing an RPB for a given separation task. For instance, If the height of the RPB is smaller than required, some of the liquid exiting the distributor is carried away in the gas thereby preventing them from reaching inside the RPB and resulting in flooding.

If the height of the RPB is too large, some parts of the packing remain unwetted thereby resulting in liquid maldistribution and consequently a bulkier RPB.

The scale-up of RPB from lab-scale to commercial scale is a complex and troublesome multistage task that requires adequate knowledge to avoid scale-up failures that could have dire consequences. Therefore, following the basics of RPB design presented in Agarwal et al. (2010), a rigorous iterative scale-up approach has been developed to calculate the basic dimensions of an RPB absorber in this study. The overview of the iterative approach is shown in Figure 6.3 and the details of the approach are presented later in this section.

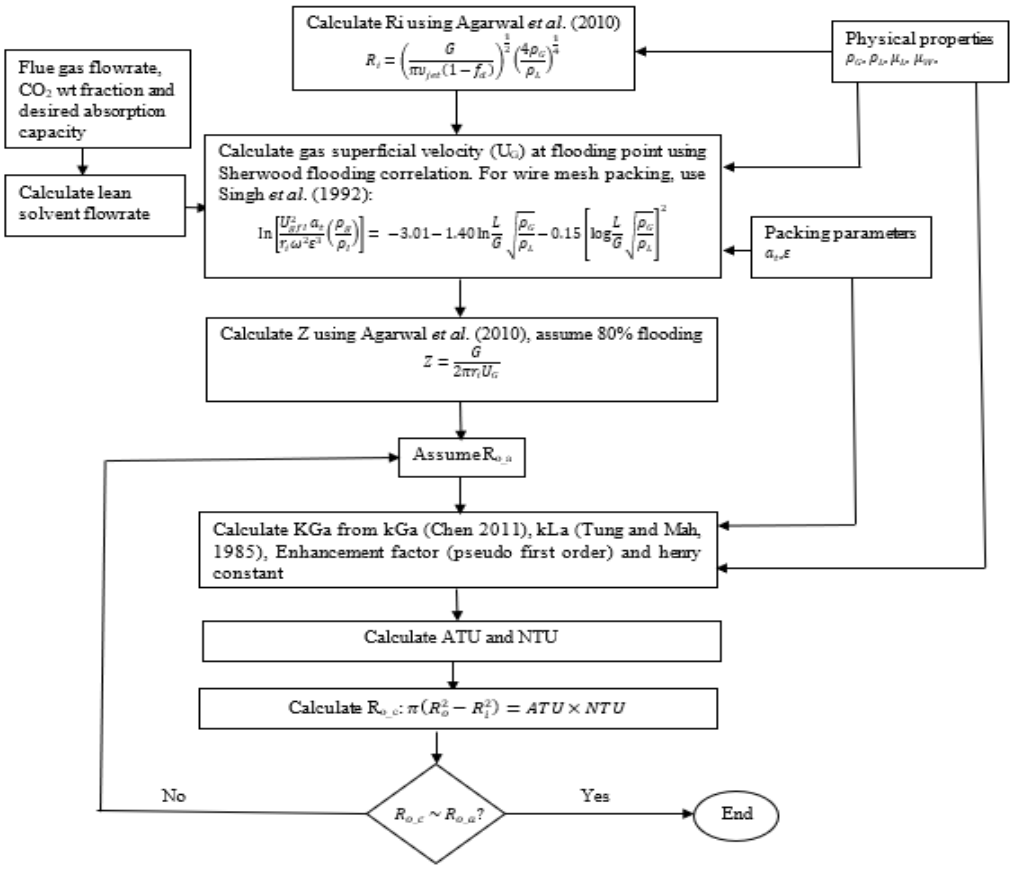

Figure 6.3 A rigorous iterative approach for RPB scale-up

6.6.1 Lean solvent flowrate estimation

To design a large-scale RPB absorber, the mass flow rate of the lean solvent that would be required must first be estimated. This is determined based on the flue gas mass flow rate,

CO_2 mass fraction in the flue gas, CO2 capture level, MEA concentration, and absorption capacity (Agbonghae et al., 2014).

$$L = \frac{Gx_{CO2}\Psi_{CO2}}{100\check{z}(\Delta\alpha)}\left[\frac{M_{MEA}}{44.009}\left(1+\frac{1-\omega_{MEA}}{\omega_{MEA}}\right)+z\alpha_{lean}\right] \qquad 6.3$$

The solvent flow rate for the large-scale RPB absorber was estimated using Eq. 6.3. This equation (Eq. 6.3) has been used by many researchers (Agbonghae et al., 2014; Luo and Wang, 2017; Otitoju et al., 2021, 2020) and is very accurate in estimating the lean solvent flow rate required for CO_2 capture.

6.6.2 RPB Inner radius estimation

The inner radius of the RPB should be selected in such a way that it can house the liquid distributor in addition to allowing gas withdrawal from the eye of the RPB without causing an excessive pressure drop. Although the inner radius of the RPB should be as small as possible for the sake of compactness, it must however not be too small. A very small inner radius could result in high exit gas velocity that could break the liquid jets coming out of the liquid distributor. To avoid this, the inner radius of the RPB should be chosen so that both the kinetic energy of the exiting gas and the kinetic energy of the liquid jet is of the same order (Agarwal et al., 2010). The inner radius of the RPB can be estimated from Eq. 6.4.

$$r_i = \left(\frac{Q_G}{\pi U_{jet}(1-f_d)}\right)^{1/2}\left(\frac{\rho_g p^{l/g}}{\rho_l}\right)^{1/4} \qquad 6.4$$

Where U_{jet} is the liquid jet velocity with a recommended value of 4 to 5 m/s. f_d is the fraction of the packing in the inner radius occupied by the liquid distributor. The value of f_d is usually between 0.25 and 0.33. $P^{l/g}$ is the ratio of the kinetic energy of the liquid to the kinetic energy of the gas with a recommended value of 4 (Agarwal et al., 2010).

6.6.3 Axial height calculations

To determine the axial height of the RPB, the gas phase superficial velocity at flooding must first be obtained. As in PB, the RPB must be operated below flooding conditions. Flooding occurs when an excessive splashing of the MEA solvent was observed in the eye of the rotor (Jassim et al., 2007). Flooding in RPB is associated with rotor speed, gas and liquid flow rates, and the design of the RPB. A representative of the flooding correlation

chart developed by Sherwood to obtain the superficial gas velocity at flooding in RPB is shown in Figure 6.4. A unique form of this correlation (Eq. 6.5) based on the functional form of the Sherwood plot was developed by Jassim et al. (2007) for RPB with expamet packing.

$$\mathrm{In}\left[\frac{U_{g,fl}^2 a_t}{r_i \omega^2 \varepsilon^3}\left(\frac{\rho_g}{\rho_l}\right)\right] = -3.01 - 1.40\, In\left(\frac{L}{G}\sqrt{\frac{\rho_g}{\rho_l}}\right) - 0.15\left[\mathrm{In}\left(\frac{L}{G}\sqrt{\frac{\rho_g}{\rho_l}}\right)\right]^2 \qquad 6.5$$

Where $U_{g,fl}$ is the gas superficial flooding velocity, ρ_g is the density of the gas phase and ρ_l is the density of the liquid phase. The rotational speed of 600 RPM used for the pilot experiment is adopted for the large-scale RPB.

Because the expamet packing used in the pilot RPB rig is adopted for large-scale RPB in this study, the gas superficial flooding velocity is calculated using Eq 6.5. Due to the higher flooding capability of RPB, it is assumed that the RPB operates at 80% to flooding, therefore:

$$U_g = 0.8\, U_{g.fl} \qquad 6.6$$

The axial height (Z) of the RPB is therefore determined using Eq 6.7.

$$Z = \frac{Q_g}{2\pi r_i U_g} \qquad 6.7$$

Where Q_g is the volumetric gas flow rate (m^3/s).

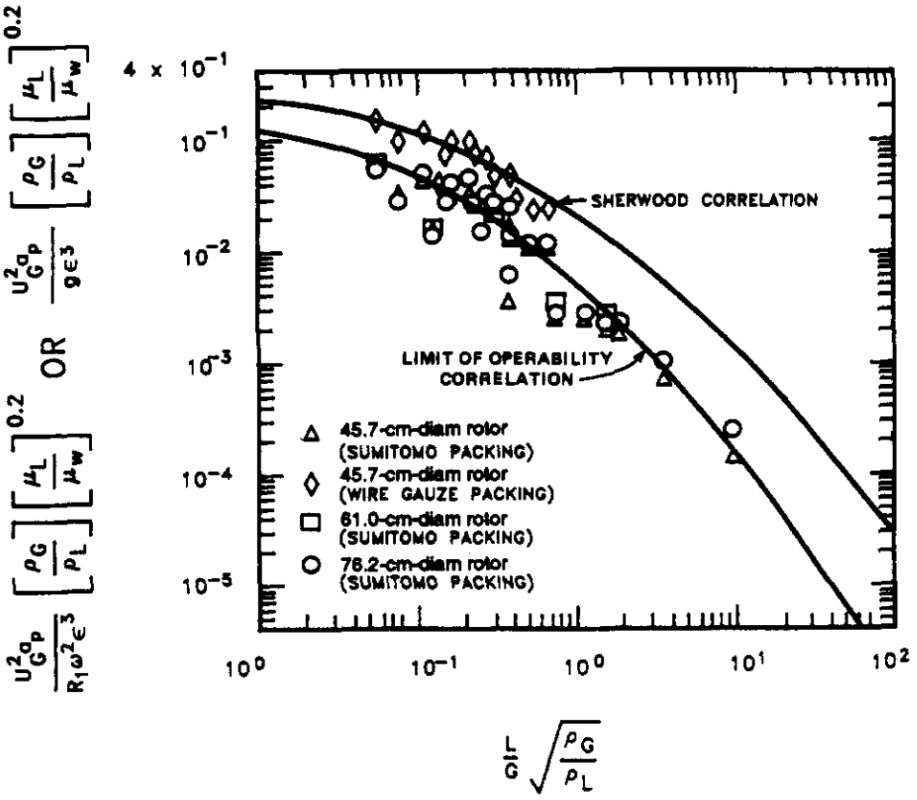

Figure 6.4 Sherwood flooding correlation chart (Singh et al., 1992)

6.6.4 Outer radius calculations

In this study, the outer radius of the RPB is calculated following an iterative procedure. For each of the cases considered, a starting value for the outer radius is assumed. Then the overall gas-phase mass transfer coefficient (K_{tot}) was obtained using Eq 5.6. The details of the parameters needed to calculate K_{tot} has been discussed in Chapter 5. The effective interfacial area (a_t) was determined using Eq. 5.18. Thereafter, the area of transfer units (ATU) and the number of transfer units (NTU) are obtained as follows:

$$ATU = \frac{F_g}{ZK_{tot}P} \tag{6.8}$$

$$NTU = \int_{y_1}^{y_2} \frac{dy}{y - y_e} \tag{6.9}$$

Where y_1 and y_2 are the mole fraction of CO2 in the inlet and outlet gas streams. y_e is the gas phase mole fraction of CO_2 in equilibrium with CO_2 concentration in the liquid. Assuming a negligible value of y_e, then NTU becomes:

$$NTU = In\frac{y_2}{y_1} \quad 6.10$$

Finally, the outer radius of the RPB is calculated thus:

$$\pi(r_o^2 - r_i^2) = ATU \times NTU \quad 6.11$$

$$r_o = \sqrt{\frac{ATU \times NTU}{\pi} + r_i^2} \quad 6.12$$

Table 6.10 Data used to calculate the dimensions of the RPB at different MEA concentrations and CO_2 loading difference of 0.18 mol_{CO2}/mol_{MEA}

Wt% MEA	L (kg/s)	ρ_l (kg/m³)	K_{tot} (mol/m².s.bar)
30	653.01	1031.93	0.0241
35	563.59	1038.25	0.0256
40	496.52	1044.49	0.0292
45	444.36	1050.64	0.0319
50	402.62	1056.7	0.0328
55	368.48	1062.64	0.0336
60	340.03	1068.43	0.0347
65	315.96	1074	0.0367
70	295.32	1079.37	0.0382
75	277.44	1084.38	0.0396
80	261.79	1088.94	0.0442
85	247.98	1092.86	0.0534
Q_g (m³/s)	325.90	ε	0.76
G (kg/s)	356.0	a_{sap} (m²/m³)	2132
F_g (mo/s)	12.6532	Pressure (bar)	1.01325
v_{jet} (m/s)	4.50	ω (rad/s)	62.83

6.4 Scale-up results for the RPB absorber used for PCC for a 250 MW_e CCGT power plant

6.4.1 Lean solvent flow rate

The lean solvent calculations are based on 90% CO_2 capture from flue gas from a 250 MWe CCGT Power Plant using MEA solvent. The specification for the flue gas from the power

plant is the same as the one used in Chapters 3 and 4 for the large-scale CO_2 capture process with MEA and PZ in PBs. The solvent flow rate is calculated for MEA concentrations from 30wt% MEA - 85wt% MEA at absorption capacities (i.e. the difference between rich loading and lean loading) of 0.1, 0.18 and 0.25 mol_{CO_2}/mol_{MEA} respectively.

From the results (See Figure 6.5), the absorption capacity (delta alpha ($\Delta\alpha$)) and MEA concentration are very influential in determining the solvent flow rate. As the MEA concentration increases from 30 – 85 wt% and the absorption capacity increases from 0.1-0.25 mol/mol, the lean solvent flow rate reduces from about 1175 kg/s to about 176 kg/s indicating an 85% reduction in L/G ratio from about 3.3 kg/kg to 0.49 kg/kg.

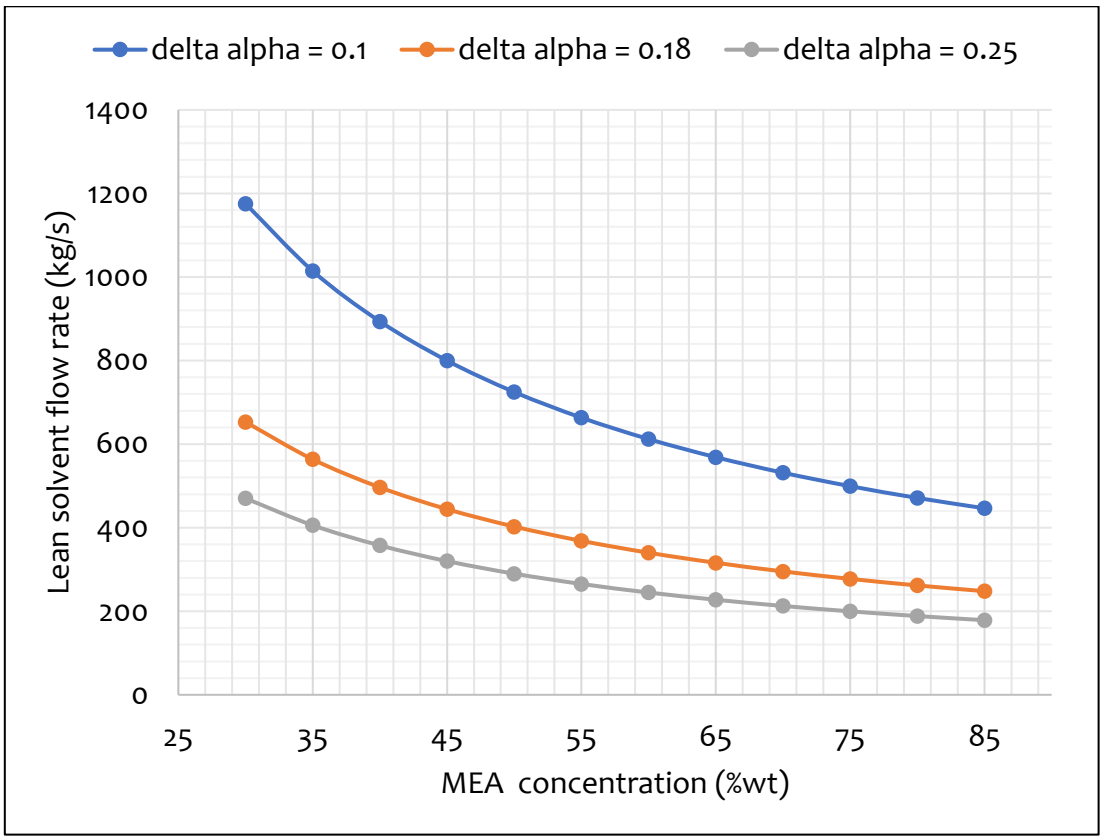

Figure 6.5 Lean solvent flow rate at different MEA concentrations and absorption capacity

The solvent flow rates obtained at $\Delta\alpha$ = 0.18 mol_{CO_2}/mol_{MEA} are adopted in this study to calculate the dimensions of the large-scale RPB absorber. This value (0.18 mol_{CO_2}/mol_{MEA}) is a conservative value considering that the presence of centrifugal acceleration in the RPB will enhance CO2 uptake that could lead to a higher value of $\Delta\alpha$. At $\Delta\alpha$=0.1 mol_{CO_2}/mol_{MEA},

the lean solvent flow rates are so large that if they are adopted as a benchmark the RPB size-reduction expectation may not be met.

6.4.2 Inner radius and axial height of the RPB

The liquid jet velocity is chosen between values between 4-5 m/s is recommended for the liquid jet velocity; higher values may result in the jet splashing back when the hit the packing (Agarwal *et al.*, 2010). The physical properties, namely ρ_G and ρ_L, have been estimated using an initial lean loading of 0.2 mol_{CO_2}/mol_{MEA}, 40°C temperature and 1.01 bar pressure. The results in Figure 6.6, show the variation of the inner radius (r_i) and the axial height (Z) with the MEA concentration. The values of r_i only change slightly with MEA concentration. For instance, an MEA increase from 30 wt% to 85 wt% only results in a 1.4% reduction in the inner radius for the RPB.

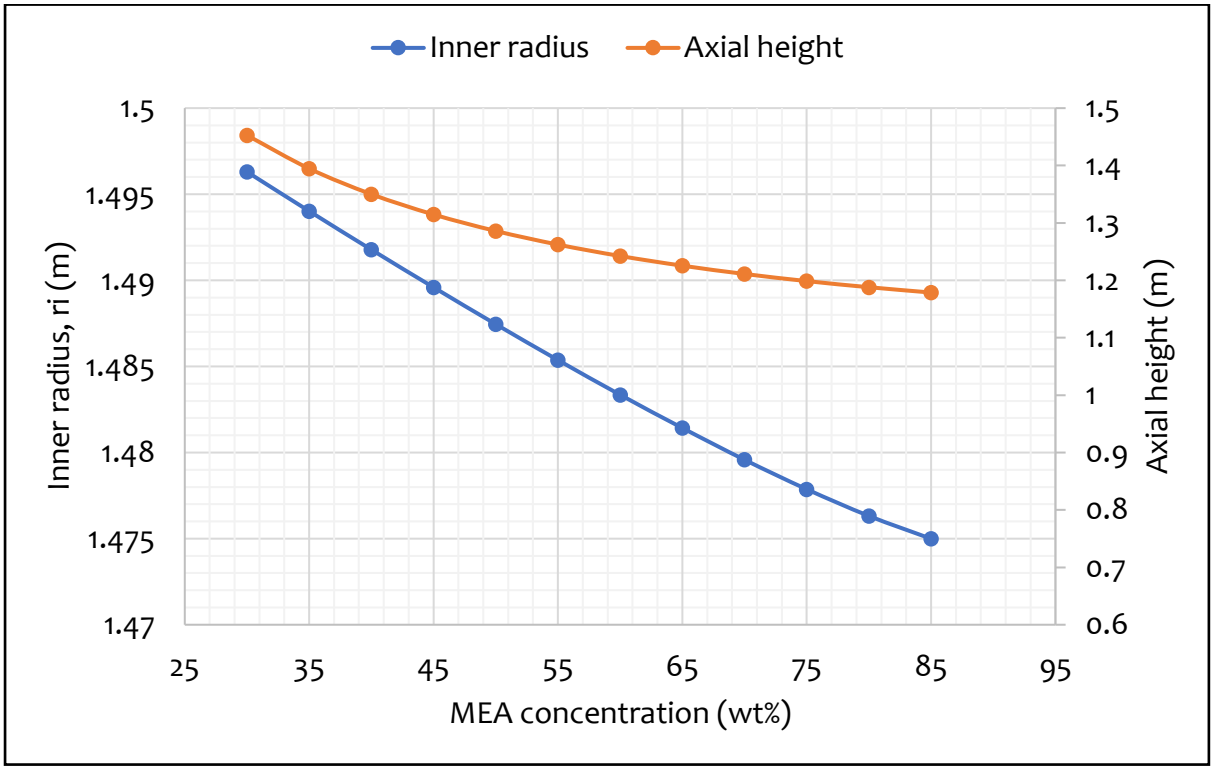

Figure 6.6 Variation of Inner radius and axial height of the RPB with MEA concentration

The reason for this minimal change in the values of r_i despite the increase in MEA concentration is that all the terms in Eq. 6.4 used to calculate r_i are constants except for the density of the MEA solvent which changed by about 5.6% from 1031.93 kg/m³ at 30 wt% MEA to 1092.86 kg/m³ at 85 wt% MEA.

The effect of the change in MEA concentration is more profound on the axial height of the RPB than it was on the inner radius. As the MEA concentration increased from 30 wt% to 85 wt%, the axial height decreased by 19% from 1.45 m to1.17 m. This is about 17% more than the reduction achieved in the inner radius.

6.4.3 Outer radius of the RPB

The variation of the outer radius of the rotor with the MEA concentration is shown in Figure 6.7. The reduction in the outer radius as the MEA concentration increases is due to the reduction in the ATU and r_i of the RPB. The reduction in the ATU is influenced by the axial height of the RPB and the $K_{tot.}$ As seen from Table 6.10 and Figure6.6, these variables both reduce with an increase in MEA concentration thereby resulting in lower ATU and consequently lower values of r_o.

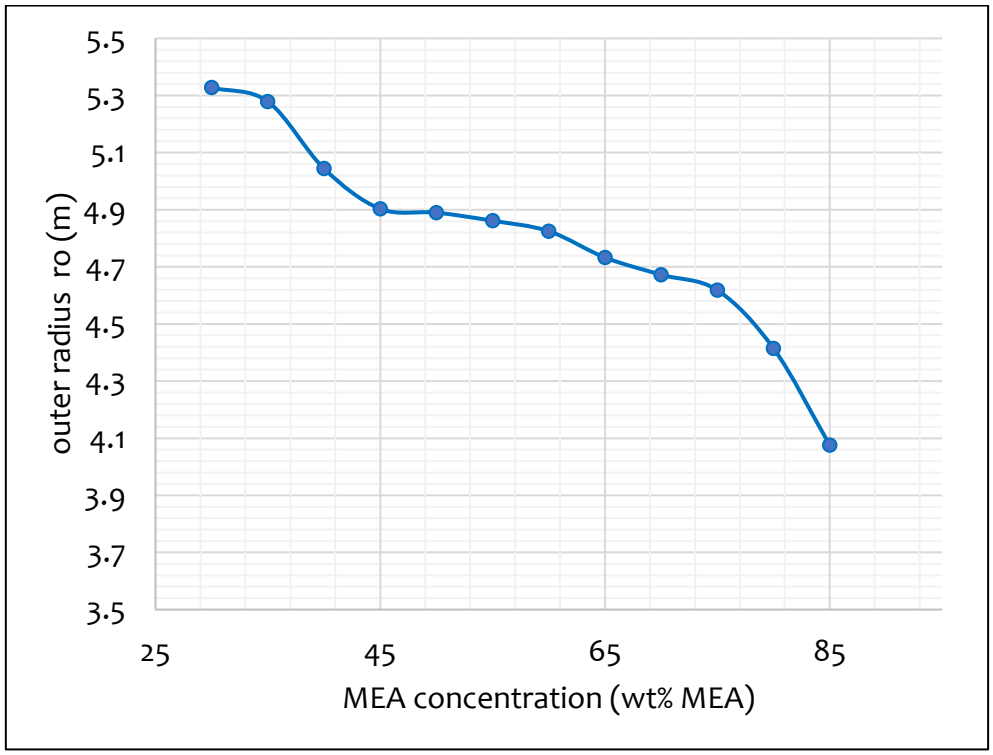

Figure 6.7 Initial outer radius of the RPB absorber for different MEA concentrations

Since there is no study on the design of RPB absorbers for large-scale CO2 capture before this, there is no known report on what the maximum allowable outer radius should be. For large-scale PB absorbers, a maximum diameter of 18 m is recommended (Agbonghae et

al., 2014; IEA-GHG, 2006; Otitoju et al., 2020). This value would be too high for RPB due to the huge rotor requirement and the limitation imposed by the moving mechanical parts in RPB. A conservative maximum value of 10 m has been chosen for the outer diameter of the RPB designed in this study. Also, care has been taken to ensure that the ratio of the axial height to the outer diameter of the RPB does not exceed the recommended value of 0.85 (Gudena et al., 2013).

6.5 Technical assessment of the large-scale RPB absorber for solvent-based PCC process

The analysis of the CO_2 capture process characteristics in RPB absorbers has been carried out in previous studies (Borhani et al., 2018; Im et al., 2020; Joel et al., 2014; Kang et al., 2014; Oko et al., 2019). In those analyses, the model response to a change in certain variables was examined. Conclusions from some of these studies have highlighted the size-reduction benefits of the RPB. However, these analyses (except Im et al. (2020) that used different RPB dimensions) were performed using a tiny RPB absorber of inner and outer diameters of 0.156 m and 0.398 m and axial height of 0.025 m. The flue gas and solvent flow rates in those studies were limited to 0.022 kg/s and 0.66 kg/s. In addition to this, the lean solvent CO_2 loadings (0.0355-0.100 mol_{CO2}/mol_{MEA}), rich solvent CO_2 loadings (0.0420-0.1105 mol_{CO2}/mol_{MEA}) and L/G ratios (16-30 kg/kg) at which some of these analyses were performed are economically impractical for the CO_2 capture process. Therefore, the process analysis in this study has employed practicable conditions for the CO_2 capture process. Also, considering that at a large scale, the flue gas and solvent flow rates will be hundreds to thousands of times these values, this could lead to a change in process and hydrodynamic behaviour of the RPB absorber. Therefore, it is imperative to provide process analysis at a large scale to obtain insights on the possible requirements of the CO_2 capture in large-scale RPB absorbers.

In this section, the results obtained from section 6.4 are used to simulate a large-scale RPB absorber which is then used to analyze the response of the large-scale CO_2 capture process to change in operating variables. The operating conditions and the specifications used to simulate the large-scale RPB absorber are shown in Table 6.11.

Table 6.11 Operating conditions and specifications used for the simulation of the large-scale RPB absorber

Flue gas	
Flow rate (kg/s)	356
Temperature (°C)	40
Molar compositions	
CO_2	0.0492256
H_2O	0.085029
N2	0.865745
Lean solvent	
Flow rate (kg/s)	250-440
Temperature (°C)	40
CO_2 loading (mol_{CO2}/mol_{MEA})	0.16-0.30
MEA concentration (wt%)	30, 55, 65, 75
RPB absorber dimensions and specifications	
Pressure (Bar)	1.01325
Rotor speed (RPM)	400-1200
Inner diameter (m)	2.98
Outer diameter (m)	8.00
Axial height (m)	0.65

Contrary to previous studies (Borhani et al., 2018; Joel et al., 2014) where the analyses were performed with a lean solvent temperature of about 20 °C, the analyses in this study have been performed at a lean solvent temperature of 40 °C. This is because findings from those studies indicated that the CO_2 capture levels are generally lower than the required 90% at that temperature. Therefore, operating at that temperature means high energy consumption for solvent cooling before entering the RPB absorber and a lower CO_2 capture level in the RPB absorber. Therefore, based on our experience on CO_2 capture with MEA in PB, the lean solvent temperature is fixed at 40 °C in this work. This would enhance the mass transfer flux and reduce water vaporization of the capture process.

6.5.1 Lean solvent CO_2 loading

The CO2 loading of the MEA solvent entering the RPB absorber affects the CO_2 capture level. In an integrated CO_2 capture process, the CO_2 loading of the lean solvent depends on the regeneration performance in the stripper. In addition to this, it affects the amount of energy consumed for solvent regeneration in the stripper. Therefore, it has a direct influence on the performance of both the absorber (in terms of the CO_2 capture level and

the rich CO_2 loading) and the stripper (in terms of regeneration energy consumption). However, despite its importance, the effect of change in lean solvent CO_2 loading on CO_2 capture level and rich solvent CO_2 loading in the RPB absorber has not been examined. This analysis will provide the first insights on this.

The lean CO_2 loading was varied from 0.16-0.3 mol_{CO2}/mol_{MEA} to study its impact on the CO_2 capture level at MEA concentrations of 30, 55 65 and 75 wt%. The rotor speed of 600 RPM was used for this analysis. The influence of lean CO_2 loading on the CO_2 capture level at different MEA concentrations is shown in Figure 6.8. The results show that the CO_2 capture level decreases with an increase in lean CO_2 loading for all MEA concentrations. At all lean CO_2 loadings, the highest CO_2 capture levels are achieved at the MEA concentration of 75 wt% and the lowest CO_2 capture levels are achieved at an MEA concentration of 30 wt%. Also, the decrease in the CO_2 capture level as the lean loading increases from 0.16-0.30 mol_{CO2}/mol_{MEA} is more profound at lower MEA concentrations (30 and 55 wt%) than at higher MEA concentrations (65 and 75 wt%).

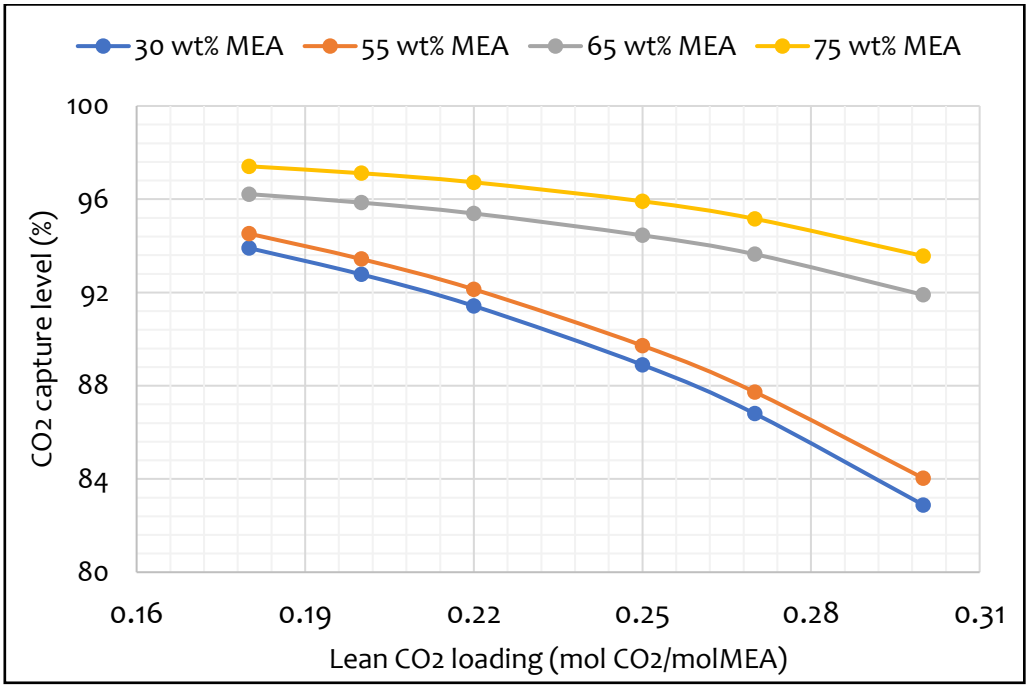

Figure 6.8 Influence of lean CO_2 loading on CO_2 capture level at different MEA concentrations

As the CO_2 loading was increased from 0.16 to 0.3 mol_{CO2}/mol_{MEA}, 12 and 10 points drop in CO_2 capture levels are observed at 30 and 55 wt % MEA concentrations as against 4 and 3

points drop in capture CO_2 levels observed at 65 and 75 wt% concentrations. The reason for this is that as the CO_2 loading in the lean solvent increases, the amount of free MEA available to absorb CO_2 decreases. And as the free MEA decreases, the CO_2 uptake capability of the lean solvent also decreases. However, these decreases are more significant for the 30 and 50 wt% MEA concentrations than for the 65 and 75 wt% MEA concentrations. Although the CO_2 capture levels are generally higher (above 90%) at CO_2 loadings below 0.22 mol_{CO_2}/mol_{MEA}, however, operating at these lean loadings mean higher energy would be required to strip the CO_2 in the solvent down to these levels. At higher lean loadings (above 0.27 mol_{CO_2}/mol_{MEA}) the lean solvent becomes more saturated with CO_2 thereby resulting in a higher solvent rate being needed to achieve the required CO_2 capture level. This increase in lean solvent rate could lead to an increase in RPB size and consequently, an increase in the capital and operating costs of the process. After careful observations of the results obtained from this analysis, a lean CO_2 loading of 0.25 mol_{CO_2}/mol_{MEA} is chosen for the rest of the analysis carried out in this work.

The effects of the change in lean CO_2 loadings on the rich CO_2 loadings are shown in Figure 6.9. In contrast to the results in Figure 6.8, the rich CO_2 loading increases with lean CO_2 loadings as the MEA concentration increases from 30-75 wt%. The increase in the rich loadings is however not an indication of better absorption performance.

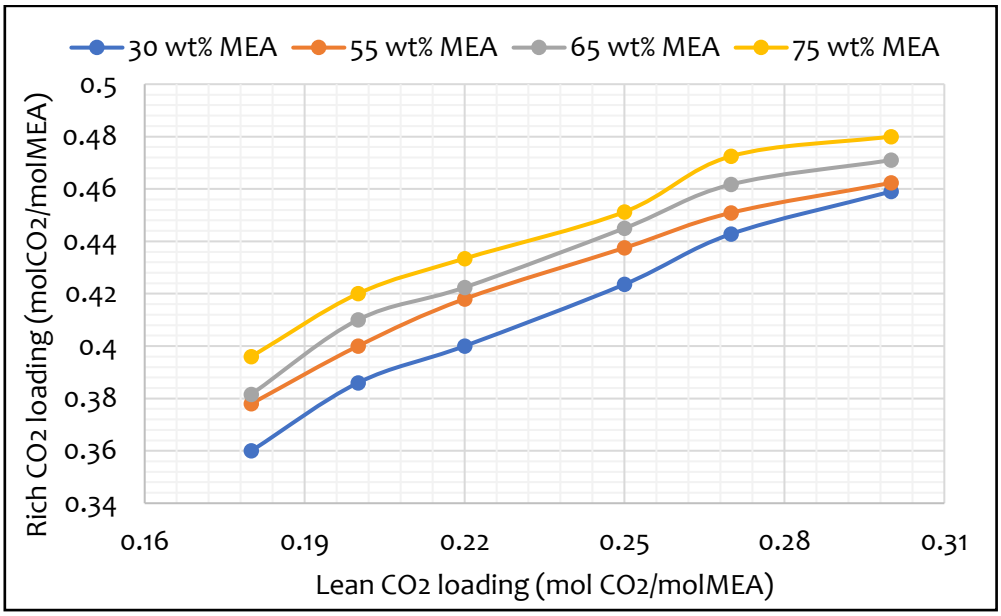

Figure 6.9 Influence of lean CO_2 loading on rich CO_2 loading at different MEA concentrations

Although the rich CO_2 loadings obtained at low lean loadings are smaller, they resulted in higher absorption capacities (difference between the rich and lean loadings) compared to those obtained at higher lean loadings. This is responsible for the higher CO_2 capture levels achieved at low CO_2 loadings.

6.5.2 Different MEA concentrations

Insights on the effects of MEA concentrations on the capture performance of an RPB absorber has been provided for pilot scale RPB at MEA concentrations of 55 to 75 wt% (Borhani et al., 2018; Im et al., 2020; Joel et al., 2014). For the large-scale RPB absorber in this study, the analysis of the effect of MEA concentration on the CO_2 capture level is carried out at MEA concentrations of 55, 65 and 75 wt%. This is because the developed RPB model was only validated with MEA concentrations within this range. Two rotor speeds of 600 and 1000 RPM and lean solvent flow of 350 kg/s are used. The results of this analysis are shown in Figure 6.10. By increasing the MEA concentration from 55 to 75 wt%, the CO_2 capture level increased significantly for 600 RPM and slightly for 1000 RPM. The MEA concentrations have lesser effects on the CO_2 capture level at 1000 RPM. Therefore, it will be less economical to operate the RPB at this rotor speed.

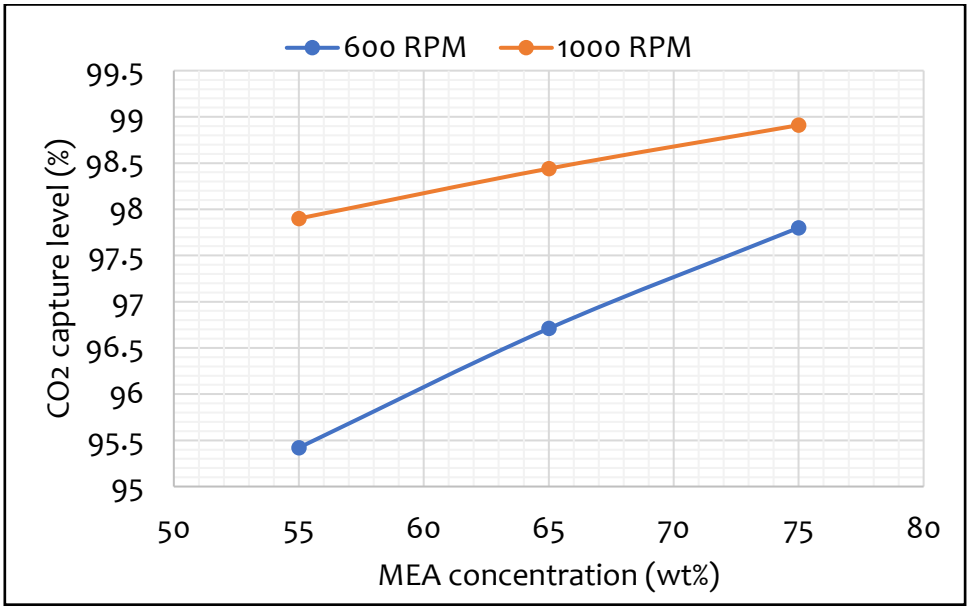

Figure 6.10 Influence of MEA concentrations on CO_2 capture level at two rotor speeds

The CO_2 capture level increases as the MEA concentration increased from 55 to 75 wt%. For both rotor speeds (600 and 1000 RPM) the CO_2 capture levels are highest at the MEA concentration of 75 wt%. This is because, at higher MEA concentrations, the rate of reaction is enhanced since the rate coefficient of the pseudo-first-order reaction is a function of MEA concentrations (Freguia and Rochelle, 2003; Joel et al., 2014). The implication of this is that if the CO_2 capture level is fixed at a particular value, it will require a lower lean solvent flowrate to capture the same amount of CO_2 at 75 wt% MEA compared to at 55 and 65 wt% MEA. This reduction in lean solvent flow rate could lead to a reduction in the amount of energy consumed for solvent regeneration. Although higher MEA concentrations could lead to higher CO_2 capture levels and lower energy consumption, they have a greater tendency for equipment corrosion. Therefore, care must be taken to select an MEA concentration that fulfils the basic requirement of the best CO_2 capture level with less equipment corrosion.

6.5.3 Rotor speed

Existing studies have evaluated the effect of rotor speed on the CO_2 capture level for pilot-scale RPB absorbers. Findings from those studies indicated that the rotor speed improves the mass and heat transfer performance of the RPB absorber. Hence, the impact of rotor speed on CO_2 capture is investigated at a rotor speed of 400–1200 RPM at MEA concentrations of 55, 65 and 75 wt%. The lean solvent flow rate is maintained at 350 kg/s. The results of this analysis are shown in Figure 6.11.

There is a noticeable change in the CO_2 capture level for all MEA concentrations when the rotor speed is increased from 400 RPM to 600 RPM. Beyond 600 RPM, there is very little change in the capture level for all MEA concentrations. Rotor speed enhances mass transfer due to its contribution to the interfacial area. However, this contribution is more significant at 400 and 600 RPM than at higher rotor speeds. For instance, when the rotor speed was increased from 400 RPM to 600 RPM, the interfacial area for mass transfer increased by 6% from 1361.4 m^2/m^3 to 1446.95 m^2/m^3. The effect of this is depicted by the sharp increase in capture level between 400 and 600 RPM. A further increase in rotor speed to 800, 1000 and 1200 RPMs only resulted in a 1.3%, 0.99% and 0.82% increase in interfacial area. This decrease in the percentage increase in the interfacial area as the rotor speed is increased beyond 600 RPM is responsible for the slow increase in CO_2 capture

level observed at these rotor speeds. Therefore, operating at rotor speed above 600 RPM is less economical as this will mean higher rotating energy consumptions for very little change in CO_2 capture level.

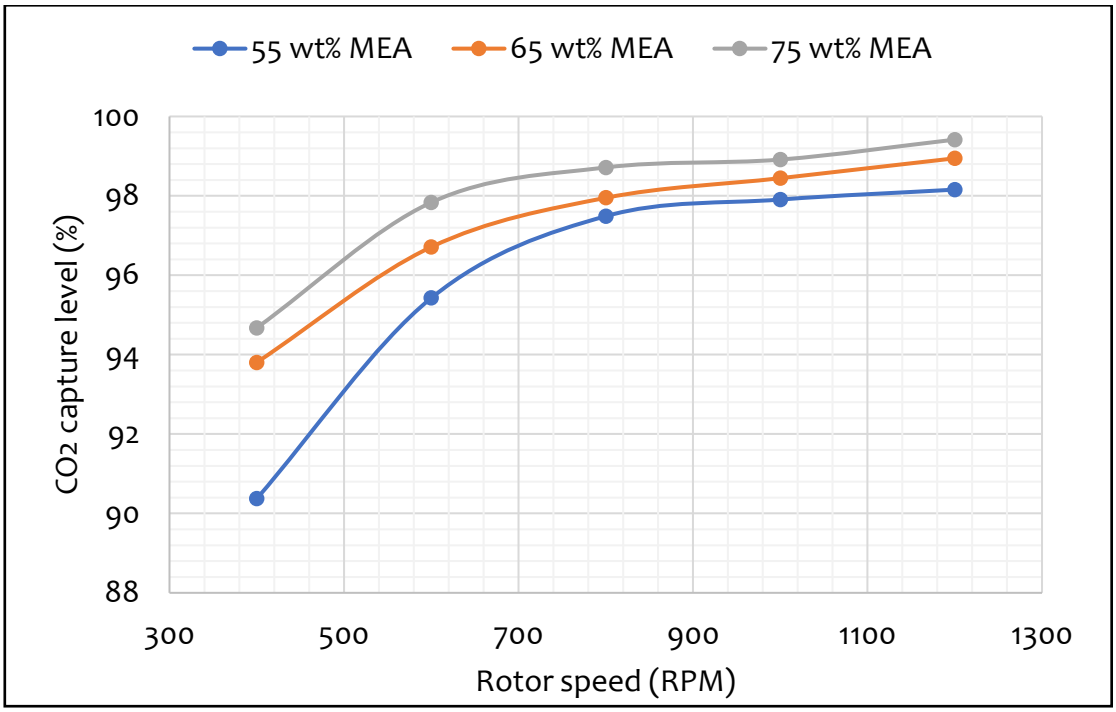

Figure 6.11 Influence of rotor speed on CO_2 capture level at different MEA concentrations

6.5.4 Lean solvent flow rate

For this analysis, the lean solvent is varied from 260 to 440 kg/s at a rotor speed of 600 RPM. This range is chosen to cover the range of lean solvent flow rates estimated for MEA concentrations of 55, 65 and 75 in Table 6.10. In the pilot-plant experiments conducted by Jassim et al. (2007) the L/G ratios were in the range of 16-30. Subsequent studies have adopted these or similar L/Gs in their work. These L/G ratios are too high, impractical, and will lead to a very large amount of solvent being used in the CO_2 capture process. This could lead to flooding issues in the RPB absorber. In addition to this, a lot of energy will be required to regenerate the solvent which will add to the total energy consumption of the process. Hence, process analysis carried out at those L/G ratios may not offer the right insight into how the lean solvent flow rate variation affects the capture performance of the RPB absorber.

Since the CO_2 composition in the flue gas used in the experiment by Jassim is typical of flue gas from a gas-fired power plant. Studies conducted with flue gas of similar CO_2 composition in PB using MEA as solvent showed an L/G ratio of 0.69-2.68 (Agbonghae et al., 2014; Canepa et al., 2013; Otitoju et al., 2020). The solvent flow rate range is chosen for analysis in the work results in L/G ratio of 0.73-1.24 which are within the range observed in previous studies of CO_2 capture with MEA in PB.

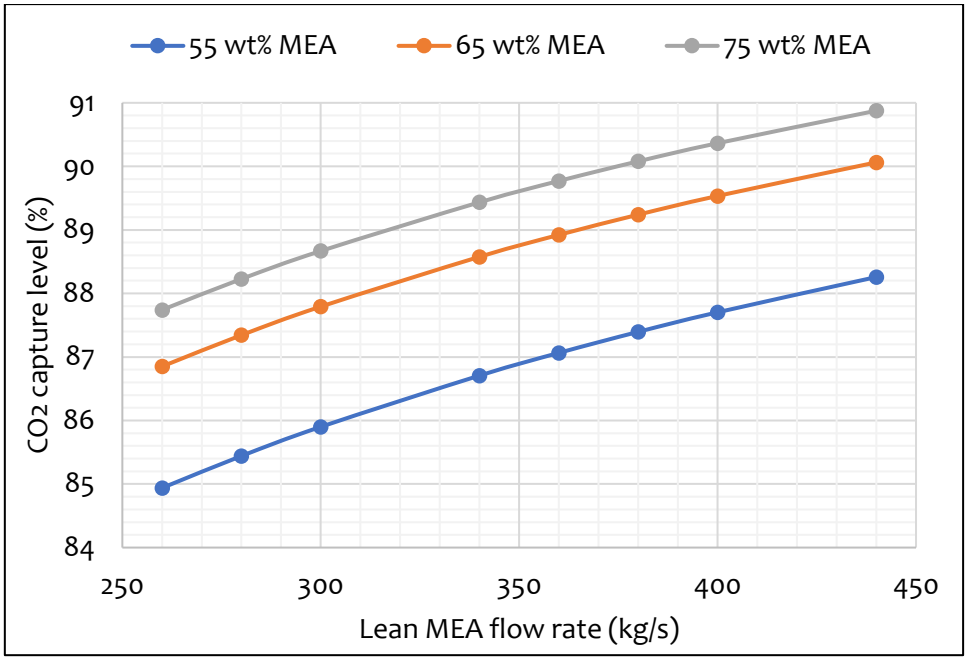

Figure 6.12 Influence of lean MEA flow on CO_2 capture level at different MEA concentration

The results of the effect of the lean solvent variation on CO2 capture level are shown in Figure 6.12. The CO2 capture level increased as the lean solvent increased for all MEA concentrations. The highest CO2 capture level was achieved at MEA concentrations of 75 wt%. This is because as the lean flow rate increases, the mass transfer and chemical reactions in the system are enhanced. At 55 wt%, the CO_2 captures are generally below 90%. Upon increasing to 65 and 75 wt%, the capture levels get to above 90%. In previous studies (Borhani et al., 2018; Joel et al., 2014), the CO_2 capture level at these conditions is usually close to 100%. The reason for this is the high ratio of the lean solvent to flue gas used. The lean solvent flow rates chosen in this study have resulted in more realistic L/G ratios and more practicable capture levels.

6.5.5 Energy consumption

The energy consumed by the rotor to rotate the RPB absorber in the CO_2 capture process needs to be estimated. This is additional parasitic energy for the process. When combined with the regeneration energy, it could lead to a higher energy consumption per tonnes of CO_2 captured in RPB than in PB. The power consumptions of the rotor are estimated at a rotor speed of 400, 600, 800 and 1000 RPMs. At each rotor speed, the power consumptions are calculated at MEA concentrations of 55, 65 and 75 wt%. The results of how the power consumption varied with MEA concentration at different rotor speeds are shown in Figure 6.13.

Generally, the power consumption increases as the rotor speed increases for all MEA concentrations. There is a minimal increase in power consumption as the rotor speed was increased from 400 to 600 RPM and a significant increase in power consumption as the rotor speed is increased from 600 to 800 and 1000 RPM respectively. Results suggested that it will be more economical to operate the RPB at a lower rotor speed (400 and 600 RPM) than to operate at a higher rotor speed.

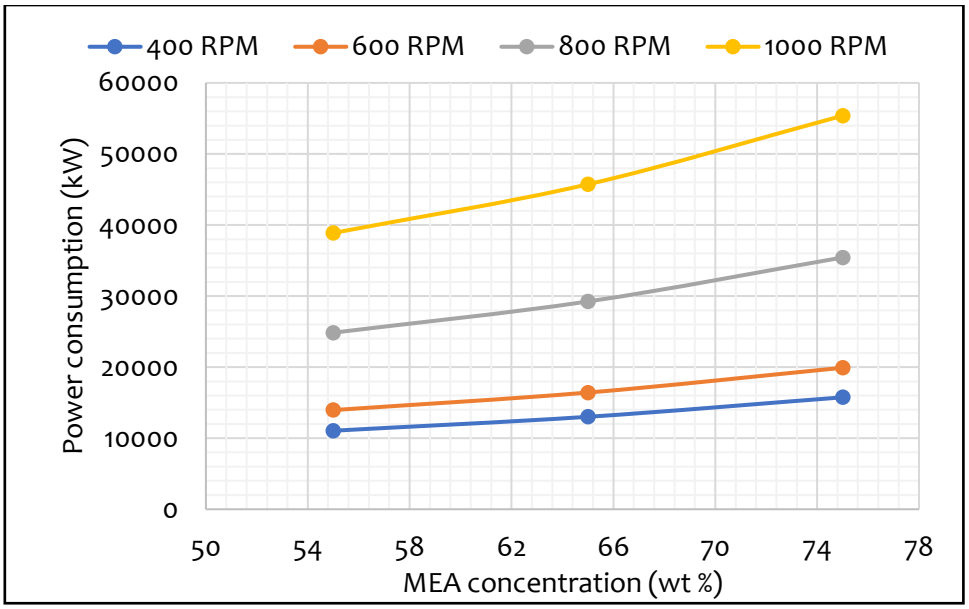

Figure 6.13 power consumption at different MEA concentrations

6.6 Economic assessment of the large-scale RPB absorber for solvent-based PCC process

The economic assessments of the RPB absorber designed in this thesis are provided in this section. The economic assessment is based on the CAPEX of the large-scale RPB absorber.

The results from the technical assessments carried out in section 6.5 show that the large scale-RPB performed best with the 75 wt% MEA. This is in agreement with the findings in earlier pilot-scale analyses (Im et al., 2020; Joel et al., 2014; Luo et al., 2021). However, the power consumption analysis in Figure 6.13 revealed that an enormous amount of power (11-55 MW) would be required to drive the rotor if the RPB is operated at a rotor speed of 400- 1000 rpm. Because of this, the economic analysis was performed with a rotor speed of 100 rpm. This reduced the rotor energy consumption to 0.78 MW. The details used in the economic assessment of the RPB absorber are shown in Table 6.12.

Table 6.12 Specification for the RPB absorber used for economic assessment

Parameters	value
MEA concentration (wt%)	75
Solvent flow rate (kg/s)	280
Capture level (%)	90
Rotor speed (rpm)	100
r_i (m)	1.48
r_o (m)	4.50
Z (m)	1.20

6.6.1 The CAPEX for the RPB absorber

There is no reported study on the costing of RPB for solvent-based PCC process, also there are limited data and experience on how to determine the capital expenditure of RPB used for solvent-based PCC process. Sudhoff et al. (2015) provided costing correlations for an RPB used for distillation. Earlier, Gudena et al. (2013) briefly described the costing of an RPB used for bioethanol recovery and purification. Based on these two studies, the CAPEX of the RPB generally consists of three parts which are the rotor cost, the motor cost and the drive cost. The rotor cost includes the cost of packings, shafts, liquid distributors and casing. The drive cost includes the cost of drives, bearings and other rotating parts. Thus the CAPEX of the RPB absorber was estimated from the individual parts using the expression in Eq 6.23 (Sudhoff et al., 2015).

$$\mathrm{CAPEX} = \left(\mathrm{C}^{\mathrm{rotor}} + \mathrm{C}^{\mathrm{motor}} + \mathrm{C}^{\mathrm{drive}}\right) \times \mathrm{C}^{\mathrm{tax}} \qquad 6.23$$

Where C^{rotor} is the rotor cost and included the cost of packing, shaft, liquid distributor as well as casing. It was estimated using the expression in Eq 6.24.

$$\mathrm{C}^{\mathrm{rotor}} = \mathrm{C}_{\mathrm{FOB}}^{\mathrm{rotor}}\left(1 + \mathrm{C}_{\mathrm{L+M}}^{\mathrm{rotor}}\ \mathrm{C}_{\mathrm{L/M}}^{\mathrm{rotor}}\right) \times \frac{\mathrm{C}^{\mathrm{CEPCI}}}{1000} \qquad 6.24$$

C^{motor} is the motor cost. It was estimated using the expression in Eq 6.25.

$$\mathrm{C}^{\mathrm{motor}} = \mathrm{C}_{\mathrm{FOB}}^{\mathrm{motor}}\left(1 + \mathrm{C}_{\mathrm{L+M}}^{\mathrm{motor}}\ \mathrm{C}_{\mathrm{L/M}}^{\mathrm{motor}}\right) \times \frac{\mathrm{C}^{\mathrm{CEPCI}}}{1000} \qquad 6.25$$

C^{drive} is the purchasing cost of the drives and bearings. It was estimated using the expression in Eq 6.26.

$$\mathrm{C}^{\mathrm{drive}} = \mathrm{C}_{\mathrm{FOB}}^{\mathrm{drive}}\left(1 + \mathrm{C}_{\mathrm{L+M}}^{\mathrm{drive}}\ \mathrm{C}_{\mathrm{L/M}}^{\mathrm{drive}}\right) \times \frac{\mathrm{C}^{\mathrm{CEPCI}}}{1000} \qquad 6.26$$

C^{tax} is the added tax on the cost of materials. The terms $\mathrm{C}_{\mathrm{FOB}}^{\mathrm{rotor}}$, $\mathrm{C}_{\mathrm{FOB}}^{\mathrm{motor}}$, and $\mathrm{C}_{\mathrm{FOB}}^{\mathrm{drive}}$ in Eqs 6.24 – 6.26 denote the free-on-board (FOB) cost of the rotor, motor and drive. It is the cost of materials and construction for each of these items. They were calculated with the expressions in Eqs 6.27 – 6.29.

$$\mathrm{C}_{\mathrm{FOB}}^{\mathrm{rotor}} = C_{ref}^{rotor} \times \left(\frac{V^{\dot{R}PB}}{V_{ref}^{\dot{R}PB}}\right)^{n^{rotor}} \qquad 6.27$$

V^{RPB} and V_{ref}^{RPB} denote the RPB liquid capacity and reference liquid capacity of the RPB. C_{ref}^{rotor} is the reference investment cost for the rotor and n^{rotor} is actual to reference scaling factor for the rotor.

$$\mathrm{C}_{\mathrm{FOB}}^{\mathrm{motor}} = C_{ref}^{motor} \times \left(\frac{P^{motor}}{P_{ref}^{motor}}\right)^{n^{motor}} \times C^{RS} \times C^{en} \times C^{al} \qquad 6.28$$

C_{ref}^{motor} is the reference investment cost for the motor, C^{RS} is the higher rotational speed adds cost, C^{en} denotes the fan and motor enclosure adds cost and C^{al} is the alloys adds cost, and n^{motor} is actual to reference scaling factor for the motor.

$$\mathrm{C}_{\mathrm{FOB}}^{\mathrm{drive}} = C_{ref}^{drive} \times \left(\frac{P^{motor} \times C_{trans}^{0.5}}{P_{ref}^{drive}}\right)^{n^{drive}} C^{al} \qquad 6.29$$

C_{ref}^{drive} is the reference investment cost for the drive, P_{ref}^{motor} refers to the motor reference electrical power and P_{ref}^{drive} refers to the drive reference electrical power. C_{trans} represents the engine transmission to drive ratio adds cost and n^{drive} is actual to reference scaling factor for the drive. The description and values of the terms in Eq. 6.23-6.29 are presented in Table 6.13

Table 6.13 Values and descriptions of the terms in Eqs 6.23-6.38 (Sudhoff et al., 2015)

Factor	Unit	Definition	Value
C^{tax}	-	Added tax on costs of material	1.19
C_{L+M}^{motor}	-	Adds labour and material costs for motor, drive and rotor	1.36
C_{L+M}^{drive}	-		1.50
C_{L+M}^{rotor}	-		1.70
$C_{L/M}^{motor}$	-	Minimizes the addition of labour costs, if a special alloy is considered in C^{al}	0.58
$C_{L/M}^{drive}$	-		0.20
$C_{L/M}^{rotor}$	-		1.00
C^{CEPCI}	-	Cost degression based on the Chemical Engineering Plant Cost Index	585.70
C_{ref}^{motor}	$	The reference value for investment costs for the motor, drive and rotor	19000
C_{ref}^{drive}	$		5300
C_{ref}^{rotor}	$		220000
P_{ref}^{motor}	kW	The reference value for electrical power of the motor and drive	75.00
P_{ref}^{drive}	kW		180
V_{ref}^{RPB}	L/s	The reference value for the liquid capacity of the RPB	2.20
n^{motor}	-	Scaling factor of the actual to the reference condition	1.10
n^{drive}	-		1.90
n^{rotor}	-		0.38
C^{RS}	-	Adds costs for higher rotational speed	1.30
C^{en}	-	Adds costs for fan and enclosure of motor	1.00
C^{al}	-	Adds costs for expensive alloys such as stainless steel	motor:2.80
			drive:3.00
C_{trans}	-	Adds cost for engine transmission ratio to the drives	20.00

The results for the CAPEX of the large-scale RPB absorber for a 250 MW_e CCGT power plant is presented in Table 6.14. The CAPEX includes the cost of material and construction for the RPB absorber.

Table 6.14 CAPEX for the large-scale RPB absorber for solvent-based PCC

Cost	Value (M$)	Cost	Value (M$)
C_{FOB}^{rotor} (M$)	1.37	C^{rotor} (M$)	2.17
C_{FOB}^{motor} (M$)	0.91	C^{motor} (M$)	0.95
C_{FOB}^{drive} (M$)	4.42	C^{drive} (M$)	3.363
	CAPEX (M$)		7.71

6.7 Comparison between PCC process using PB absorber and RPB absorber for large-scale PCC process

6.7.1 Size

In this section, the size of the RPB absorber is compared to the size of the PB absorbers obtained in Chapter 4 for the large-scale solvent-based PCC process. The diameter and packing height for the different configurations of the PCC process using PB and the diameter and packing height using RPB are shown in Table 6.15. The diameter and packing height of the RPB absorber are significantly lower than those of the PB. A reduction in packing volume of between 22–60 times was attained with the RPB absorber compared to the PB absorber. This is consistent with the finding of Joel et al. (2014). The volume of each of the PB units and the RPB unit was determined using the approach provided by Agarwal et al. (2010). The RPB absorber has 5-13 times the volume reduction factor compared to the PB absorbers. These reductions with RPB absorber are possible because of the high centrifugal acceleration which allows packings with high surface area to be utilized in the RPB. As shown in Table 6.15, the specific surface area of the packing used in the RPB absorber is 10-14 times higher than the specific surface area of the packings used in the PB absorbers.

Table 6.15 Size of RPB absorber against PB absorbers required for large-scale PCC process for 250 MW_e CCGT power plant

Description	PB absorbers for PCC process				RPB absorber
	Standard	Standard	AI	AIAFS	RPB
Solvent type	MEA	PZ	PZ	PZ	MEA
Solvent conc (wt%)	30	40	40	40	75
Inner diameter (m)					2.96
Outer diameter (m)	14	12.5	12	12	9.0
packing height (m)	30	20	15	15	1.20
Packing volume (m^3)	4618	2454	1697	1697	77
Packing volume reduction (times)					22-60
Unit volume (m^3)	4618[a]	2454[a]	1697[a]	1697[a]	347[b]
Volume reduction (times)					5-13
Packing specific surface(m^2/m^3)	151	205	205	205	2132
Void fraction	0.98	0.99	0.99	0.99	0.76

[a]Without the sump [b]calculated based on the assumptions provided by Agarwal et al. (2010)

6.7.2 Cost

In this section, the costs of the PB absorbers calculated in Chapter 4 are compared to the cost of the RPB absorber calculated in this chapter. The comparison is based on the CAPEX for the absorber alone. The CAPEX for the standard configuration of the PCC process using 30 wt% MEA and 40 wt% PZ was estimated to be $25.20 million and $14.70 million respectively. Likewise, the CAPEX for the AI and the AIAFS PCC process configurations using 40 wt% PZ was estimated to be $12.63 million. The CAPEX for the absorber in the AI and the AIAFS configurations are the same because they both have the same dimensions. With RPB absorber, the CAPEX is significantly reduced to $7.7 million. This is about a 39-69% reduction in CAPEX for the RPB absorber compared to the PB absorbers. Using RPB, the cost of the solvent-based PCC process could be reduced.

6.8 Conclusion

The validation, scale-up and technical and economic assessment of a PCC RPB absorber model using MEA were performed. The model predictions agreed with the experimental

data. A new iterative scale-up procedure was proposed and used for the scale-up of the RPB absorber model. This effort is the first to apply this step-by-step procedure to estimate the size of an RPB suitable for CO_2 capture from the flue gas of a 250 MW_e CCGT power plant. Technical analyses were carried out to study the influence of lean loading, MEA concentrations, rotor speed and lean solvent flow rate on the RPB absorber performance in terms of CO_2 capture level at MEA concentrations of 55, 65 and 75 wt%. Additionally, the size of the large scale RPB absorber was compared to the size of the PB absorbers. Sizes reduction of about 5-13 times was recorded with RPB absorbers compared to PB absorbers. Furthermore, economic assessments revealed that the CAPEX of the RPB absorber is significantly lower (by 39-69%) compared to the CAPEX of the PB absorbers.

Chapter 7 Conclusions and recommendations for future research

7.1 Conclusions

This thesis studies the modelling, simulation and performance evaluation of solvent-based PCC processes for a 250 MW_e CCGT power plant. The PCC process is studied based on PB and RPB technologies. MEA and PZ were used as absorbents.

7.1.1 New scale-up methodology proposed for PCC using PB

In chapter 3, the steady-state rate-based model of the solvent-based PCC process using MEA was developed in Aspen Plus®. The model was validated at a pilot scale using experimental data from the Separation Research Programme and Brindisi pilot plants. The PCC model predicted the pilot plants performance with maximum deviations of 9.43% using the SRP pilot plant data and 1.50% using the Brindisi pilot plant data. The model also correctly predicted the temperature profiles in the absorber and stripper of the SRP pilot plant depicting the locations of the temperature bulges in all the cases considered.

Furthermore, a new scale-up method based on the gas superficial flooding velocity was proposed and validated. This scale-up method accurately predicted the diameter of the PB absorber and stripper. The method was then used to design a large-scale PCC process for a 250 MW_e CCGT power plant. The scale-up method attained a lesser diameter for the absorber and stripper.

7.1.2 Techno-economic assessment of PCC using PB with different solvents and process configuration

A steady-state rate-based model was developed for the solvent-based PCC process using PZ in Aspen Plus®. The model was validated at pilot scale using experimental data collected at the SRP pilot plant at the University of Texas, USA. The model predictions agree with the experimental data to within ±10%. The validated pilot-scale PCC process model was scaled up to treat the flue gas from a 250 MW_e CCGT power plant. Different configurations of the PCC process including the standard, absorber intercooling and a combination of the absorber intercooling and advanced flash stripper were described and simulated for PZ concentrations of 30, 35 and 40 wt% PZ. Additionally, the technical and economic performance assessments of the different configurations of the large-scale PCC process

were carried out. They were compared to the standard large-scale PCC process using 30 wt% MEA.

The technical performance assessment revealed that the regeneration energy of the standard PCC process can be reduced from 4.97 GJ/t_{CO2} using 30 wt% MEA to 3.20 GJ/t_{CO2} using 30 wt% PZ. By modifying the process configuration to include an absorber intercooler and advanced flash stripper (AIAFS process configuration) the regeneration energy was reduced to 2.41 GJ/t_{CO2} with 40 wt% PZ as solvent. This is the least regeneration energy obtained for all process configurations and solvent concentrations considered. The least total energy consumption for CO2 capture and compression was estimated to be 2.76 GJ/t_{CO2}. This was also achieved with the AIAFS process using 40 wt% PZ as solvent. The economic performance assessment of the PCC process revealed that the total annual cost (TAC) and the CO_2 capture cost (CCC) of the standard PCC process using 30 wt% MEA was M$44.81/year. As with energy consumption, the least TAC and CCC of M$26.58/year and $34.65/$t_{CO2}$ were obtained with the AIAFS PCC process using 40 wt% PZ. This study provides insights into the energy and cost requirements of the large-scale PCC process using PZ.

7.1.3 Development of steady-state models for RPB Absorber with MEA and model validation

The methodology for rate-based model development for an RPB absorber in ACM® was described in detail. The mass and energy balances equations in the gas and liquid phases were developed based on some set of assumptions. The mass and heat transfer in RPB using two-film theory was discussed. Liquid and gas films mass transfers were considered and the effects of chemical reactions on mass transfer were accounted for with the enhancement factor. The interfacial heat transfer coefficient in the RPB model was also presented. The hydrodynamic properties such as the effective interfacial area, liquid holdup, and pressure drop were also incorporated into the model. Thermodynamic properties which is an important aspect of the CO_2 absorption modelling were estimated using the ElecNRTL thermodynamic method. The ways to calculate various physical properties used in the model was discussed. Additionally, the model was validated at pilot scale. The model predictions of the CO_2 capture level and rich CO_2 loading agreed well with the experimental data.

7.1.4 New RPB scale-up methodology and techno-economic assessment of PCC using RPB Absorber for 250 MW_e CCGT power plant

The RPB absorber model was scaled up using an iterative procedure to determine its basic dimensions such as the inner diameter, the outer diameter and the axial height that would be required to process flue gas from a 250 MW_e CCGT power plant. The technical assessment of the large-scale PCC process using RPB absorber showed the influence of different process parameters on CO_2 capture level at 55, 65 and 75 wt% MEA concentrations. It also revealed that the size of the PB absorbers was reduced by 5-13 times with the RPB absorber. Economic assessments showed that the CAPEX of the RPB absorber is $7.7 million. This is significantly lower compared to the value of $25.2 million, $14.70 million and $12.63 million obtained for the PB absorber in the standard MEA process, standard PZ process, PZ process with absorber intercooling and PZ process with absorber intercooling and advanced flash stripper.

7.2 Recommendations for future research

The following areas are recommended for further research on the performance evaluation of the solvent-based PCC process.

7.2.1 Implementation of process improvement schemes and optimization of the PCC process using PB and MEA solvent

Although the energy consumption of the large-scale MEA-based PCC process developed in the thesis is lower than in previous studies, it is however still very high compared to those obtained with large-scale PCC processes using PZ. One way to reduce this is to implement process improvement schemes such as absorber intercooling, split flow and a combination of absorber intercooling and advanced flash stripper amongst others in the large-scale MEA process. Process optimization of the large-scale MEA-based PCC process would reveal sets of operating conditions that would result in lower energy consumption and cost, thus an adequate optimization of the MEA process should be performed. The huge absorber size also contributed to the very high CAPEX of the absorber in the MEA-based PCC process. This is because of the type of packing used in the absorber. Switching to higher efficiency structural packing will significantly reduce the height of the packing and consequently may lead to a reduction in the cost of the MEA-based PCC process. Additionally, the new scale-up method proposed in this thesis assumed 70% flooding

velocity. A sensitivity study of the influence of the flooding velocity on the size of the absorber and the stripper at different flooding percentage should be carried out. This will help in finding the most appropriate range of flooding percentage to choose from when designing PB absorbers and strippers.

7.2.2 Study on solid formation in solvent-based PCC process using PZ solvent

PZ is known to form solids that precipitate out of lean PZ solvent streams at temperatures below 20 °C. This solid formation needs to be carefully monitored. While this may not be a problem in PZ-based PCC plants in temperate regions such as Africa and the Middle East, it will certainly be a challenge for PZ-based PCC plants in regions with cold temperatures such as Europe and North America where temperatures are mostly below 20 °C in winter months. Therefore, a study of the formation of solid and its implication for the design and operation of the PCC process using PZ solvent must be carefully assessed. This would help design engineers and operators know the areas of the plant where solid formations are likely to occur and the steps that need to be taken to avoid them.

Furthermore, the life cycle analysis (LCA) was not performed for the PCC processes developed in this thesis. It is therefore recommended that future development and analysis of the PCC process should include the cradle-to-grave assessment to quantify its impacts on the environment.

7.2.3 Model development for the whole intensified solvent-based PCC process

The modelling and simulation of the whole PCC process using RPB are critical to understanding the requirements of the process based on this technology. Therefore, the complete model of the PCC process including the RPB absorber, RPB stripper, heat exchangers, pumps, coolers needs to be carried out for both pilot-scale and large-scale PCC processes. Therefore, a study integrating these components is needed to gain insights into the design and operations of the whole PCC process based on RPB. Optimization of the whole process would reveal how the performance of the PCC process using RPB could be better improved. This would present the whole picture of the benefits that RPB technology offers to the solvent-based PCC process.

7.2.4 Study of solvent-based PCC process using PZ solvent

The residence time in RPB is very short. In other words, it means the contact time between the solvent and the flue gas is very short. Using solvents such as PZ that reacts almost two times faster with CO_2 than MEA could be a potential game-changer for this process. With MEA, concentrations in the region of 70-75 wt% MEA have been found to give the best results in the PCC process using RPB. At these concentrations, equipment corrosion problem is exacerbated and the need for corrosion inhibitors is greatly increased. With PZ this problem would be avoided as lower concentrations would be required for the CO2 capture function in RPB. Thus, a detailed study on the use of PZ for CO2 capture in RPB needs to be carried out.

References

Aboudheir, A., Tontiwachwuthikul, P., Chakma, A., Idem, R., 2003. Kinetics of the reactive absorption of carbon dioxide in high CO_2-loaded, concentrated aqueous monoethanolamine solutions. Chem. Eng. Sci., 58, 5195–5210.

Abu-Zahra, M.R.M., Niederer, J.P.M., Feron, P.H.M., Versteeg, G.F., 2007a. CO_2 capture from power plants. Part II. A parametric study of the economical performance based on mono-ethanolamine. Int. J. Greenh. Gas Control, 1, 135–142.

Abu-Zahra, M.R.M., Schneiders, L.H.J., Niederer, J.P.M., Feron, P.H.M., Versteeg, G.F., 2007b. CO_2 capture from power plants: Part I. A parametric study of the technical performance based on monoethanolamine. Int. J. Greenh. Gas Control, 1, 37–46.

Agarwal, L., Pavani, V., Rao, D.P., Kaistha, N., 2010. Process intensification in HiGee absorption and distillation: Design procedure and applications. Ind. Eng. Chem. Res., 49, 10046–10058.

Agbonghae, E.O., Hughes, K.J., Ingham, D.B., Ma, L., Pourkashanian, M., 2014. Optimal process design of commercial-scale amine-based CO_2 capture plants. Ind. Eng. Chem. Res., 53, 14815–14829.

Ahmad, A.L., Sunarti, A.R., Lee, K.T., Fernando, W.J.N., 2010. International Journal of Greenhouse Gas Control CO_2 removal using membrane gas absorption. Int. J. Greenh. Gas Control, 4, 495–498.

Akram, M., Ali, U., Best, T., Blakey, S., Finney, K.N., Pourkashanian, M., 2016. Performance evaluation of PACT Pilot-plant for CO_2 capture from gas turbines with Exhaust Gas Recycle. Int. J. Greenh. Gas Control, 47, 137–150.

Alhajaj, A., Mac Dowell, N., Shah, N., 2016. A techno-economic analysis of post-combustion CO_2 capture and compression applied to a combined cycle gas turbine: Part I. A parametric study of the key technical performance indicators. Int. J. Greenh. Gas Control, 44, 26–41.

Arias, A.M., Mores, P.L., Scenna, N.J., Mussati, S.F., 2016. Optimal design and sensitivity analysis of post-combustion CO_2 capture process by chemical absorption with amines. J. Clean. Prod., 115, 315–331.

Aroonwilas, A., Veawab, A., 2004. Characterization and Comparison of the CO_2 Absorption Performance into Single and Blended Alkanolamines in a Packed Column. Ind. Eng. Chem. Res., 43, 2228–2237.

Aspentech, 2012. Aspen Capital Cost Estimator: User's Guide. Aspen Technol. Inc. version 8., 738.

Aspentech, 2008. Rate-based model of the CO2 capture process by MEA using Aspen plus. Burlington, MA.

Aspentech, 2001. Physical property methods and models 11.1. Cambridge, MA.

Ayyad, A., Abbas, A., Elminshawy, N., 2021. A simulation study of the effect of post-combustion amine-based carbon-capturing integrated with solar thermal collectors

for combined cycle gas power plant. Discov. Sustain., 2, 1-21.

Bae, T.H., Hudson, M.R., Mason, J.A., Queen, W.L., Dutton, J.J., Sumida, K., Micklash, K.J., Kaye, S.S., Brown, C.M., Long, J.R., 2013. Evaluation of cation-exchanged zeolite adsorbents for post-combustion carbon dioxide capture. Energy Environ. Sci., 6, 128–138.

Baxter, L.L., Baxter, A., Bever, E., Burt, S., Chamberlain, S., Frankman, D., Hoeger, C., Mansfield, E., Parkinson, D., Sayre, A., Stitt, K., 2019. Cryogenic Carbon Capture Development: Final/Technical report. Pennsylvania.

Biliyok, C., Lawal, A., Wang, M., Seibert, F., 2012. Dynamic modelling, validation and analysis of post-combustion chemical absorption CO_2 capture plant. Int. J. Greenh. Gas Control, 9, 428–445.

Biliyok, C., Yeung, H., 2013. Evaluation of natural gas combined cycle power plant for post-combustion CO_2 capture integration. Int. J. Greenh. Gas Control, 19, 396–405.

Billet, R., Schultes, M., 1999. Prediction of Mass Transfer Columns with Dumped and Arranged Packings. Chem. Eng. Res. Des., 77, 498–504.

Bird, R.B., Stewart, E.W., Lightfoot, N.E., 2007. Transport Phenomena, 2nd. ed. John Wiley & Sons, INC, New York.

Bishnoi, S., Rochelle, G.T., 2000. Absorption of carbon dioxide into aqueous piperazine: reaction kinetics, mass transfer and solubility. Chem. Eng. Sci., 55, 5531–5543.

Borhani, T.N., Oko, E., Wang, M., 2019. Process modelling, validation and analysis of rotating packed bed stripper in the context of intensified CO_2 capture with MEA. J. Ind. Eng. Chem., 75, 285–295.

Borhani, T.N., Oko, E., Wang, M., 2018. Process modelling and analysis of intensified CO_2 capture using monoethanolamine (MEA) in rotating packed bed absorber. J. Clean. Prod., 204, 1124–1142.

BP, 2017. BP Energy Outlook Energy 2017. BP Stat. Rev. World Energy 52.

Bravo, J, L. Rocha, J, A. Fair, J, R., 1985. Mass transfer in Gauze Packings. Hydrocarb. Process, 64, 91–95.

Bravo, J.L., Patwardhan, A.A., Edgar, T.F., 1992. Influence of Effective Interfacial Areas in the Operation and Control of Packed Distillation Columns. Ind. Eng. Chem. Res., 31, 604–608.

Brunazzi, E., Macías-Salinas, R., Viva, A., 2008. Calculation Procedure for Flooding in Packed Columns Using a Channel Model. Chem. Eng. Commun., 196, 330–341.

Bui, M., Adjiman, C.S., Bardow, A., Anthony, E.J., Boston, A., Brown, S., Fennell, P.S., Fuss, S., Galindo, A., Hackett, L.A., Hallett, J.P., Herzog, H.J., Jackson, G., Kemper, J., Krevor, S., Maitland, G.C., Matuszewski, M., Metcalfe, I.S., Petit, C., Puxty, G., Reimer, J., Reiner, D.M., Rubin, E.S., Scott, S.A., Shah, N., Smit, B., Trusler, J.P.M., Webley, P., Wilcox, J., Mac Dowell, N., 2018. Carbon capture and storage (CCS): The way forward. Energy Environ. Sci., 11, 1062–1176.

Burns, J.R., Jamil, J.N., Ramshaw, C., 2000. Process intensification: operating characteristics of rotating packed beds — determination of liquid hold-up for a high-voidage structured packing. Chem. Eng. Sci., 55, 2401–2415.

Buvik, V., Bernhardsen, I.M., Figueiredo, R. V., Vevelstad, S.J., Goetheer, E., van Os, P., Knuutila, H.K., 2021. Measurement and prediction of oxygen solubility in post-combustion CO_2 capture solvents. Int. J. Greenh. Gas Control 104, 103205. https://doi.org/10.1016/j.ijggc.2020.103205

Canepa, R., Wang, M., Biliyok, C., Satta, A., 2013. Thermodynamic analysis of combined cycle gas turbine power plant with post-combustion CO_2 capture and exhaust gas recirculation. Proc. Inst. Mech. Eng. Part E J. Process Mech. Eng. 227, 89–105.

Chen, C. -C, Evans, L.B., 1986. A local composition model for the excess Gibbs energy of aqueous electrolyte systems. AIChE J., 32, 444–454.

Chen, E., Madan, T., Sachde, D., Walters, M.S., Nielsen, P., Rochelle, G.T., 2013. Pilot Plant Results with Piperazine. Energy Procedia, 37, 1572–1583.

Chen, E., Zhang, Y., Lin, Y., Nielsen, P., Rochelle, G., 2017. Review of Recent Pilot Plant Activities with Concentrated Piperazine. Energy Procedia, 114, 1110–1127.

Chen, Y., Lin, C., Liu, H., 2005a. Mass Transfer in a Rotating Packed Bed with Viscous Newtonian and Non-Newtonian Fluids. Ind. Eng. Chem. Res., 44, 1043–1051.

Chen, Y., Lin, C., Liu, H., 2005b. Mass Transfer in a Rotating Packed Bed with Various Radii of the Bed. Ind. Eng. Chem. Res., 40, 7868–7875.

Chen, Y., Lin, F., Lin, C., Tai, C.Y., Liu, H., Re, S., 2006. Packing Characteristics for Mass Transfer in a Rotating Packed Bed. Ind. Eng. Chem. Res., 45, 6846–6853.

Chen, Y.S., 2011. Correlations of mass transfer coefficients in a rotating packed bed. Ind. Eng. Chem. Res., 50, 1778–1785.

Chen, Y.S., Liu, H.S., 2002. Absorption of VOCs in a rotating packed bed. Ind. Eng. Chem. Res., 41, 1583–1588.

Cheng, H.-H., Lai, C.-C., Tan, C.-S., 2013. Thermal regeneration of alkanolamine solutions in a rotating packed bed. Int. J. Greenh. Gas Control, 16, 206–216.

Cheng, H.-H., Tan, C.-S., 2011. Removal of CO_2 from indoor air by alkanolamine in a rotating packed bed. Sep. Purif. Technol., 82, 156–166.

Chilton, T.H., Colburn, A.P., 1934. Mass Transfer (Absorption) Coefficients: Prediction from Data on Heat Transfer and Fluid Friction. Ind. Eng. Chem., 26, 1183–1187.

Clark, J.. K.A., 1964. Kinetics of absorption of carbon dioxide in aqueous ammonia solutions at short contact times. Ind. Chem. Eng. Fundam., 3, 239–245.

CO2earth., Atmospheric CO2. Available from https://www.co2.earth/ (accessed 12 December 2021).

Cortes Garcia, G.E., van der Schaaf, J., Kiss, A.A., 2017. A review on process intensification in HiGee distillation. J. Chem. Technol. Biotechnol., 92, 1136–1156.

Coulson, J.M., Richardson, J.F., 2002. Chemical Engineering, 5th ed. Butterwoth Heinemann, Oxford.

Cousins, A., Huang, S., Cottrell, A., Feron, P.H.M., Eric, C., Rochelle, G.T., 2014. Pilot-scale parametric evaluation of concentrated piperazine for CO_2 capture at an Australian coal-fired power station. Greenh. Gases Sci. Technol., 5, 7–16.

Cousins, A., Wardhaugh, L.T., Feron, P.H.M., 2011. Preliminary analysis of process flow sheet modifications for energy-efficient CO_2 capture from flue gases using chemical absorption. Chem. Eng. Res. Des., 89, 1237–1251.

Cullinane, J.T., Rochelle, G.T., 2006. Kinetics of carbon dioxide absorption into aqueous potassium carbonate and piperazine. Ind. Eng. Chem. Res., 45, 2531–2545.

Danckwerts, P. V., 1951. Surface renewal theory. Ind. Eng. Chem., 43, 1460-1467.

Danckwerts, P. V., 1970. Gas-Liquid Reactions. McGraw Hill, New York.

Davison, J., 2007. Performance and costs of power plants with capture and storage of CO_2. Energy, 32, 1163–1176.

De Koeije, G., Enge, Y., Sanden, K., Graff, O.F., Falk-Pedersen, O., Amundsen, T., Overå, S., 2011. CO_2 Technology Centre Mongstad-Design, functionality and emissions of the amine plant. Energy Procedia, 4, 1207–1213.

Derks, P.W.J., Kleingeld, T., van Aken, C., Hogendoorn, J.A., Versteeg, G.F., 2006. Kinetics of absorption of carbon dioxide in aqueous piperazine solutions. Chem. Eng. Sci., 61, 6837–6854.

Diego, M.E., Bellas, J.M., Pourkashanian, M., 2018. Techno-economic analysis of a hybrid CO2 capture system for natural gas combined cycles with selective exhaust gas recirculation. Appl. Energy, 215, 778–791.

Dugas, R., 2006. Pilot Plant Study of Carbon Dioxide Capture by Aqueous Monoethanolamine. MSE Thesis. University of Texas at Austin.

Dutta, R., Nord, L.O., Bolland, O., 2017. Selection and design of post-combustion CO_2 capture process for 600 MW natural gas-fueled thermal power plant based on operability. Energy, 121, 643–656.

Eckert, J.S., 1970. Selecting the Proper Distillation Column Packing. Chem. Eng. Prog., 66, 39–44.

Edwards, T.J., Newman, J., Prausnitz, J.M., 1975. Thermodynamics of aqueous solutions containing volatile weak electrolytes. AIChE J., 21, 248–259.

Enaasen, N. F., Kvamsdal, H.M., Hillestad, M., 2016. Dynamic simulation of post-combustion CO_2 capture for flexible operation of the Brindisi pilot plant. Int. J. Greenh. Gas Control, 48, 204–215.

Enaasen, N.F., 2015. Post-combustion absorption-based CO2 capture : modelling, validation and analysis of process dynamics. PhD Thesis. Norwegian University of Science and Technology.

Energy, N.R.G., 2014. WA Parish CO2 capture project. Available from https://www.lexissecuritiesmosaic.com/gateway/FedReg/business_pla-2014-petranova-waparish-factsheet.pdf (accessed on 10 August 2021).

Ermatchkov, V., Pérez-Salado Kamps, Á., Maurer, G., 2003. Chemical equilibrium constants for the formation of carbamates in (carbon dioxide + piperazine + water) from 1H-NMR-spectroscopy. J. Chem. Thermodyn., 35, 1277–1289.

Ermatchkov, V., Pérez-Salado Kamps, Á., Speyer, D., Maurer, G., 2006. Solubility of carbon dioxide in aqueous solutions of piperazine in the low gas loading region. J. Chem. Eng. Data, 51, 1788–1796.

Frailie, P.T., 2014. Modelling of carbon dioxide absorption/stripping by aqueous methyldiethanolamine/piperazine. PhD Thesis. University of Texas at Austin.

Freeman, S.A., Dugas, R., Van Wagener, D.H., Nguyen, T., Rochelle, G.T., 2010. Carbon dioxide capture with concentrated, aqueous piperazine. Int. J. Greenh. Gas Control, 4, 119–124.

Freeman, S.A., Rochelle, G.T., 2011. Density and viscosity of aqueous (piperazine + carbon dioxide) solutions. J. Chem. Eng. Data, 56, 574–581.

Freguia, S., Rochelle, G.T., 2003. Modelling of CO_2 capture by aqueous monoethanolamine. AIChE J., 49, 1676–1686.

Frimpong, R.A., Nikolic, H., Pelgen, J., Ghorbanian, M., Figueroa, J.D., Liu, K., 2019. Evaluation of different solvent performance in a 0.7 MWe pilot-scale CO_2 capture unit. Chem. Eng. Res. Des., 148, 11–20.

Fu, K., Chen, G., Liang, Z., Sema, T., Idem, R., 2014. Analysis of Mass Transfer Performance of Monoethanolamine-Based CO_2 Absorption in a Packed Column Using Artificial Neural Networks. Ind. Eng. Chem. Res., 53, 4413-4423.

Gabrielsen, J., Michelsen, M.L., Stenby, E.H., Kontogeorgis, G.M., 2005. A model for estimating CO_2 solubility in aqueous alkanolamines. Ind. Eng. Chem. Res., 44, 3348–3354.

Gao, T., Rochelle, G.T., 2020. CO_2 Absorption from Gas Turbine Flue Gas by Aqueous Piperazine with Intercooling. Ind. Eng. Chem. Res., 59, 7174–7181.

Gao, T., Selinger, J.L., Rochelle, G.T., 2019. Demonstration of 99% CO_2 removal from coal flue gas by amine scrubbing. Int. J. Greenh. Gas Control, 83, 236–244.

Garcia, M., Knuutila, H.K., Gu, S., 2017. Aspen Plus simulation model for CO_2 removal with MEA: Validation of desorption model with experimental data. J. Environ. Chem. Eng., 5, 4693–4701.

García, S., Gil, M. V., Pis, J.J., Rubiera, F., Pevida, C., 2013. Cyclic operation of a fixed-bed pressure and temperature swing process for CO_2 capture: Experimental and statistical analysis. Int. J. Greenh. Gas Control, 12, 35–43.

Gaspar, J., Cormos, A.M., 2012. Dynamic modelling and absorption capacity assessment of CO_2 capture process. Int. J. Greenh. Gas Control, 8, 45–55.

Geankoplis, C.J., 2014. Transport Process & Separation Process Principles (Includes Unit Operations), 4th ed. Pearson Education Limited, Essex.

Gelowitz, D., Supap, T., Abdulaziz, N., Sema, T., Idem, R., Tontiwachwuthikul, P., 2013. Part 8: Post-combustion CO_2 capture: pilot plant operation issues. Carbon Manag., 4, 215–231.

Ghalib, L., Ali, B.S., Ashri, W.M., Mazari, S., Saeed, I.M., 2017. Modelling the effect of piperazine on CO_2 loading in MDEA/PZ mixture. Fluid Phase Equilib., 434, 233–243.

Grande, C.A., 2012. Advances in Pressure Swing Adsorption for Gas Separation. ISRN Chem. Eng., 2012, 1–13.

Grande, C.A., Ribeiro, R.P.L., Oliveira, E.L.G., Rodrigues, A.E., 2009. Electric swing adsorption as emerging CO_2 capture technique. Energy Procedia, 1, 1219–1225.

Gudena, K., Rangaiah, G.P., Lakshminarayanan, S., 2013. HiGee stripper-membrane system for decentralized bioethanol recovery and purification. Ind. Eng. Chem. Res., 52, 4572–4585.

Hanley, B., Chen, C.-C., 2012. New Mass-Transfer Correlations for Packed Towers. AICHE J., 58, 2290–2292.

Harun, N., Nittaya, T., Douglas, P.L., Croiset, E., Ricardez-Sandoval, L.A., 2012. Dynamic simulation of MEA absorption process for CO_2 capture from power plants. Int. J. Greenh. Gas Control, 10, 295–309.

Hedin, N., Andersson, L., Bergström, L., Yan, J., 2013. Adsorbents for the post-combustion capture of CO_2 using rapid temperature swing or vacuum swing adsorption. Appl. Energy, 104, 418–433.

Hemmati, A., Farahzad, R., Surendar, A., Aminahmadi, B., 2019. Validation of mass transfer and liquid holdup correlations for CO_2 absorption process with methyldiethanolamine Solvent and piperazine as an activator. Process Saf. Environ. Prot., 126, 214–222.

Hetzer, H.B., Robinson, R.A., Bates, R.G., 1967. Dissociation constants of piperazinium ion and related thermodynamic quantities from 0 to 50 deg. J. Phys. Chem., 72, 2081–2086.

Higbie, R., 1935. The rate of absorption of a pure gas into a still liquid during short periods of exposure. Trans Am. Ina. Chem. Eng., 31, 365–389.

Horvath, A.L., 1985. Handbook of aqueous electrolyte solutions: Physical properties, estimation and correlation methods. Ellis Horwood, Chichester.

Idem, R., Supap, T., Shi, H., Gelowitz, D., Ball, M., Campbell, C., Tontiwachwuthikul, P., 2015. Practical experience in post-combustion CO_2 capture using reactive solvents in large pilot and demonstration plants. Int. J. Greenh. Gas Control, 40, 6–25.

IEA-GHG, 2006. CO2 capture in low-rank coal power plant. IEA Greenh. Gas R&D Program. Rep. no2006/1.

IEA, 2021. Electricity Information: Overview. Available from https://www.iea.org/reports/electricity-information-overview (accessed on 20

December 2021).

IEA, 2019. World Energy Outlook 2019. World Energy Outlook Ser. 1–810.

Im, D., Jung, H., Lee, J.H., 2020. Modelling, simulation and optimization of the rotating packed bed (RPB) absorber and stripper for MEA-based carbon capture. Comput. Chem. Eng., 143, 107102.

International Energy Agency, 2010. Energy Technology Perspectives: Scenarios & Strategies To 2050, International Energy Agency (IEA) Publications.

IPCC, 2014. Climate Change 2014 Synthesis Report Summary Chapter for Policymakers. Intergov. Panel Clim. Chang. 31.

IPCC, 2005. Carbon dioxide capture and storage, IPCC special report on Carbon dioxide capture and storage. New York.

Ishibashi, M., Ota, H., Akutsu, N., Umeda, S., Tajika, M., Izumi, J., Yasutake, A., Kabata, T., Kageyama, Y., 1996. Technology for removing carbon dioxide from power plant flue gas by the physical adsorption method. Energy Convers. Manag., 37, 929–933.

Plaza, J, M., 2011. Modelling of Carbon Dioxide Absorption using Aqueous Monoethanolamine, Piperazine and Promoted Potassium Carbonate. PhD Thesis. University of Texas at Austin.

Jassim, M.S., Rochelle, G., Eimer, D., Ramshaw, C., 2007. Carbon dioxide absorption and desorption in aqueous monoethanolamine solutions in a rotating packed bed. Ind. Eng. Chem. Res., 46, 2823–2833.

Jenkins, J., 2015. Financing mega-scale energy projects: a case study of the Petra Nova carbon capture project, Paulson Institute., 1-13.

Joel, A.S., Wang, M., Ramshaw, C., 2015. Modelling and simulation of intensified absorber for post-combustion CO_2 capture using different mass transfer correlations. Appl. Therm. Eng., 74, 47–53.

Joel, A.S., Wang, M., Ramshaw, C., Oko, E., 2017. Modelling, simulation and analysis of intensified regenerator for solvent-based carbon capture using rotating packed bed technology. Appl. Energy, 203, 11–25.

Joel, A.S., Wang, M., Ramshaw, C., Oko, E., 2014. Process analysis of intensified absorber for post-combustion CO_2 capture through modelling and simulation. Int. J. Greenh. Gas Control, 21, 91–100.

Kang, J.L., Sun, K., Wong, D.S.H., Jang, S.S., Tan, C.S., 2014. Modelling studies on absorption of CO_2 by monoethanolamine in rotating packed bed. Int. J. Greenh. Gas Control, 25, 141–150.

Karimi, M., Hillestad, M., Svendsen, H.F., 2011. Capital costs and energy considerations of different alternative stripper configurations for post-combustion CO_2 capture. Chem. Eng. Res. Des., 89, 1229–1236.

Kenarsari, S.D., Yang, D., Jiang, G., Zhang, S., Wang, J., Russell, A.G., Wei, Q., Fan, M., 2013. Review of recent advances in carbon dioxide separation and capture. RSC Adv., 3,

22739.

Kenig, E.Y., Schneider, R., Górak, A., 2001. Reactive absorption: Optimal process design via optimal modelling. Chem. Eng. Sci., 56, 343–350.

Kenig, E, Y., Kucka, L., Górak, A., 2003. Rigorous modelling of reactive processes. Chem. Eng. Technol., 26, 6–15.

Kenneth, D., 2017. Petra Nova is one of two carbon capture and sequestration power plants in the world. From https://www.eia.gov/todayinenergy/detail.php?id=33552 (accessed on 1 November 2018).

Khalifa, O., Alkhatib, I.I.I., Bahamon, D., Alhajaj, A., Abu-Zahra, M.R.M., Vega, L.F., 2022. Modifying absorption process configurations to improve their performance for Post-Combustion CO_2 capture – What have we learned and what is still missing? Chem. Eng. J., 430, 133096.

Khan, F.M., Krishnamoorthi, V., Mahmud, T., 2011. Modelling reactive absorption of CO_2 in packed columns for post-combustion carbon capture applications. Chem. Eng. Res. Des., 89, 1600–1608.

Kim, I., Svendsen, H.F., 2007. Heat of absorption of carbon dioxide (CO_2) in monoethanolamine (MEA) and 2-(aminoethyl)ethanolamine (AEEA) solutions. Ind. Eng. Chem. Res., 46, 5803–5809.

Kister, H.Z., Gill, D.R., 1992. Flooding and Pressure Drop Prediction for Structured Packings. IChemE Symp. Ser., 128 A109–A123.

Kister, H.Z., Gill, R.D., 1991. Predict Flood Point and Pressure Drop for Modern Random Packings. Chem. Eng. Prog., 87, 32–42.

Kister, H.Z., Scherffius, J., Afshar, K., Abkar, E., 2007. Realistically predict capacity and pressure drop for packed columns. Chem. Eng. Prog., 103, 28–38.

Knudsen, J.N., Andersen, J., Jensen, J.N., Biede, O., 2011. Evaluation of process upgrades and novel solvents for the post-combustion CO_2 capture process in pilot-scale. Energy Procedia, 4, 1558–1565.

Knudsen, J.N., Jensen, J.N., Vilhelmsen, P.J., Biede, O., 2009. Experience with CO_2 capture from coal flue gas in pilot-scale: Testing of different amine solvents. Energy Procedia, 1, 783–790.

Krótki, A., Więcław Solny, L., Stec, M., Spietz, T., Wilk, A., Chwoła, T., Jastrząb, K., 2020. Experimental results of advanced technological modifications for a CO_2 capture process using amine scrubbing. Int. J. Greenh. Gas Control, 96, 103014.

Kucka, L., Müller, I., Kenig, E.Y., Górak, A., 2003. On the modelling and simulation of sour gas absorption by aqueous amine solutions. Chem. Eng. Sci., 58, 3571–3578.

Kvamsdal, H.M., Jakobsen, J.P., Hoff, K.A., 2009. Dynamic modelling and simulation of aCO2 absorber column for post-combustion CO_2 capture. Chem. Eng. Process. Process Intensif., 48, 135–144.

Lawal, A., Wang, M., Stephenson, P., Koumpouras, G., Yeung, H., 2010. Dynamic modelling

and analysis of post-combustion CO_2 chemical absorption process for coal-fired power plants. Fuel, 89, 2791–2801.

Lawal, A., Wang, M., Stephenson, P., Obi, O., 2012. Demonstrating full-scale post-combustion CO_2 capture for coal-fired power plants through dynamic modelling and simulation. Fuel, 101, 115–128.

Lawal, A., Wang, M., Stephenson, P., Yeung, H., 2009. Dynamic modelling of CO2absorption for post-combustion capture in coal-fired power plants. Fuel, 88, 2455–2462.

Lee, J., Kolawole, T., Attidekou, P., 2017. Carbon Capture from a Simulated Flue Gas Using a Rotating Packed Bed Adsorber and Monoethanolamine (MEA). Energy Procedia, 114, 1834–1840.

Lemaire, E., Bouillon, P.A., Lettat, K., 2014. Development of HiCapt^{+TM} Process for CO_2 Capture from Lab to Industrial Pilot Plant. Oil Gas Sci. Technol. – Rev. d'IFP Energies Nouv., 69, 1069–1080.

Lepaumier, H., Da Silva, E.F., Einbu, A., Grimstvedt, A., Knudsen, J.N., Zahlsen, K., Svendsen, H.F., 2011. Comparison of MEA degradation in pilot-scale with lab-scale experiments. Energy Procedia, 4, 1652–1659.

Leva, M., 1954. Flow Through Irrigated Dumped Packings. Chem. Eng. Prog., 50, 51–59.

Li, K., Leigh, W., Feron, P., Yu, H., Tade, M., 2016. Systematic study of aqueous monoethanolamine (MEA)-based CO_2 capture process: Techno-economic assessment of the MEA process and its improvements. Appl. Energy, 165, 648–659.

Li, L., Voice, A.K., Li, H., Namjoshi, O., Nguyen, T., Du, Y., Rochelle, G.T., 2013. Amine blends using concentrated piperazine. Energy Procedia, 37, 353–369.

Liang, Z. (Henry), Rongwong, W., Liu, H., Fu, K., Gao, H., Cao, F., Zhang, R., Sema, T., Henni, A., Sumon, K., Nath, D., Gelowitz, D., Srisang, W., Saiwan, C., Benamor, A., Al-Marri, M., Shi, H., Supap, T., Chan, C., Zhou, Q., Abu-Zahra, M., Wilson, M., Olson, W., Idem, R., Tontiwachwuthikul, P. (PT), 2015. Recent progress and new developments in post-combustion carbon-capture technology with amine-based solvents. Int. J. Greenh. Gas Control, 40, 26–54.

Liguori, S., Wilcox, J., 2018. Design considerations for post-combustion CO2 capture with membranes, In Current Trends and Future Developments on (Bio-) Membranes: Carbon Dioxide Separation/Capture by Using Membranes. Elsevier Inc., Amsterdam, Netherlands.

Lin, C.C., Chen, Y.W., 2011. Performance of a cross-flow rotating packed bed in removing carbon dioxide from gaseous streams by chemical absorption. Int. J. Greenh. Gas Control, 5, 668–675.

Lin, C.C., Lin, Y.H., Tan, C.S., 2010. Evaluation of alkanolamine solutions for carbon dioxide removal in cross-flow rotating packed beds. J. Hazard. Mater., 175, 344–351.

Lin, Y.-J., Rochelle, G.T., 2016. Approaching a reversible stripping process for CO_2 capture. Chem. Eng. J., 283, 1033–1043.

Lin, Y.-J., Rochelle, G.T., 2014. Optimization of Advanced Flash Stripper for CO_2 Capture using Piperazine. Energy Procedia, 63, 1504–1513.

Lin, Y.J., Chen, E., Rochelle, G.T., 2016. Pilot plant test of the advanced flash stripper for CO2 capture. Faraday Discuss., 192, 37–58.

Littel, R.J., Versteeg, G.F., Van Swaaij, W.P.M., 1992. Kinetics of CO_2 with primary and secondary amines in aqueous solutions-II. Influence of temperature on zwitterion formation and deprotonation rates. Chem. Eng. Sci., 47, 2037–2045.

Liu, L., Fang, M., Xu, S., Wang, J., Guo, D., 2022. Development and testing of a new post-combustion CO2 capture solvent in pilot and demonstration plant. Int. J. Greenh. Gas Control, 113, 103513.

Liu, W., Luo, Y., Liu, Y.Z., Chu, G.W., 2020. Scale-Up of a Rotating Packed Bed Reactor with a Mesh-Pin Rotor: (I) Hydrodynamic Studies. Ind. Eng. Chem. Res., 59, 5114–5123.

Liu, Y., Hseuh, B.F., Gao, Z., Wong, D.S.H., Yao, Y., 2019. Dynamic Profile Monitoring for Flooding Prognosis in Packed Columns. Chem. Eng. Technol., 42, 1232–1239.

Llerena-Chavez, H., Larachi, F., 2009. Analysis of flow in rotating packed beds via CFD simulations—Dry pressure drop and gas flow maldistribution. Chem. Eng. Sci., 64, 2113–2126.

Lobo, W.., Friend, L., Hashmall, H., Zenz, F.A., 1945. Limiting Capacity of Dumped Tower Packings. Trans Am. Inst. Chem. Eng., 41, 693–710.

Luo, X., 2016. Modelling, Simulation and Optimisation of Natural Gas Combined Cycle Power Plant Integrated with Carbon Capture. PhD Thesis. University of Hull, UK.

Luo, X., Wang, M., 2017. Improving Prediction Accuracy of a Rate-Based Model of an MEA-Based Carbon Capture Process for Large-Scale Commercial Deployment. Engineering, 3, 232–243.

Luo, X., Wang, M., Lee, J., Hendry, J., 2021. Dynamic modelling based on surface renewal theory, model validation and process analysis of rotating packed bed absorber for carbon capture. Appl. Energy, 301, 117462.

Luo, Y., Chu, G.W., Zou, H.K., Wang, F., Xiang, Y., Shao, L., Chen, J.F., 2012a. Mass transfer studies in a rotating packed bed with novel rotors: Chemisorption of CO_2. Ind. Eng. Chem. Res., 51, 9164–9172.

Luo, Y., Chu, G.W., Zou, H.K., Zhao, Z.Q., Dudukovic, M.P., Chen, J.F., 2012b. Gas-liquid effective interfacial area in a rotating packed bed. Ind. Eng. Chem. Res., 51, 16320–16325.

Ma, X., Wang, X., Song, C., 2009. "Molecular basket" sorbents for separation of CO_2 and H_2S from various gas streams. J. Am. Chem. Soc., 131, 5777–5783.

Mac Dowell, N., Shah, N., 2014. Dynamic modelling and analysis of a coal-fired power plant integrated with a novel split-flow configuration post-combustion CO_2 capture process. Int. J. Greenh. Gas Control, 27, 103–119.

Madan, T., Van Wagener, D.H., Chen, E., Rochelle, G.T., 2013. Modelling pilot plant results

for CO2 stripping using piperazine in a two-stage flash. Energy Procedia, 37, 386–399.

Mangalapally, H.P., Hasse, H., 2011. Pilot plant study of post-combustion carbon dioxide capture by reactive absorption: Methodology, comparison of different structured packings, and comprehensive results for monoethanolamine. Chem. Eng. Res. Des., 89, 1216–1228.

Mangalapally, H.P., Notz, R., Hoch, S., Asprion, N., Sieder, G., Garcia, H., Hasse, H., 2009. Pilot plant experimental studies of post-combustion CO_2 capture by reactive absorption with MEA and new solvents. Energy Procedia, 1, 963–970.

Mantripragada, H.C., Zhai, H., Rubin, E.S., 2019. Boundary Dam or Petra Nova – Which is a better model for CCS energy supply? Int. J. Greenh. Gas Control, 82, 59–68.

Manzolini, G., Sanchez Fernandez, E., Rezvani, S., Macchi, E., Goetheer, E.L.V., Vlugt, T.J.H., 2015. Economic assessment of novel amine-based CO2 capture technologies integrated in power plants based on European Benchmarking Task Force methodology. Appl. Energy, 138, 546–558.

Marx-Schubach, T., Schmitz, G., 2019. Modelling and simulation of the start-up process of coal-fired power plants with post-combustion CO2 capture. Int. J. Greenh. Gas Control, 87, 44–57.

Mazari, S.A., Ali, B.S., Jan, B.M., Saeed, I.M., 2014. Degradation study of piperazine, its blends and structural analogs for CO_2 capture: A review. Int. J. Greenh. Gas Control, 31, 214–228.

Mimura, T., Shimojo, S., Suda, T., Iijima, M., Mitsuoka, S., 1995. Research and development on energy-saving technology for flue gas carbon dioxide recovery and steam system in power plant. Energy Convers. Manag., 36, 397–400.

Moioli, S., Pellegrini, L.A., 2015. Improved rate-based modelling of the process of CO_2 capture with PZ solution. Chem. Eng. Res. Des., 93, 611–620.

Montañés, R., Flø, N., Nord, L., 2017a. Dynamic Process Model Validation and Control of the Amine Plant at CO_2 Technology Centre Mongstad. Energies, 10, 1527.

Montañés, R., GarÐarsdóttir, S.Ó., Normann, F., Johnsson, F., Nord, L.O., 2017b. Demonstrating load-change transient performance of a commercial-scale natural gas combined cycle power plant with post-combustion CO2 capture. Int. J. Greenh. Gas Control, 63, 158–174.

Moore, T., Nguyen, D., Iyer, J., Roy, P., Stolaroff, J.K., 2021. Advanced absorber heat integration via heat exchange packings. AIChE J., 67, 1-14.

Moser, P., Schmidt, S., Sieder, G., Garcia, H., Stoffregen, T., 2011. Performance of MEA in a long-term test at the post-combustion capture pilot plant in Niederaussem. Int. J. Greenh. Gas Control, 5, 620–627.

Mostafavi, E., Ashrafi, O., Navarri, P., 2021. Assessment of process modifications for amine-based post-combustion carbon capture processes. Clean. Eng. Technol., 4, 100249.

Mulgundmath, V., Tezel, F.H., 2010. Optimisation of carbon dioxide recovery from flue gas

in a TPSA system. Adsorption, 16, 587–598.

Munjal, S., Duduković, M.P., Ramachandran, P., 1989. Mass-transfer in rotating packed beds—II. Experimental results and comparison with theory and gravity flow. Chem. Eng. Sci., 44, 2257–2268.

Nessi, E., Papadopoulos, A.I., Seferlis, P., 2021. A review of research facilities, pilot and commercial plants for solvent-based post-combustion CO_2 capture: Packed bed, phase-change and rotating processes. Int. J. Greenh. Gas Control, 111, 103474.

Nguyen, T., Hilliard, M., Rochelle, G.T., 2010. Amine volatility in CO2 capture. Int. J. Greenh. Gas Control, 4, 707–715.

Nittaya, T., Douglas, P.L., Croiset, E., Ricardez-Sandoval, L.A., 2014. Dynamic modelling and evaluation of an industrial-scale CO_2 capture plant using monoethanolamine absorption processes. Ind. Eng. Chem. Res., 53, 11411–11426.

Notz, R., Mangalapally, H.P., Hasse, H., 2012. Post-combustion CO_2 capture by reactive absorption: Pilot plant description and results of systematic studies with MEA. Int. J. Greenh. Gas Control, 6, 84–112.

Nwaoha, C., Idem, R., Supap, T., Saiwan, C., Tontiwachwuthikul, P., Rongwong, W., Al-Marri, M.J., Benamor, A., 2017. Heat duty, heat of absorption, sensible heat and heat of vaporization of 2–Amino–2–Methyl–1–Propanol (AMP), Piperazine (PZ) and Monoethanolamine (MEA) tri–solvent blend for carbon dioxide (CO_2) capture. Chem. Eng. Sci., 170, 26–35.

Oko, E., Ramshaw, C., Wang, M., 2018. Study of intercooling for rotating packed bed absorbers in intensified solvent-based CO_2 capture process. Appl. Energy, 223, 302–316.

Oko, E., Wang, M., Joel, A.S., 2017. Current status and future development of solvent-based carbon capture. Int. J. Coal Sci. Technol., 4, 5–14.

Oko, E., Wang, M., Ramshaw, C., 2019. Study of mass transfer correlations for rotating packed bed columns in the context of solvent-based carbon capture. Int. J. Greenh. Gas Control, 91, 102831.

Onda, K., Takeuchi, H., Okumoto, Y., 1968. Mass transfer coefficients between gas and liquid phases in packed columns. J. Chem. Eng. Japan, 1, 56–62.

Otitoju, O., Oko, E., Wang, M., 2020. A new method for scale-up of solvent-based post-combustion carbon capture process with packed columns. Int. J. Greenh. Gas Control, 93, 102900.

Otitoju, O., Oko, E., Wang, M., 2021. Technical and economic performance assessment of post-combustion carbon capture using piperazine for large scale natural gas combined cycle power plants through process simulation. Appl. Energy, 292, 116893.

Oyenekan, A.B., Rochelle, T.G., 2007. Alternative Stripper Configurations for CO_2 Capture by Aqueous Amines. AIChE J., 53, 3144–3154.

Oyenekan, B.A., Rochelle, G.T., 2005. Energy Performance of Stripper Configurations for

CO_2 Capture by Aqueous Amines. Ind. & Eng. Chem. Res., 45, 2457–2464.

Piché, S., Larachi, F., Grandjean, B.P.A., 2001. Loading capacity in packed towers - Database, correlations and analysis. Chem. Eng. Technol., 24, 373–380.

Pinsent, B.R.., Pearson, L., Roughton, F.W.., 1956. The kinetics of combination of carbon dioxide with hydroxide ions. Trans. Faraday Soc., 1512–1520.

Pinto, D.D.D., Brodtkorb, T.W., Vevelstad, S.J., Knuutila, H., Svendsen, H.F., 2014. Modeling of oxidative MEA degradation. Energy Procedia, 63, 940–950.

Plaza, J.M., Rochelle, G.T., 2011. Modelling pilot plant results for CO_2 capture by aqueous piperazine. Energy Procedia, 4, 1593–1600.

Posey, M.L., Rochelle, G.T., 1997. A Thermodynamic Model of Methyldiethanolamine–CO_2 –H 2 S–Water. Ind. Eng. Chem. Res., 36, 3944–3953.

Qian, Z., Li, Z.H., Guo, K., 2012. Industrial applied and modelling research on selective H 2S removal using a rotating packed bed. Ind. Eng. Chem. Res., 51, 8108–8116.

Rabensteiner, M., Kinger, G., Koller, M., Gronald, G., Hochenauer, C., 2015a. Investigation of carbon dioxide capture with aqueous piperazine on a post-combustion pilot plant-Part I: Energetic review of the process. Int. J. Greenh. Gas Control, 39, 79–90.

Rabensteiner, M., Kinger, G., Koller, M., Gronald, G., Hochenauer, C., 2015b. Investigation of carbon dioxide capture with aqueous piperazine on a post-combustion pilot plant - Part II: Parameter study and emission measurement. Int. J. Greenh. Gas Control, 37, 471–480.

Rackett, H.G., 1970. Equation of State for Saturated Liquids. J. Chem. Eng. Data, 15, 514–517.

Rahimi, M.R., Mosleh, S., 2015. CO_2 Removal from Air in a Countercurrent Rotating Packed Bed, Experimental Determination of Height of Transfer Unit. Adv. Environ. Sci. Technol., 1, 19–24.

Rahimpour, M.R., Kashkooli, A.Z., 2004. Absorber using amine-promoted potash solution. Iran. J. Sci. Technol. Trans. B., 28, 653–666.

Rao, D.P., Bhowal, A., Goswami, P.S., 2004. Process Intensification in Rotating Packed Beds (HIGEE): An Appraisal. Ind. Eng. Chem. Res., 43, 1150–1162.

Razi, N., Svendsen, H.F., Bolland, O., 2013. Validation of mass transfer correlations for CO_2 absorption with MEA using pilot data. Int. J. Greenh. Gas Control, 19, 478–491.

Reddy, S., Johnson, D., Gilmartin, J., 2008. Fluor's econamine FG plus^{SM} technology for CO_2 capture at coal-fired power plants. Air Waste Manag. Assoc. - 7th Power Plant Air Pollut. Control "Mega" Symp. 2008, 1, 63–79.

Reddy, S., Scherffius, J.R., Yonkoski, J., Radgen, P., Rode, H., 2013. Initial results from fluor's CO_2 capture demonstration plant using econamine FG Plus^{SM} technology at E.ON Kraftwerke's wilhelmshaven power plant. Energy Procedia, 37, 6216–6225.

Rezazadeh, F., Gale, W.F., Rochelle, G.T., Sachde, D., 2017. Effectiveness of absorber

intercooling for CO_2 absorption from natural gas-fired flue gases using monoethanolamine solvent. Int. J. Greenh. Gas Control, 58, 246–255.

Rocha, J.A., Bravo, J.L., Fair, J.R., 1996. Distillation columns containing structured packings: A comprehensive model for their performance. 2. Mass-transfer model. Ind. Eng. Chem. Res., 35, 1660–1667.

Rochelle, G., Chen, E., Freeman, S., Van Wagener, D., Xu, Q., Voice, A., 2011. Aqueous piperazine as the new standard for CO_2 capture technology. Chem. Eng. J., 171, 725–733.

Rochelle, G.T., Wu, Y., Chen, E., Akinpelumi, K., Fischer, K.B., Gao, T., Liu, C.-T., Selinger, J.L., 2019. Pilot plant demonstration of piperazine with the advanced flash stripper. Int. J. Greenh. Gas Control, 84, 72–81.

Sachde, D., Chen, E., Rochelle, G.T., 2013. Modeling Pilot Plant Performance of an Absorber with Aqueous Piperazine. Energy Procedia, 37, 1987–2001

SaskPower, 2012. Boundary Dam Integrated Carbon Capture and Storage Demonstration Project 1–2.

Schach, M.O., Schneider, R., Schramm, H., Repke, J.U., 2010. Techno-economic analysis of post-combustion processes for the capture of carbon dioxide from power plant flue gas. Ind. Eng. Chem. Res., 49, 2363–2370.

Scherffius, J.R., Reddy, S., Klumpyan, J.P., Armpriester, A., 2013. Large-scale CO_2 capture demonstration plant using fluor's econamine FG Plus^{SM} technology at NRG's WA parish electric generating station. Energy Procedia, 37, 6553–6561.

Schneider, R., Kenig, E.Y., Górak, A., 1999. Dynamic modelling of reactive absorption with the maxwell-Stefan approach. Chem. Eng. Res. Des., 77, 633–638.

Seader, J.D., Seider, W.D., Lewin, D.R., Boulle, L., Rycrof, A., 2006. Separation Process Principles, 3rd ed. John Wiley & Sons, INC, Hoboken, NJ.

Seibert, F., Chen, E., Perry, M., Briggs, S., Montgomery, R., Rochelle, G., 2011. UT/SRP CO_2 capture pilot plant — Operating experience and procedures. Energy Procedia, 4, 1616–1623.

Sherwood, T.K., Shipley, G.H., Holloway, F.A.L., 1938. Flooding Velocities in Packed Columns. Ind. Eng. Chem., 30, 765–769.

Singh, S.P., Counce, R.M., Wilson, J.H., Villiers-Fisher, J.F., Jennings, H.L., Lucero, A.J., Reed, G.D., Ashworth, R.A., Elliott, M.G., 1992. Removal of Volatile Organic Compounds from Groundwater Using a Rotary Air Stripper. Ind. Eng. Chem. Res., 31, 574–580.

Sinnott, R.K., 2005. Chemical Engineering Design, Fourth ed, Coulson & Richardson's Chemical Engineering series. Elsevier Butterworth-Heinemann, Oxford.

Sipöcz, N., Tobiesen, F.A., 2012. Natural gas combined cycle power plants with CO2capture - Opportunities to reduce cost. Int. J. Greenh. Gas Control, 7, 98–106.

Soave, G., 1972. Equilibrium constants from a modified Redlich-Kwong equation of state. Chem. Eng. Sci., 27, 1197–1203.

Song, C., Liu, Q., Ji, N., Deng, S., Zhao, J., Kitamura, Y., 2017. Natural gas purification by heat pump assisted MEA absorption process. Appl. Energy, 204, 353–361.

Sreedhar, I., Nahar, T., Venugopal, A., Srinivas, B., 2017. Carbon capture by absorption – Path covered and ahead. Renew. Sustain. Energy Rev., 76, 1080–1107.

Stec, M., Tatarczuk, A., Więcław-Solny, L., Krótki, A., Ściążko, M., Tokarski, S., 2015. Pilot plant results for advanced CO2 capture process using amine scrubbing at the Jaworzno II Power Plant in Poland. Fuel, 151, 50–56.

Steeneveldt, R., Berger, B., Torp, T.A., 2006. CO_2 Capture and Storage: Closing the Knowing-Doing Gap. Chem. Eng. Res. Des., 84, 739–763.

Stéphenne, K., 2014. Start-up of World's First Commercial Post-combustion Coal-Fired CCS Project: Contribution of Shell Cansolv to SaskPower Boundary Dam ICCS Project. Energy Procedia, 63, 6106–6110.

Stichlmair, J., Bravo, J.L., Fair, J.R., 1989. General model for prediction of pressure drop and capacity of countercurrent gas/liquid packed column. Gas Sep. Purif., 61, 19–28.

Strigle, R.F., 1994. Packed tower design and applications: random and structured packings, 2nd ed. Gulf Publishing Company, Houston.

Sudhoff, D., Leimbrink, M., Schleinitz, M., Górak, A., Lutze, P., 2015a. Modelling, design and flexibility analysis of rotating packed beds for distillation. Chem. Eng. Res. Des., 94, 72–89.

Suess, P., Spiegel, L., 1992. Hold-up of mellapak structured packings. Chem. Eng. Process., 31, 119–124.

Supap, T., Idem, R., Tontiwachwuthikul, P., Saiwan, C., 2011. Investigation of degradation inhibitors on CO_2 capture process. Energy Procedia, 4, 583–590.

Tan, C.S., Chen, J.E., 2006. Absorption of carbon dioxide with piperazine and its mixtures in a rotating packed bed. Sep. Purif. Technol., 49, 174–180.

Thiels, M., Wong, D.S.H., Yu, C.H., Kang, J.L., Jang, S.S., Tan, C.S., 2016. Modelling and Design of Carbon Dioxide Absorption in Rotating Packed Bed and Packed Column. IFAC-PapersOnLine, 49, 895–900.

Tsai, R.E., Seibert, S.R., Eldridge, B., Rochelle, G.T., 2011. A Dimensional Model for Predicting the Mass-Transfer Area of Structured Packing. AIChE J., 57, 1173–1184.

Tung, H.-H., Mah, R.S.H., 1985. Modelling liquid mass transfer in HIGEE separation process. Chem. Eng. Commun., 39, 147–153.

Van Wagener, D.H., 2011. Stripper Modeling for CO_2 Removal Using Monoethanolamine and Piperazine Solvents. PhD Thesis. University of Texas at Austin.

Van Wagener, D.H., Rochelle, G.T., Chen, E., 2013. Modelling of pilot stripper results for CO_2 capture by aqueous piperazine. Int. J. Greenh. Gas Control, 12, 280–287.

Wang, M., Joel, A.S., Ramshaw, C., Eimer, D., Musa, N.M., 2015. Process intensification for post-combustion CO_2 capture with chemical absorption: A critical review. Appl.

Energy, 158, 275–291.

Wang, M., Lawal, A., Stephenson, P., Sidders, J., Ramshaw, C., 2011. Post-combustion CO2capture with chemical absorption: A state-of-the-art review. Chem. Eng. Res. Des., 89, 1609–1624.

Wang, T., Lackner, K.S., Wright, A., 2011. Moisture Swing Sorbent for Carbon Dioxide Capture from Ambient Air. Environ. Sci. Technol., 45, 6670–6675.

Wang, X., Song, C., 2020. Carbon Capture From Flue Gas and the Atmosphere: A Perspective. Front. Energy Res., 8, 560849.

Whitman, W.G., 1924. The Two-Film Theory of Gas Absorption. Chem. Metall. Eng., 29, 146–148.

Więckol-Ryk, A., Krzemień, A., Smoliński, A., Lasheras, F.S., 2018. Analysis of biomass blend co-firing for post-combustion CO_2 capture. Sustain., 10, 1–15.

Wilke, C.R., Chang, P., 1955. Correlation of diffusion coefficients in dilute solutions. AIChE J., 1, 264–270.

Wolf-Zöllner, V., Seibert, F., Lehner, M., 2019. Extended performance comparison of different pressure drop, hold-up and flooding point correlations for packed columns. Chem. Eng. Res. Des., 147, 699–708.

Yi, F., Zou, H.K., Chu, G.W., Shao, L., Chen, J.F., 2009. Modelling and experimental studies on absorption of CO_2 by Benfield solution in rotating packed bed. Chem. Eng. J., 145, 377–384.

Ying, J., Eimer, D.A., 2012. Measurements and correlations of diffusivities of nitrous oxide and carbon dioxide in monoethanolamine + water by laminar liquid jet. Ind. Eng. Chem. Res., 51, 16517–16524.

Ying, J., Eimer, D.A., Wenjuan, Y., 2012. Measurements and correlation of physical solubility of carbon dioxide in (monoethanolamine + water) by a modified technique. Ind. Eng. Chem. Res., 51, 6958–6966.

Yu, C.-H., Huang, C.-H., Tan, C.-S., 2012. A Review of CO_2 Capture by Absorption and Adsorption. Aerosol Air Qual. Res., 12, 745–769.

Yu, C.H., Cheng, H.H., Tan, C.S., 2012. CO_2 capture by alkanolamine solutions containing diethylenetriamine and piperazine in a rotating packed bed. Int. J. Greenh. Gas Control, 9, 136–147.

Zhang, L.-L., Wang, J.-X., Xiang, Y., Zeng, X.-F., Chen, J.-F., 2011. Absorption of Carbon Dioxide with Ionic Liquid in a Rotating Packed Bed Contactor: Mass Transfer Study. Ind. Eng. Chem. Res., 50, 6957–6964.

Zhang, R., Zhang, X., Yang, Q., Yu, H., Liang, Z., Luo, X., 2017. Analysis of the reduction of energy cost by using MEA-MDEA-PZ solvent for post-combustion carbon dioxide capture (PCC). Appl. Energy, 205, 1002–1011.

Zhang, Y., Chen, C.C., 2013. Modelling CO2 absorption and desorption by aqueous monoethanolamine solution with Aspen rate-based model. Energy Procedia, 37,

1584–1596.

Zhang, Y., Chen, H., Chen, C.C., Plaza, J.M., Dugas, R., Rochelle, G.T., 2009. Rate-based process modelling study of CO2 Capture with aqueous monoethanolamine solution. Ind. Eng. Chem. Res. 48, 9233–9246. https://doi.org/10.1021/ie900068k

Zhang, Y., Sachde, D., Chen, E., Rochelle, G., 2017. Modelling of absorber pilot plant performance for CO_2 capture with aqueous piperazine. Int. J. Greenh. Gas Control, 64, 300–313.

Zhang, Z., Kai, G., Huijuan, L., Junnan, S., Zhi, Q., 2014. Characteristics of mass transfer between gas-liquid phases in a higee reactor. Chem. Ind. Chem. Eng. Q., 20, 523–530.

Zhou, S., Chen, X., Nguyen, T., Voice, A.K., Rochelle, G.T., 2010. Aqueous ethylenediamine for CO_2 capture. ChemSusChem, 3, 913–918.